


2018

Effect of Nonclassical Optical Turbulence on a Propagating Laser Beam

Melissa Beason
University of Central Florida

 Part of the [Electrical and Computer Engineering Commons](#)
Find similar works at: <https://stars.library.ucf.edu/etd>
University of Central Florida Libraries <http://library.ucf.edu>

This Doctoral Dissertation (Open Access) is brought to you for free and open access by STARS. It has been accepted for inclusion in Electronic Theses and Dissertations by an authorized administrator of STARS. For more information, please contact STARS@ucf.edu.

STARS Citation

Beason, Melissa, "Effect of Nonclassical Optical Turbulence on a Propagating Laser Beam" (2018).
Electronic Theses and Dissertations. 6161.
<https://stars.library.ucf.edu/etd/6161>



EFFECT OF NONCLASSICAL OPTICAL TURBULENCE ON A PROPAGATING LASER BEAM

by

MELISSA K. BEASON
B.S. University of Florida, 1983
M.S. University of Central Florida, 1985

A dissertation submitted in partial fulfillment of the requirements
for the degree of Doctor of Philosophy
in the Department of Electrical and Computer Engineering
in the College of Engineering and Computer Science
at the University of Central Florida
Orlando, Florida

Fall Term
2018

Major Professor: Ronald Phillips

© 2018 Melissa Beason

ABSTRACT

Theory developed for the propagation of a laser beam through optical turbulence generally assumes that the turbulence is both homogeneous and isotropic and that the associated spectrum follows the classical Kolmogorov spectral power law of $\kappa^{-11/3}$. If the atmosphere deviates from these assumptions, beam statistics such as mean intensity, correlation, and scintillation index could vary significantly from mathematical predictions. This work considers the effect of nonclassical turbulence on a propagated beam. Namely, anisotropy of the turbulence and a power law that deviates from $\kappa^{-11/3}$. A mathematical model is developed for the scintillation index of a Gaussian beam propagated through nonclassical turbulence and theory is extended for the covariance function of intensity of a plane wave propagated through nonclassical turbulence. Multiple experiments over a concrete runway and a grass range verify the presence of turbulence which varies between isotropy and anisotropy. Data is taken throughout the day and the evolution of optical turbulence is considered. Also, irradiance fluctuation data taken in May 2018 over a concrete runway and July 2018 over a grass range indicate an additional beam shaping effect. A simplistic mathematical model was formulated which reproduced the measured behavior of contours of equal mean intensity and scintillation index.

For my family

You believed God called me to this and you never doubted my ability.

ACKNOWLEDGMENTS

Ron Phillips: Thank you for seeing something in me and your dedication to pushing me to be my best.

Larry Andrews: Thank you for never doubting my abilities, for spending hours and hours at your kitchen table teaching me, for picking me up when I would get discouraged, for the hours on the phone brainstorming, and most of all for sharing your excitement over the beauty of mathematics!

WPRG Team - Bob, Jon, Joe, Frank, Chris, Franklin and Bruce: You have taught me so much with great patience and put up with me pushing for better and better data. Much of this work would not have been possible without your input. Thank you.

This work was supported through the Office of Naval Research grant Atmospheric Propagation for High Energy Lasers (N00014-17-1-2100).

TABLE OF CONTENTS

LIST OF FIGURES	ix
LIST OF TABLES	xvi
LIST OF SYMBOLS AND NOTATION.....	xvii
CHAPTER 1: INTRODUCTION	1
CHAPTER 2: OPTICAL TURBULENCE	5
CHAPTER 3: BEAM PROPAGATION THROUGH OPTICAL TURBULENCE ...	13
3.1 Free-Field Propagation	13
3.2 Gaussian Solution in Free Field	15
3.3 Propagation through Random Media	19
3.3.1 Spectral Representations	24
3.3.2 Derivation of Relevant Statistical Moments	27
3.3.3 Field Moments.....	30
CHAPTER 4: LONG-TERM SPOT SIZE, NORMALIZED INTENSITY AND SCINTILLATION INDEX IN NONCLASSICAL OPTICAL TURBULENCE	35
4.1 Comparison of Two Common Methods to Calculate Spot Size.....	39
4.1.1 Method 1	39
4.1.2 Method 2	41

4.1.3 Comparison of Methods	43
4.2 Normalized Intensity	48
4.3 Scintillation Index	50
CHAPTER 5: COVARIANCE OF INTENSITY, THEORY AND MEASUREMENT IN NONCLASSICAL TURBULENCE	57
5.1 Plane Wave CFI Theory.....	59
5.2 CFI Experimental Setup and Processing	61
5.3 Comparison of Theory to Experimental Results.....	64
CHAPTER 6: EVOLUTION OF TURBULENCE OVER MULTIPLE DAYS	72
6.1 CFI for Near Plane Wave, Winter 2017.....	75
6.2 Scintillation Index for Gaussian Beam, Summer 2017	83
6.3 Experimental Observations	90
CHAPTER 7: BEAM SHAPING AND ANISOTROPY	96
7.1 Mathematical Model and Predicted Behavior.....	98
7.2 Experiment.....	108
7.2.1 Experimental layout.....	109
7.2.2 Experimental results	110
7.3 Experimental Observations	117
CHAPTER 8: CONCLUSIONS	119

8.1 Summary of Contributions.....	119
8.2 Future Work	121
APPENDIX A: DERIVATION OF THE INNER SCALE PARAMETER	122
APPENDIX B: COPYRIGHT PERMISSIONS	126
REFERENCES	129

LIST OF FIGURES

Figure 1. Cascade of energy between scale sizes from energy injection at outer scale to dissipation at inner scale. Plot shows power relationship between scale sizes. Note the logarithmic vertical axis.	6
Figure 2. Propagation geometry between points S and R	14
Figure 3. Relationship between transmitter and receiver beam parameters.....	18
Figure 4. Comparison of two methods to compute beam diameter in the vertical (y) direction for three anisotropy ratios as a function of power law, α , for 50 cm transmit aperture with propagation distance of 5 km and $\tilde{C}_n^2 = 1 \times 10^{-14} m^{3-\alpha}$	44
Figure 5. Comparison of two methods to compute beam diameter in the vertical (y) direction for three anisotropy ratios as a function of power law, α , for 5 cm transmit aperture with propagation distance of 5 km and $\tilde{C}_n^2 = 1 \times 10^{-14} m^{3-\alpha}$	44
Figure 6. Comparison of beam contours for two methods with $\alpha = 3.5$, $L = 5$ km and $\tilde{C}_n^2 = 1 \times 10^{-14} m^{3-\alpha}$. (a) $\mu_y / \mu_x = 2$, (b) $\mu_y / \mu_x = 0.5$	46
Figure 7. Comparison of beam contours for two methods with $\alpha = 3.2$, $L = 5$ km and $\tilde{C}_n^2 = 1 \times 10^{-14} m^{3-\alpha}$. (a) $\mu_y / \mu_x = 2$, (b) $\mu_y / \mu_x = 0.5$	47
Figure 8. Equal mean-intensity contours resulting from propagation of 632.8 nm collimated beam with 1 cm transmitter diameter through nonclassical turbulence where $\alpha = 3.5$, $\mu_y / \mu_x = 0.33$ and $\tilde{C}_n^2 = 1 \times 10^{-13}$	49

Figure 9. Mean intensity along vertical axis resulting from propagation of 632.8 nm collimated beam with 1 cm transmitter diameter through nonclassical turbulence where $\alpha = 3.5$, $\mu_y / \mu_x = 0.33$ and $\tilde{C}_n^2 = 1 \times 10^{-13}$	50
Figure 10. Contours of equal scintillation index resulting from 100 m propagation of 632.8 nm collimated beam with 1 cm transmitter diameter through nonclassical turbulence where $\alpha = 3.5$, $\mu_y / \mu_x = 0.33$ and $\tilde{C}_n^2 = 1 \times 10^{-13}$	54
Figure 11. Scintillation index along vertical axis resulting from propagation of 632.8 nm collimated beam with 1 cm transmitter diameter through nonclassical turbulence where $\alpha = 3.5$, $\mu_y / \mu_x = 0.33$ and $\tilde{C}_n^2 = 1 \times 10^{-13}$. Propagation distance is shown on figure.	55
Figure 12. Aerial view of SLF runway, Kennedy Space Center, Florida. Reprinted with permission from [17], Optical Society of America.....	58
Figure 13. Experimental configuration. The transmitter consisted of a 532 nm collimated laser with a 10 cm Gaussian spatial profile. A GC660 camera was placed before the focus of the 12 cm receiver lens. Reprinted with permission from [17], Optical Society of America.	63
Figure 14. Typical CCD image. Note how the entire circular lens is visible on the CCD.....	63
Figure 15. January 31, 2017, 9:12 am. Normalized CFI resulting from 1 km propagation (line) compared to theoretical calculation (triangle). Theoretical anisotropy ratio $\mu_y / \mu_x = 1/0.95$. No rotation angle. Scale factor of 0.75 (slight	

focus) was used in comparing data to theory. (a) measured normalized CFI, (b) theoretical normalized CFI, (c) measured (line) and theoretical (triangles) cross section through major axis (d) measured (line) and theoretical (triangles) cross section through minor axis. Reprinted with permission from [17], Optical Society of America. 69

Figure 16. January 31, 2017, 5:05 pm. Normalized CFI resulting from 1 km propagation (line) compared to theoretical calculation (triangle). Theoretical anisotropy ratio $\mu_y/\mu_x = 1/0.6$. Theoretical were results rotated -8 degrees to obtain tilt of measured results. Scale factor of 0.45 (slight focus) was used in comparing data to theory. (a) measured normalized CFI, (b) theoretical normalized CFI, (c) measured (line) and theoretical (triangles) cross section through major axis (d) measured (line) and theoretical (triangles) cross section through minor axis. Reprinted with permission from [17], Optical Society of America. 70

Figure 17. February 2, 2017, 5:41 pm. Normalized CFI resulting from 2 km propagation distance (solid line) compared to theoretical calculation (triangle). Theoretical anisotropy ratio $\mu_y/\mu_x = 0.6/1$. Theoretical results were rotated 12 degrees to obtain tilt of measured results. Scale factor of 1.9 (slight defocus) was used in comparing data to theory. (a) measured normalized CFI, (b) theoretical normalized CFI, (c) measured (line) and theoretical (triangles) cross section through major axis (d) measured (line) and theoretical (triangles) cross

section through minor axis. Reprinted with permission from [17], Optical Society of America.	71
Figure 18. Contours of equal normalized CFI from 1 km propagation of 532 nm near-plane wave beam on January 31, 2017. Dimensions are in centimeters. Measurement times for (a)-(c) are given on the images. Reprinted with permission from [19], Optical Society of America.	78
Figure 19. Atmospheric data from instruments located on SLF, January 31, 2017. (a) C_n^2 from Scintec BLS 900; (b) air and ground temperature on runway; (c) solar flux on runway. Reprinted with permission from [19], Optical Society of America.	79
Figure 20. Wind magnitude (red) and direction (blue) from sonic anemometers located along propagation path on January 31, 2017. (a) Near start of path; (b) near middle of path. Reprinted with permission from [19], Optical Society of America.	80
Figure 21. Contours of equal normalized CFI from 2 km propagation of 532 nm near-plane wave beam on February 2, 2017. Dimensions are in centimeters. Measurement times for (a)-(d) are given on the images. Reprinted with permission from [19], Optical Society of America.	81
Figure 22. Atmospheric data from instruments located on SLF, February 2, 2017. (a) C_n^2 from Scintec BLS 900; (b) air and ground temperature on runway; (c) solar flux on runway. Reprinted with permission from [19], Optical Society of America.	82

Figure 23. Wind magnitude (red) and direction (blue) from sonic anemometers located along propagation path on February 2, 2017. (a) Near start of path; (b) near end of path. Reprinted with permission from [19], Optical Society of America.	83
Figure 24. Equal intensity contours of 532 nm beam prior to propagation through turbulence. Axes correspond to pixels where only the region of the CCD with the beam is shown.....	84
Figure 25. Experimental layout at SLF, August 2017. Reprinted with permission from [19], Optical Society of America.	85
Figure 26. Contours of equal scintillation index from 100 m propagation of 532 nm Gaussian beam on August 1, 2017. Axes dimensions correspond to pixels. Measurement times for (a)-(g) are given on the images. Reprinted with permission from [19], Optical Society of America.	87
Figure 27. Atmospheric data from instruments located on SLF, August 1, 2017. (a) C_n^2 from SRS; (b) air and ground temperature on runway; (c) solar flux on runway. Reprinted with permission from [19], Optical Society of America.	88
Figure 28. Wind magnitude (red) and direction (blue) from sonic anemometer located near receiver on August 1, 2017. Reprinted with permission from [19], Optical Society of America.	89
Figure 29 . Contours of equal scintillation index from 100 m propagation of 532 nm Gaussian beam on August 3, 2017. Axes dimensions correspond to pixels.	

Measurement times for (a)-(g) are given on the images. Reprinted with permission from [19], Optical Society of America.	91
Figure 30. Atmospheric data from instruments located on SLF, August 3, 2017.	
(a) C_n^2 from SRS; (b) air and ground temperature on runway; (c) solar flux on runway. Reprinted with permission from [19], Optical Society of America.	92
Figure 31. Wind magnitude (red) and direction (blue) from sonic anemometer located near receiver on August 3, 2017. Reprinted with permission from [19], Optical Society of America.	
93	
Figure 32. Effect of an index gradient on free-field propagation of a Gaussian beam. (a) Beam after 100 m propagation with no index gradient; (b) beam after 100 m propagation with index gradient of $\Delta n = 2 \times 10^{-9}$	
99	
Figure 33. Anisotropy combinations without index gradient and $C_n^2 = 5 \times 10^{-14} m^{-2/3}$.	
Figure dimensions are in mm. (a), (b) Mean intensity and radial component of scintillation index for isotropic turbulence. (c), (d) Mean intensity and radial component of scintillation index for anisotropic turbulence with $\mu_y / \mu_x = 1/2$. .	
105	
Figure 34. (a), (b) Mean intensity and radial component of scintillation index for anisotropic turbulence with $\mu_y / \mu_x = 1/2$, $C_n^2 = 5 \times 10^{-13} m^{-2/3}$ and no beam shaping.	
106	
Figure 35. Anisotropy combinations with beam shaping where $W_x = 0.75W_y$ and $C_n^2 = 5 \times 10^{-14} m^{-2/3}$. (a), (b) Mean intensity and radial component of scintillation	

index for isotropic turbulence. (c), (d) Mean intensity and radial component of scintillation index for anisotropic turbulence with $\mu_y / \mu_x = 1/2$	107
Figure 36. (a) SLF concrete runway; (b) TISTEF grass range.....	108
Figure 37. (a) Beam as seen by camera; (b) cross sections of beam at center.	110
Figure 38. Experimental layout.	110
Figure 39. Measured mean intensity and corresponding scintillation index contours resulting from propagation of 6.5 mm radius beam for 100 m at SLF on 1 May 2018. Dimensions are in mm. (a-b) 10:52 ET; (c-d) 14:32 ET.	112
Figure 40. Measured mean intensity and corresponding scintillation index contours resulting from propagation of 6.5 mm radius beam for 125 m at SLF on 3 May 2018. (a-b) 7:43 ET; (c-d) 9:10 ET; (e-f) 10:32 ET; (g-h) 13:48 ET.....	115
Figure 41. Measured mean intensity and corresponding scintillation index contours resulting from propagation of 6.5 mm radius beam for 125 m at TISTEF on 3 July 2018. Dimensions in mm. (a-b) 9:18 ET; (c-d) 10:07 ET; (e-f) 16:48 ET; (g-h) 18:51 ET.	116

LIST OF TABLES

Table 1. Time, Atmospheric Conditions, and Rytov Variance Corresponding to Measurement Times. Anemometer (1) was located near the transmitter and anemometer (2) was located mid-path on 31 January and near the receiver on 2 February. The wind direction is relative to the propagation direction where 0° is wind blowing in the direction of propagation. σ_R^2 is the Rytov variance. Reprinted with permission from [17], Optical Society of America.....	68
Table 2. Wind and turbulence strength information for measurement times. C_n^2 is measured using BLS900 at TISTEF and UCF manufactured device at SLF. ...	118

LIST OF SYMBOLS AND NOTATION

$\bar{I}(x, y)$	Mean of $I(x, y)$
$\langle I(x, y) \rangle$	Ensemble average of $I(x, y)$
A_0	Gaussian beam amplitude
$A(\alpha)$	Spectrum multiplicative factor
$B_I(r_1, r_2)$	Covariance of intensity
$B_n(R_1, R_2)$	Spatial covariance of index of refraction
B_χ	Log amplitude covariance
$b_I(r_1, r_2)$	Normalized covariance of intensity
C_n^2	Refractive index structure parameter
C_T^2	Temperature structure parameter
C_v^2	Velocity structure parameter
$dv(K, z)$	Random spectral amplitude of index of refraction
D_n	Index of refraction structure function
D_T	Temperature structure function
D_v	Velocity structure function
E_1, E_2, E_3	Field statistical moment

F_0	Phase front radius of curvature for Gaussian beam at transmitter
F_n	Two dimensional index of refraction power spectrum
F	Phase front radius of curvature for Gaussian beam at receiver
${}_1F_1$	Confluent hypergeometric function
${}_2F_1$	Hypergeometric function
$G(\mathbf{r}, \mathbf{s}, z)$	Green's function
I_0	Intensity at transmitter
I^0	Free field intensity
I	Intensity
k	Optical wave number
l_0	Inner scale of turbulence
L_0	Outer scale of turbulence
L	Propagation distance
n	Index of refraction
n_0	Mean index of refraction
n_1	Random fluctuation in index of refraction

P	Atmospheric pressure
q	Transformed spatial wavenumber
q_m	Transformed inner scale wavenumber parameter
q_o	Transformed outer scale wavenumber
T	Temperature
T_x, T_y	Parameters describing beam spread in x, y directions due to turbulence
$U_0(\mathbf{r}, z)$	Complex field amplitude in free space
U_m	m th order Born perturbation
$U(\mathbf{r}, z)$	Complex field amplitude in turbulence
W_0	Gaussian beam radius at transmitter
W_{LT}	Long term beam radius
W_{LTx}, W_{LTy}	Long term beam radius in x, y directions
W	Gaussian beam radius in free space at receiver
W_x, W_y	Free space Gaussian beam radius in x, y directions
α	Spectral power law
γ, γ'	Gaussian propagation parameters

$\Gamma(x)$	Gamma function
ε	Dissipation rate
Θ_0	Gaussian beam curvature parameter at transmitter
Θ	Gaussian beam curvature parameter at receiver
$\bar{\Theta}$	$1 - \Theta$
\mathbf{K}	Spatial wave number vector
K_x, K_y	x, y components of spatial wave number
K_{mx}, K_{my}	x, y components of inner scale spatial wave number parameter
K_{ox}, K_{oy}	x, y components of outer scale spatial wave number parameter
λ	Wavelength
Λ_0	Fresnel ratio of Gaussian beam at transmitter
Λ	Fresnel ratio of Gaussian beam at receiver
Λ_x, Λ_y	Fresnel ratio in x, y directions
μ_x, μ_y	x, y anisotropy parameters
ν	Viscosity
$\tilde{\rho}_0$	Spatial coherence radius in generalized

	turbulence
$\tilde{\rho}_{0,x}, \tilde{\rho}_{0,y}$	x, y components of coherence radius in generalized turbulence
σ_I^2	Scintillation index
$\sigma_{I,l}^2$	Longitudinal component of scintillation index
$\sigma_{I,r}^2$	Off axis component of scintillation index
σ_r^2	Parameter describing radial changes in intensity
σ_R^2	Rytov variance
$\tilde{\sigma}_R^2$	Generalized Rytov variance
$\Phi_n(\mathbf{K})$	Spatial power spectrum of index of refraction
$\tilde{\Phi}_n(q)$	Transformed spatial power spectrum of index
ϕ_m	Normalized Born perturbation
χ	Field log amplitude
Ψ, Ψ_1, Ψ_2	Rytov perturbation parameters

CHAPTER 1: INTRODUCTION

In a laboratory environment, a laser beam will propagate for long distances with little loss of power or coherence. However, when propagated in the atmosphere, a laser beam is negatively impacted by absorption, scattering and atmospheric turbulence. Scattering and absorption reduce the propagated power but optical turbulence has a much more deleterious effect on the beam in that it causes beam spreading beyond diffraction, causes the beam to wander, reduces the coherence of the beam, and causes the beam to self-interfere or scintillate.

Optical turbulence is a complicated statistical phenomenon whereby small temperature (and to a much lesser extent, pressure) fluctuations result in index of refraction fluctuations. The random index of refraction fluctuations along the propagation path in turn result in random variations in the phase front of the beam. Traditionally, it has been assumed that near the ground the statistics of the index of refraction are isotropic (the same in all directions) and homogeneous (the same along the entire path) and that it follows the classical turbulence power law. With the recognition that the strength of optical turbulence is reduced with height above the surface, models have been developed to describe this behavior [1, 2] and changes made to propagation models to incorporate height dependence of the strength of turbulence (represented by the structure function constant, C_n^2) along the path [3]. However, theoreticians and engineers have still

assumed isotropy of the turbulence. Up until recently, this was a both a logical and expedient assumption. Methodologies and equipment were not easily available to determine anisotropy of the turbulence and mathematical models and simulations quickly become more labor intensive with the addition of anisotropy into propagation theory.

If these underlying assumptions are not correct, it could impact all technologies which utilize a laser propagating through the atmosphere. Some application areas include free-space optical (FSO) communications, satellite communications, high energy lasers, and imaging. The field of optical communications has gained much ground with the advent of fiber optics, however, in many situations it relies on either a low bandwidth system or FSO to carry the signal the “last mile.” Optical turbulence causes beam wander and scintillation, both of which increase fade of the optical communication signal. Satellite uplink and downlink optical communication systems suffer from the same fade issues as FSO. High Energy Laser (HEL) systems require that a high energy density is maintained on a fix spot long enough to damage the target. Corruption of the phase front of the beam from passage through optical turbulence increases the minimum attainable spot size at the focus of the beam reducing energy density on the target. Additionally, turbulence will cause the beam to wander preventing it from remaining on a fixed spot long enough to cause damage to the target. Beam spreading from turbulence causes degradation of the modulation transfer function of an imaging system resulting in

image blurring. Furthermore, turbulence induced beam wander will cause the image to “dance.” An accurate understanding of the defining statistics of optical turbulence will increase our ability to compensate for its effects. The engineering of an optical system can only be as good as our understanding of the atmospheric effects in which the system will be used.

In 1970, Consortini, et al [4] performed an experiment involving the propagation of three parallel 1 cm beams for 130 m. They found that the movement of the centroid of the beam due to atmospheric effects was different in the horizontal and vertical directions leading to the conclusion that the optical turbulence was anisotropic. For this experiment, they took short exposure photographic images to calculate beam movement. The measurements lacked the experimental accuracy possible in today’s technology but proved that there was a directional difference.

Kon [5] was the first to consider that the optical turbulence spectrum could be different in the horizontal and vertical directions and proposed a spectral model that included this difference.

Recently, the topic of anisotropy of the turbulence near the ground has gained much interest. Anisotropic turbulence could lead to significantly different beam statistics than that predicted based on isotropic turbulence. For that reason, it is important to develop methods to accurately detect anisotropy and to develop propagation theories that incorporate anisotropy. For instance, researchers at the University of Miami [6] recently found that the contours of

equal covariance of intensity of a spherical wave propagated near ground formed ellipses. They were able to successfully reproduce the behavior by assuming an anisotropic spectral model where the degree of anisotropy was maintained through all scale sizes in the inertial range of the turbulence spatial spectrum.

Based on the early work of Consortini, et al and Kon, and the more recent findings of University of Miami researchers, we began to study methods of measuring anisotropy of turbulence indirectly by the impact that it had on a propagated beam and to develop accompanying models and extend existing theory. We also considered the possibility that the spectral power law might differ from the classically assumed $\kappa^{-11/3}$. Chapter 2 of this dissertation summarizes the generation of optical turbulence developing the terminology and concepts necessary in this work. Similarly, in Chapter 3, we review the basic theory of beam propagation through a random media. Contributions of this work to the study of nonclassical, or generalized, turbulence and its effect on a beam are covered in Chapters 4-7. In Chapter 8, accomplishments during this study are reviewed and future of this study are considered.

CHAPTER 2: OPTICAL TURBULENCE

As a beam passes through the atmosphere, it is affected by changes in the index of refraction along its path. These changes can be both deterministic and stochastic in nature. The stochastic portion is referred to as optical turbulence. Optical turbulence refers to small random index of refraction changes resulting predominantly from small temperature changes originating from a turbulent velocity flow.

The atmosphere is a viscous fluid which is driven into motion via wind velocity. The resulting flow becomes turbulent when the Reynolds number $Re = Vl/\nu$ exceeds a critical value. In this equation V is the wind speed l is the relevant scale size and ν is the kinematic viscosity. Near the ground, the Reynolds number becomes quite large and as such the atmosphere is highly turbulent. As the wind energy feeds into the turbulent flow, subflows develop, called turbulent eddies (see Figure 1). The largest eddy size, or scale, of the turbulent flow is called the outer scale, denoted by L_0 . The eddies begin to deteriorate as soon as they are formed, breaking apart into smaller and smaller scales transferring energy at each stage within the inertial range until the inner scale, l_0 , is reached where the turbulent energy is dissipated into heat through viscosity. This process is described physically by the complicated Navier-Stokes equations. Because of the difficulty of solving these for problems of interest, the optical turbulence community has chosen to follow the methods first introduced

to describe turbulent flow by Kolmogorov [7] and later extended to the passive additive scalars of temperature and refractive index by Obukhov and Corssin [8, 9].

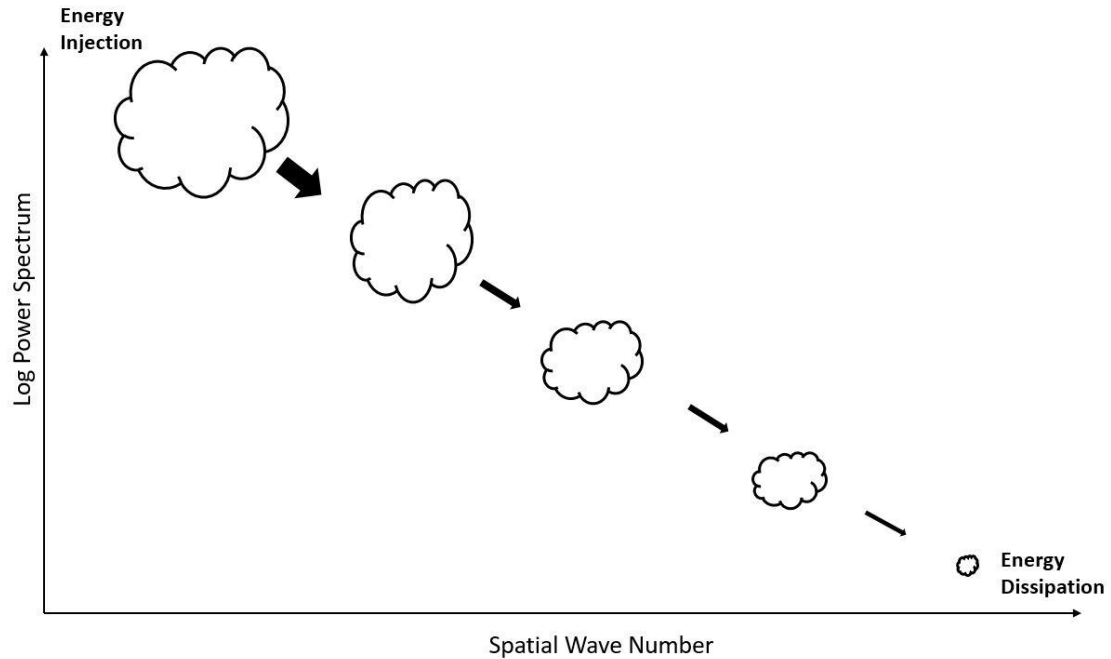


Figure 1. Cascade of energy between scale sizes from energy injection at outer scale to dissipation at inner scale. Plot shows power relationship between scale sizes. Note the logarithmic vertical axis.

Kolmogorov postulated that the longitudinal wind velocity structure function in the region between energy input (outer scale) and energy loss (inner scale) could be described by a universal law [10]. This region is predominantly characterized by energy transfer between the eddies with energy input only at the outer scale and energy loss only at the inner scale. Kolmogorov developed

this universal law through dimensional analysis of the velocity structure function parallel to two observation points \mathbf{R}_1 and \mathbf{R}_2 separated by distance $R = |\mathbf{R}_1 - \mathbf{R}_2|$.

The wind velocity structure function is given by

$$D_v(\mathbf{R}_1, \mathbf{R}_2) = \left\langle \left(v(\mathbf{R}_1) - v(\mathbf{R}_2) \right)^2 \right\rangle \quad (2.1)$$

where $\langle \bullet \rangle$ indicates ensemble average. Assuming statistical isotropy and homogeneity, the structure function becomes a function of separation distance, R . Kolmogorov postulated that the structure function should be a function of the dissipation rate, ε , which determines the rate at which energy is injected into and leaves the energy cascade. It must also have units of $(m/s)^2$ and should be a function of separation R . Assuming the simple form of

$$D_v(R) = C(\varepsilon R)^x \quad (2.2)$$

where C is a dimensionless constant, x is forced to take a value of 2/3 to meet the dimensional requirements. The more common form of the velocity structure function is

$$D_v(R) = C_v^2 R^{2/3}. \quad (2.3)$$

C_v^2 is the velocity structure constant with units of $m^{4/3}/s^2$. This equation is valid only within the inertial subrange, that is, for separation distances between the observation points such that $l_0 \ll R \ll L_0$. A Taylor series expansion of the structure function over short separations leads to a more complete form for the velocity structure function [3]

$$D_v(R) = \begin{cases} C_v^2 l_0^{-4/3} R^2, & 0 \leq R \ll l_0 \\ C_v^2 R^{2/3}, & l_0 \ll R \ll L_0 \end{cases} \quad (2.4)$$

The same type of dimensional analysis [10] leads to the fundamental velocity turbulence length, the inner scale, defined by

$$l_0 = 7.4 \left(\nu^3 / \varepsilon \right)^{1/4} \quad (2.5)$$

ν is viscosity. The quantity in parentheses is referred to as the Kolmogorov microscale.

Temperature passively follows velocity and thus where there is a turbulent velocity field, there is a corresponding stochastic temperature distribution with equations that follow the form of velocity. Namely, the temperature structure function follows

$$D_T(R) = \begin{cases} C_T^2 l_0^{-4/3} R^2, & 0 \leq R \ll l_0 \\ C_T^2 R^{2/3}, & l_0 \ll R \ll L_0 \end{cases} \quad (2.6)$$

The inner scale of temperature turbulence is similar to that of velocity and is given by [11]

$$l_0 = 5.8 \left(D^3 / \varepsilon \right)^{1/4} \quad (2.7)$$

where D is the diffusivity of heat in air.

The index of refraction is temperature dependent according to [12]

$$n(\mathbf{R}) = 1 + 79 \times 10^{-6} \left(1 + 7.52 \times 10^{-3} \lambda^{-2} \right) \frac{P(\mathbf{R})}{T(\mathbf{R})} \quad (2.8)$$

where λ is the wavelength and $P(\mathbf{R})$ and $T(\mathbf{R})$ represent pressure, in millibars, and temperature, in kelvin, at point \mathbf{R} . The index change is negligibly affected by

wavelength within the visible spectrum and for the cases of interest to this work, pressure fluctuations do not significantly contribute to index fluctuations. Instead, the index fluctuations are driven by temperature fluctuations. Therefore, along with the temperature structure function there is an analogous index of refraction structure function which according to Kolmogorov statistics is given by

$$D_n(R) = \begin{cases} C_n^2 l_0^{-4/3} R^2, & 0 \leq R \ll l_0 \\ C_n^2 R^{2/3}, & l_0 \ll R \ll L_0 \end{cases} \quad (2.9)$$

C_n^2 is the refractive index structure constant with units of $m^{-2/3}$ and indicates the strength of optical turbulence. C_n^2 is related to C_T^2 through the relationship [3]

$$C_n^2 = \left(79 \times 10^{-6} \frac{P}{T^2} \right) C_T^2 \quad (2.10)$$

Since it is easier to measure temperature than index of refraction, C_n^2 is often computed from C_T^2 where temperature changes are measured temporally using one or multiple fast response temperature probes spatially separated. The validity of this method is based on Taylor's frozen turbulence hypothesis which states that since the atmosphere is slow to change, differences in measurements at one location are caused by advection as turbulent eddies are blown past the receiver and not by changes in the quantities themselves. Furthermore, ergodicity and wide sense stationarity are assumed by sampling in time which is valid for short periods of time, on the order of 1-5 minutes. Another indirect method to determine C_n^2 is to measure the effect of the turbulence on an optical

beam and from the resulting beam scintillation calculate C_n^2 . Such a device is referred to as a scintillometer.

Equation (2.9) was generated from dimensional analysis rather than basic physics. While this method has met with amazing success, in this work we are going to consider slight variations from the Kolmogorov power law. Also, in arriving at this point, we have utilized the assumption of spatial statistical homogeneity and isotropy. While this thesis will not deal with the case of inhomogeneity, we will consider the mathematically more challenging case of statistical spatial anisotropy. In other words, we will consider that the defining statistics for the index of refraction are constant over the path (homogeneous) but can vary with direction (anisotropic). For instance, the strength of turbulence may be stronger in the vertical direction than in the horizontal direction.

The index of refraction can be broken into two terms, one representing a local mean index and the other a random component with a mean of zero such that

$$n(\mathbf{R}) = n_0(\mathbf{R}) + n_1(\mathbf{R}) \quad (2.11)$$

and $\langle n_1(\mathbf{R}) \rangle = 0$.

The spatial index of refraction covariance between two points is defined as

$$B_n(\mathbf{R}_1, \mathbf{R}_2) = \langle n(\mathbf{R}_1)n(\mathbf{R}_2) \rangle \quad (2.12)$$

which assuming spatial homogeneity can be written as

$$B_n(\mathbf{R}) = \langle n(\mathbf{R}_1)n(\mathbf{R}_1 + \mathbf{R}) \rangle \quad (2.13)$$

where $\mathbf{R} = \mathbf{R}_2 - \mathbf{R}_1$.

The spatial covariance and spatial power spectral density are Fourier transform pairs according to

$$B_n(\mathbf{R}) = \iiint_{-\infty}^{\infty} e^{i\mathbf{K} \cdot \mathbf{R}} \Phi_n(\mathbf{K}) d^3\mathbf{K} \quad (2.14)$$

$$\Phi_n(\mathbf{K}) = \left(\frac{1}{2\pi} \right)^3 \iiint_{-\infty}^{\infty} e^{-i\mathbf{K} \cdot \mathbf{R}} B_n(\mathbf{R}) d^3\mathbf{R} \quad (2.15)$$

$\mathbf{K} = (\kappa_x, \kappa_y, \kappa_z)$ is the spatial wavenumber vector and $\mathbf{R} = (x, y, z)$. This relates to the structure function through [13]

$$D_n(\mathbf{R}) = \iiint_{-\infty}^{\infty} \Phi_n(\mathbf{K}) [1 - \cos(\mathbf{K} \cdot \mathbf{R})] d^3\mathbf{K} \quad (2.16)$$

The classical power spectral density that results from Kolmogorov's dimensional analysis in an isotropic atmosphere is [3]

$$\Phi_n(\kappa) = 0.033 C_n^2 \kappa^{-11/3} \quad (2.17)$$

This form ignores spectral roll off and assumes an inner scale size that goes down to zero and an infinitely large outer scale.

There are various mathematical models that incorporate an inner and outer scale cutoff into the index of refraction power spectrum. Often the choice is made not in consideration of the physics but by mathematical tractability of the formulation. An inner scale cutoff can easily be incorporated with consideration of dissipation and was first utilized by Tatarskii [14]. von Karman added a mathematically tractable outer scale cutoff to Tatarskii's spectral representation

[3]. The result is a power spectrum model for the index of refraction with both inner and outer scale cutoffs referred to as the modified von Karman [3].

$$\Phi_n(\kappa) = 0.033C_n^2 \frac{\exp(-\kappa^2/\kappa_m^2)}{(\kappa^2 + \kappa_0^2)^{11/6}} \quad (2.18)$$

Here $\kappa_m = 5.92/l_0$ is the inner scale cutoff where 5.92 was chosen for energy conservation at l_0 . $\kappa_0 = 2\pi/L_0$ relates the spatial frequency of the outer scale of turbulence to its spatial distance dimension L_0 . The outer scale definition is somewhat obscure and may be defined somewhat differently depending upon the model.

In Chapter 3, we will derive the integral equations that describe the beam after propagation through random index of refraction fluctuations. In this derivation, we will utilize the spectral representation of the index variations which with integration becomes the power spectrum. In analysis, we will use a power spectrum model of similar form to (2.17) or (2.18).

CHAPTER 3: BEAM PROPAGATION THROUGH OPTICAL TURBULENCE

3.1 Free-Field Propagation

Propagation of a transverse electromagnetic wave in free space is described by the wave equation

$$\nabla^2 u = \frac{1}{c^2} \frac{\partial^2 u}{\partial t^2} \quad (3.1)$$

where the field $u(\mathbf{R}, t)$ is a function of space and time, c is the speed of light, and ∇^2 is the Laplacian operator defined in rectangular coordinates as

$$\nabla^2 u = \frac{\partial^2 u}{\partial x^2} + \frac{\partial^2 u}{\partial y^2} + \frac{\partial^2 u}{\partial z^2}. \quad (3.2)$$

Assuming a single frequency solution such that $u(\mathbf{R}, t) = U_0(\mathbf{R})e^{-i\omega t}$ where ω is angular frequency and $U_0(\mathbf{R})$ is the complex wave amplitude, (3.1) reduces to the Helmholtz equation

$$\nabla^2 U_0 + k^2 U_0 = 0. \quad (3.3)$$

One method of solving this is using the Huygens-Fresnel integral which in essence considers the field in the receiver plane to be a result of the integrated effect of spherical waves originating from each point of the source. Considering points in $\mathbf{R} = (\mathbf{r}, z)$ and $\mathbf{S} = (\mathbf{s}, 0)$ where \mathbf{r} and \mathbf{s} are transverse vectors in the

receiver and source planes, respectively, with propagation in the z direction, the Huygens-Fresnel integral is given by [3]

$$U_0(\mathbf{r}, z) = -2ik \int \int_{-\infty}^{\infty} G(\mathbf{s}, \mathbf{r}; z) U_0(\mathbf{s}, 0) d^2s \quad (3.4)$$

where the 0 subscript throughout indicates free-field values and $G(\mathbf{r}, \mathbf{s}, z)$ is the free-field Green's function

$$G(\mathbf{r}, \mathbf{s}, z) = \frac{e^{ik|\mathbf{R}-\mathbf{S}|}}{4\pi|\mathbf{R}-\mathbf{S}|}. \quad (3.5)$$

Equation (3.5) corresponds to a spherical wave originating at \mathbf{S} and propagating to \mathbf{R} . The geometry is shown in Figure 2.

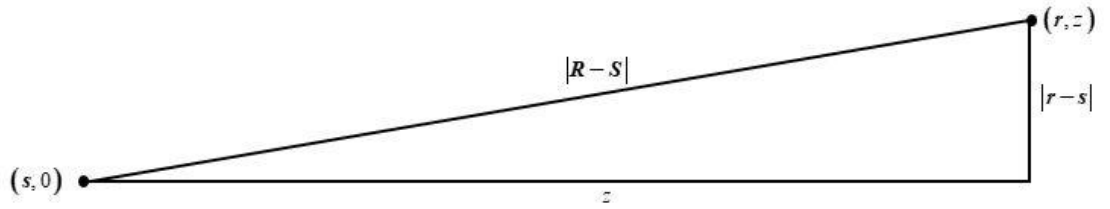


Figure 2. Propagation geometry between points \mathbf{s} and \mathbf{R} .

Recognizing that the transverse spread of an optical wave is small compared to propagation distance, as shown in Figure 2, we can approximate $|\mathbf{R}-\mathbf{S}|$ as follows.

$$\begin{aligned}
|\mathbf{R} - \mathbf{S}| &= \left(z^2 + |\mathbf{r} - \mathbf{s}|^2 \right)^{1/2} \\
&= z \left(1 + \frac{|\mathbf{r} - \mathbf{s}|^2}{z^2} \right)^{1/2}
\end{aligned} \tag{3.6}$$

Expressing equation (3.6) in a Taylor expansion and only keeping the first two terms since $|\mathbf{r} - \mathbf{s}| \ll z$,

$$\begin{aligned}
|\mathbf{R} - \mathbf{S}| &\cong z \left(1 + \frac{|\mathbf{r} - \mathbf{s}|^2}{2z^2} \right) \\
&= z + \frac{|\mathbf{r} - \mathbf{s}|^2}{2z}
\end{aligned} \tag{3.7}$$

Furthermore, approximating

$$\frac{1}{|\mathbf{R} - \mathbf{S}|} \cong \frac{1}{z} \tag{3.8}$$

equation (3.5) can be approximated by

$$G(\mathbf{r}, \mathbf{s}, z) \cong \frac{1}{4\pi z} \exp \left[ikz + \frac{ik|\mathbf{r} - \mathbf{s}|^2}{2z} \right] \tag{3.9}$$

3.2 Gaussian Solution in Free Field

A circularly symmetric Gaussian beam (TEM₀₀ laser mode) originating at the source can be expressed as

$$U_0(s) = a_0 \exp \left(-\frac{s^2}{W_0^2} - \frac{iks^2}{2F_0} \right) \tag{3.10}$$

Here, s corresponds to radial position where $s = \sqrt{x_s^2 + y_s^2}$, W_0 is the $1/e$ field beam radius and F_0 is the radius of curvature where $F_0 < 0$, $F_0 > 0$, $F_0 = \infty$ correspond to a divergent, focused, and collimated beam, respectively. The amplitude and phase vary across the beam according to

$$A_0 = a_0 \exp\left(-\frac{s^2}{W_0^2}\right) \quad (3.11)$$

and

$$\varphi_0 = -\frac{ks^2}{2F_0}. \quad (3.12)$$

Introducing the complex parameter

$$\alpha_0 = \frac{2}{kW_0^2} + i\frac{1}{F_0} \quad (3.13)$$

equation (3.10) becomes

$$U_0(s, 0) = a_0 \exp\left(-\frac{1}{2}\alpha_0 ks^2\right) \quad (3.14)$$

Substitution of Equations (3.9) and (3.10) into Equation (3.4), yields a free-field solution of

$$U_0(r, z) = \frac{1}{1 + i\alpha_0 z} \exp\left[ikz + \frac{ik}{2z}\left(\frac{i\alpha_0 z}{1 + i\alpha_0 z}\right)r^2\right] \quad (3.15)$$

r corresponds to the radial distance from the beam center in the receiver plane

which can be expressed in Cartesian coordinates as $r = \sqrt{x_r^2 + y_r^2}$.

Introduction of beam parameters [3] simplifies future analysis. From the source plane, they are defined as

$$\Theta_0 = 1 - \frac{z}{F_0}, \quad \Lambda_0 = \frac{2z}{kW_0^2}. \quad (3.16)$$

Θ_0 corresponds to refractive characteristics of the beam and Λ_0 to diffraction.

Writing equation (3.14) in terms of the beam parameters and in a more physically representative form

$$U_0(r, z) = \frac{1}{\sqrt{\Theta_0^2 + \Lambda_0^2}} \exp\left(-\frac{r^2}{W^2}\right) \exp\left[i\left(kz - \varphi - \frac{kr^2}{2F}\right)\right]. \quad (3.17)$$

Noting that (3.17) is in the same form as the starting beam, we can easily identify the beam $1/e$ radius W , the longitudinal phase shift φ resulting from propagating the distance z , and the new radius of curvature F where

$$\varphi = \tan^{-1}\left(\frac{\Lambda_0}{\Theta_0}\right) \quad (3.18)$$

$$W = W_0 \sqrt{\Theta_0^2 + \Lambda_0^2} \quad (3.19)$$

$$F = \frac{kW_0^2}{2} \left[\frac{\Lambda_0(\Theta_0^2 + \Lambda_0^2)}{\Theta_0(1 - \Theta_0) - \Lambda_0^2} \right] \quad (3.20)$$

Intensity is the squared magnitude of the field

$$I^0(r, z) = U_0(r, z)U_0^*(r, z) \quad (3.21)$$

which for propagation of a Gaussian beam becomes

$$I^0(r, z) = \left(\frac{1}{\Theta_0^2 + \Lambda_0^2}\right) \exp\left(-\frac{2r^2}{W^2}\right). \quad (3.22)$$

This same solution can be expressed in terms of receiver beam parameters Θ and Λ (Figure 3) where

$$\Theta = \frac{\Theta_0}{\Theta_0^2 + \Lambda_0^2}, \quad \bar{\Theta} = 1 - \Theta, \quad \Lambda = \frac{\Lambda_0}{\Theta_0^2 + \Lambda_0^2}. \quad (3.23)$$

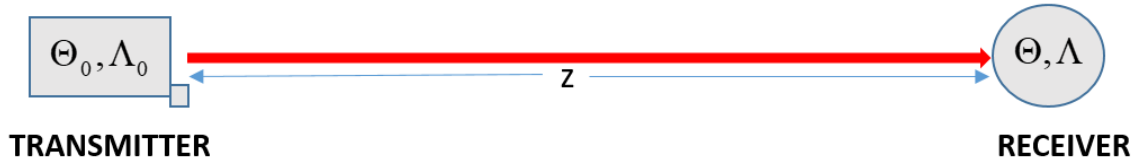


Figure 3. Relationship between transmitter and receiver beam parameters.

This results in the solution at the receiver plane for propagation of a Gaussian source beam as

$$U_0(r, z) = \sqrt{\Theta^2 + \Lambda^2} \exp\left(-\frac{r^2}{W^2}\right) \exp\left[i\left(kz - \varphi - \frac{kr^2}{2F}\right)\right] \quad (3.24)$$

and

$$W = \sqrt{\frac{2z}{k\Lambda}}, \quad F = -\frac{z}{\Theta} \quad (3.25)$$

with analogous definitions to those of Θ_0 and Λ_0 of

$$\Theta = 1 + \frac{z}{F} \quad \Lambda = \frac{2z}{kW^2} \quad (3.26)$$

We can also define φ , W and F in terms of the receiver plane parameters

$$\varphi = \tan^{-1}\left(\frac{\Lambda}{\Theta}\right) \quad (3.27)$$

$$W = \frac{W_0}{\sqrt{\Theta^2 + \Lambda^2}} \quad (3.28)$$

$$F = \frac{F_0 (\Theta^2 + \Lambda^2 - \Theta)}{(\Theta - 1)(\Theta^2 + \Lambda^2)} \quad (3.29)$$

The free-field intensity in terms of receiver parameters is

$$I^0(r, z) = (\Theta^2 + \Lambda^2) \exp\left(-\frac{2r^2}{W^2}\right) \quad (3.30)$$

3.3 Propagation through Random Media

As a coherent source propagates through random index of refraction fluctuations, as occur in the atmosphere, its phase front is distorted. This appears as beam broadening, loss of spatial coherence and intensity fluctuations (*scintillation*) where the beam cross section consists of bright and dark patches. The theory for studying propagation through optical turbulence is divided according to the strength of fluctuations. Research in this thesis is limited to the *weak irradiance fluctuation regime* where the Rytov approximation has proved to be a reliable means of analysis. Extension into moderate to strong turbulence requires use of either extended Rytov theory [3] or wave optics simulation where the turbulence is considered to occur at multiple phase screens placed along the path with free-field propagation between the screens.

In general, the weak fluctuation regime is defined by conditions such that the scintillation index of a plane wave after propagating through the medium

(Rytov variance) is less than one. Using the Rytov approximation with the Kolmogorov spectrum the Rytov variance is calculated to be

$$\sigma_R^2 = 1.23 C_n^2 k^{7/6} L^{11/6} \quad (3.31)$$

For a Gaussian beam, as considered in this work, the further requirement is that

$\sigma_I^2 < 1$ across the entire beam where σ_I^2 is normalized variance of intensity (scintillation index).

In propagation through a medium with stochastic index of refraction, the defining Helmholtz equation is

$$\nabla^2 U + k^2 n^2(\mathbf{R}) U = 0 \quad (3.32)$$

where U is the perturbed field.

There are two perturbation methods used to solve (3.32), the Born and Rytov approximations. The Born approximation, which assumes that the perturbed field is the *sum* of the free-field solution plus higher order perturbation terms has proven to be inaccurate. The Rytov approximation assumes a product of the free field solution and a phase term which incorporates perturbations and has been proven a good match to experimental data for weak irradiance fluctuations [3]. The Born method will be shown as a step in the development of the more complicated Rytov method.

As shown in Equation (2.11), the index of refraction can be broken into the sum of a constant plus a random component. Then

$$n^2(\mathbf{R}) = [n_0 + n_1(\mathbf{R})]^2 \quad (3.33)$$

In the atmosphere, $n_0 \cong 1$ and the random fluctuations are small so $|n_1(\mathbf{R})| \ll 1$.

Defining n_0 as the mean index, $\langle n_1(\mathbf{R}) \rangle = 0$. In that case, the index can be approximated by

$$n^2(\mathbf{R}) \cong 1 + 2n_1(\mathbf{R}) \quad (3.34)$$

The Born perturbation method assumes that the perturbed field after propagating distance $z = L$ can be represented as the sum of the free-field beam plus a scattered component plus higher order scattered components.

$$U(\mathbf{R}) = U_0(\mathbf{R}) + U_1(\mathbf{R}) + U_2(\mathbf{R}) + \dots \quad (3.35)$$

Introducing a small perturbation term, ε , into (3.34) and (3.35) helps with identifying the order of terms. In this case,

$$n(\mathbf{R}) \cong 1 + 2\varepsilon n_1(\mathbf{R}) \quad (3.36)$$

and

$$U(\mathbf{R}) = U_0(\mathbf{R}) + \varepsilon U_1(\mathbf{R}) + \varepsilon^2 U_2(\mathbf{R}) + \dots \quad (3.37)$$

Substituting (3.36) and (3.37) into the stochastic Helmholtz equation, (3.32), and then equating terms with the same order of perturbation yields a set of differential equations of the form

$$\nabla^2 U_0 + k^2 U_0 = 0 \quad (3.38)$$

$$\nabla^2 U_1 + k^2 U_1 = -2k^2 n_1(\mathbf{R}) U_0(\mathbf{R}) \quad (3.39)$$

$$\nabla^2 U_2 + k^2 U_2 = -2k^2 n_1(\mathbf{R}) U_1(\mathbf{R}) \quad (3.40)$$

and so on.

The first equation is the free-field equation as in (3.4) which we have already solved. The defining differential equations for all perturbations have the same form and can be solved by the method of Green's function where

$$U_m(\mathbf{R}) = \iiint G(\mathbf{S}, \mathbf{R}) [2k^2 n_1(\mathbf{S}) U_{m-1}(\mathbf{S})] d^3 S \quad (3.41)$$

$G(\mathbf{S}, \mathbf{R})$ is the Green's function defined in Equation (3.9).

Defining the cylindrical coordinates $\mathbf{S} = (s, z)$ and $\mathbf{R} = (\mathbf{r}, L)$ where L is the path length and recognizing that $z \rightarrow L - z$ in the paraxial approximation, equation (3.41) becomes

$$U_m(\mathbf{r}, L) = \frac{k^2}{2\pi} \int_0^L dz \int_{-\infty}^{\infty} d^2 s \exp \left[ik(L - z) + \frac{ik|s - \mathbf{r}|^2}{2(L - z)} \right] \frac{n_1(s, z)}{L - z} U_{m-1}(s, z) \quad (3.42)$$

In contrast to the Born approximation, the Rytov approximation [3] assumes that the perturbed field can be expressed as the product of the free-field solution and a complex exponential perturbation term

$$U(\mathbf{r}, L) = U_0(\mathbf{r}, L) \exp[\psi(\mathbf{r}, L)] \quad (3.43)$$

where

$$\psi(\mathbf{r}, L) = \psi_1(\mathbf{r}, L) + \psi_2(\mathbf{r}, L) + \dots \quad (3.44)$$

To relate this back to the Born solution given by Equation (3.42), we define a normalized Born perturbation

$$\phi_m(\mathbf{r}, L) = \frac{U_m(\mathbf{r}, L)}{U_0(\mathbf{r}, L)}, \quad m = 1, 2, 3, \dots \quad (3.45)$$

Equating the first-order Rytov and first-order Born solutions from Equations (3.35) and (3.43)

$$U_0(\mathbf{r}, L) \exp[\psi_1(\mathbf{r}, L)] = U_0(\mathbf{r}, L) + U_1(\mathbf{r}, L) \quad (3.46)$$

or

$$\psi_1(\mathbf{r}, L) = \ln[1 + \phi_1(\mathbf{r}, L)] \quad (3.47)$$

Assuming small perturbations, $|\phi_1(\mathbf{r}, L)| \ll 1$. Approximating the natural logarithm up to the first order yields

$$\psi_1(\mathbf{r}, L) \cong \phi_1(\mathbf{r}, L) \quad (3.48)$$

which with substitution into (3.42) gives

$$\psi_1(\mathbf{r}, L) = \frac{k^2}{2\pi} \int_0^L dz \iint_{-\infty}^{\infty} d^2s \exp \left[ik(L-z) + \frac{ik|\mathbf{s}-\mathbf{r}|^2}{2(L-z)} \right] \frac{n_1(\mathbf{s}, z)}{(L-z)} \frac{U_0(\mathbf{s}, z)}{U_0(\mathbf{r}, L)} \quad (3.49)$$

Note that since $\langle n_1(\mathbf{s}, z) \rangle = 0$, $\langle \psi_1(\mathbf{r}, L) \rangle = \langle \phi_1(\mathbf{r}, L) \rangle = 0$. This is not the case for higher order perturbations.

To evaluate the second-order perturbation, we equate the fields from first and second-order Rytov and Born perturbations.

$$U_0(\mathbf{r}, L) \exp[\psi_1(\mathbf{r}, L) + \psi_2(\mathbf{r}, L)] = U_0(\mathbf{r}, L) + U_1(\mathbf{r}, L) + U_2(\mathbf{r}, L) \quad (3.50)$$

or

$$\psi_1(\mathbf{r}, L) + \psi_2(\mathbf{r}, L) = \ln[1 + \phi_1(\mathbf{r}, L) + \phi_2(\mathbf{r}, L)] \quad (3.51)$$

Keeping through the second order terms of the natural logarithm yields

$$\begin{aligned}
\psi_1(\mathbf{r}, L) + \psi_2(\mathbf{r}, L) &\cong \phi_1(\mathbf{r}, L) + \phi_2(\mathbf{r}, L) - \frac{[\phi_1(\mathbf{r}, L) + \phi_2(\mathbf{r}, L)]^2}{2} \\
&\cong \phi_1(\mathbf{r}, L) + \phi_2(\mathbf{r}, L) - \frac{\phi_1^2(\mathbf{r}, L)}{2}
\end{aligned} \tag{3.52}$$

where perturbation terms higher than second order have been discarded.

Simplifying, the second order Rytov perturbation becomes

$$\psi_2(\mathbf{r}, L) = \phi_2(\mathbf{r}, L) - \frac{\phi_1^2(\mathbf{r}, L)}{2} \tag{3.53}$$

From the Born approximation

$$\begin{aligned}
\phi_2(\mathbf{r}, L) &= \frac{k^2}{2\pi} \int_0^L dz \int \int_{-\infty}^{\infty} d^2s \exp \left[ik(L-z) + \frac{ik|s-\mathbf{r}|^2}{2(L-z)} \right] \frac{n_1(s, z)}{(L-z)} \frac{U_1(s, z)}{U_0(\mathbf{r}, L)} \\
&= \frac{k^2}{2\pi} \int_0^L dz \int \int_{-\infty}^{\infty} d^2s \exp \left[ik(L-z) + \frac{ik|s-\mathbf{r}|^2}{2(L-z)} \right] \frac{n_1(s, z)}{(L-z)} \frac{U_0(s, z)\phi_1(s, z)}{U_0(\mathbf{r}, L)}
\end{aligned} \tag{3.54}$$

3.3.1 Spectral Representations

To evaluate ϕ_1 and ϕ_2 we will use a spatial wavenumber (spectral) representation for n_1 . We turn to the Riemann-Stieltjes integral representation and write the refractive index fluctuations as [3]

$$n_1(s, z) = \int \int_{-\infty}^{\infty} \exp(i\mathbf{K} \cdot \mathbf{s}) d\nu(\mathbf{K}, z) \tag{3.55}$$

where $\mathbf{K} = (\kappa_x, \kappa_y, 0)$ is the three-dimensional dimensional wave vector with $\kappa_z = 0$ and $d\nu(\mathbf{K}, z)$ is the amplitude of random index of refraction fluctuations corresponding to the spatial-wave number \mathbf{K} .

For a Gaussian beam

$$\frac{U_0(s, z)}{U_0(r, L)} = \frac{1 + i\alpha_0 L}{1 + i\alpha_0 z} \exp[ik(z - L)] \exp\left[-\frac{\alpha_0 k s^2}{2(1 + i\alpha_0 z)}\right] \exp\left[\frac{\alpha_0 k r^2}{2(1 + i\alpha_0 L)}\right] \quad (3.56)$$

Expanding $|s - \mathbf{r}|^2 = s^2 - 2\mathbf{r} \cdot \mathbf{s} + r^2$ where unbolded indicates magnitude and (\cdot) is the dot product, defining

$$\gamma = \frac{1 + i\alpha_0 z}{1 + i\alpha_0 L} \quad (3.57)$$

and substituting (3.55) and (3.56) into (3.49), the first order Born perturbation becomes

$$\begin{aligned} \phi_1(\mathbf{r}, L) = & \frac{k^2}{2\pi} \int_0^L dz \int_{-\infty}^{\infty} d^2s \exp[ik(L - z)] \exp\left(-\frac{i\mathbf{r} \cdot \mathbf{s}}{L - z}\right) \left(\frac{1}{\gamma(L - z)}\right) \exp[ik(z - L)] \\ & \times \exp\left[\frac{iks^2}{2\gamma(L - z)}\right] \exp\left[\frac{i\gamma k r^2}{2(L - z)}\right] \int_{-\infty}^{\infty} \exp(i\mathbf{K} \cdot \mathbf{s}) d\nu(\mathbf{K}, z) \end{aligned} \quad (3.58)$$

Combining like terms and rearranging,

$$\phi_1(\mathbf{r}, L) = \frac{k^2}{2\pi} \int_0^L dz \int_{-\infty}^{\infty} \frac{d\nu(\mathbf{K}, z)}{\gamma(L - z)} \exp\left[\frac{i\gamma k r^2}{2(L - z)}\right] \int_{-\infty}^{\infty} d^2s \exp\left[i\left(\mathbf{K} - \frac{k\mathbf{r}}{L - z}\right) \cdot \mathbf{s}\right] \exp\left[\frac{iks^2}{2\gamma(L - z)}\right] \quad (3.59)$$

Changing to polar coordinates, the last pair of integrals evaluate to

$$\begin{aligned} & \int_{-\infty}^{\infty} d^2s \exp\left[i\left(\mathbf{K} - \frac{k\mathbf{r}}{L - z}\right) \cdot \mathbf{s}\right] \exp\left[\frac{iks^2}{2\gamma(L - z)}\right] \\ & = \frac{2\pi i\gamma}{k} (L - z) \exp\left[i\gamma \mathbf{K} \cdot \mathbf{r} - \frac{i\mathbf{K}^2 \gamma}{2k} (L - z)\right] \exp\left[-\frac{i\gamma k r^2}{2(L - z)}\right] \end{aligned} \quad (3.60)$$

With substitution of the evaluated integral pair, we find the spectral representation for the first order Rytov perturbation to be

$$\psi_1(\mathbf{r}, L) = \phi_1(\mathbf{r}, L) = ik \int_0^L dz \int_{-\infty}^{\infty} dv(\mathbf{K}, z) \exp \left[i\gamma \mathbf{K} \cdot \mathbf{r} - \frac{iK^2 \gamma}{2k} (L - z) \right] \quad (3.61)$$

Substituting the above derived expression for $\phi_1(\mathbf{r}, L)$ as well (3.55) and (3.56) into (3.54), we find the spectral representation of the second order Born perturbation to be

$$\begin{aligned} \phi_2(\mathbf{r}, L) = & \frac{ik^3}{2\pi} \int_0^L dz \int_0^L dz' \int_{-\infty}^{\infty} \int_{-\infty}^{\infty} \frac{dv(\mathbf{K}, z) dv(\mathbf{K}', z')}{\gamma(L - z)} \exp \left[\frac{i\gamma k r^2}{2(L - z)} - \frac{i\gamma' k'^2}{2k} (z - z') \right] \\ & \times \int_{-\infty}^{\infty} d^2 s \exp \left[i s \cdot \left(\mathbf{K} + \gamma' \mathbf{K}' - \frac{k\mathbf{r}}{L - z} \right) \right] \exp \left[\frac{iks^2}{2\gamma(L - z)} \right] \end{aligned} \quad (3.62)$$

In this expression, $\gamma' = \frac{1 + i\alpha_0 z'}{1 + i\alpha_0 z}$. As previously, the last integral pair in (3.62) can

be evaluated using (3.60) with the substitution $\mathbf{K} \rightarrow \mathbf{K} + \gamma' \mathbf{K}'$. This gives a second order Born spectral representation of

$$\begin{aligned} \phi_2(\mathbf{r}, L) = & -k^2 \int_0^L dz \int_0^L dz' \int_{-\infty}^{\infty} \int_{-\infty}^{\infty} dv(\mathbf{K}, z) dv(\mathbf{K}', z') \\ & \times \exp \left[i\gamma (\mathbf{K} + \gamma' \mathbf{K}') \cdot \mathbf{r} - \frac{i\gamma |\mathbf{K} + \gamma' \mathbf{K}'|^2}{2k} (L - z) - \frac{i\gamma' k'^2}{2k} (z - z') \right] \end{aligned} \quad (3.63)$$

Using (3.53), we now also have the spectral representation for the second order Rytov perturbation.

3.3.2 Derivation of Relevant Statistical Moments

The mean intensity, covariance of intensity, and scintillation index are comprised of three statistical moments. These are

$$\begin{aligned} E_1(\mathbf{r}, \mathbf{r}) &= \langle \phi_2(\mathbf{r}, L) \rangle = \langle \psi_2(\mathbf{r}, L) \rangle + \frac{1}{2} \langle \psi_1^2(\mathbf{r}, L) \rangle \\ E_2(\mathbf{r}_1, \mathbf{r}_2) &= \langle \phi_1(\mathbf{r}_1, L) \phi_1^*(\mathbf{r}_2, L) \rangle = \langle \psi_1(\mathbf{r}_1, L) \psi_1^*(\mathbf{r}_2, L) \rangle \\ E_3(\mathbf{r}_1, \mathbf{r}_2) &= \langle \phi_1(\mathbf{r}_1, L) \phi_1(\mathbf{r}_2, L) \rangle = \langle \psi_1(\mathbf{r}_1, L) \psi_1(\mathbf{r}_2, L) \rangle \end{aligned} \quad (3.64)$$

where \mathbf{r}_1 and \mathbf{r}_2 are points in the plane transverse to the direction of propagation and the asterisk indicates complex conjugate.

Solving for $E_2(\mathbf{r}_1, \mathbf{r}_2)$ using (3.61)

$$\begin{aligned} E_2(\mathbf{r}_1, \mathbf{r}_2) &= k^2 \int_0^L dz \int_0^L dz' \iint_{-\infty}^{\infty} \iint_{-\infty}^{\infty} \langle d\nu(\mathbf{K}, z) d\nu^*(\mathbf{K}', z') \rangle \\ &\times \exp \left[i\gamma(z) \mathbf{K} \cdot \mathbf{r}_1 - i\gamma^*(z') \mathbf{K}' \cdot \mathbf{r}_2 - \frac{i\kappa^2 \gamma(z)}{2k} (L - z) + \frac{i\kappa'^2 \gamma^*(z')}{2k} (L - z') \right] \end{aligned} \quad (3.65)$$

where we have indicated that γ is a function of position.

Statistical homogeneity of the refractive index implies

$$\langle d\nu(\mathbf{K}, z) d\nu^*(\mathbf{K}', z') \rangle = F_n(\mathbf{K}, |z - z'|) \delta(\mathbf{K} - \mathbf{K}') d^2\kappa d^2\kappa'. \quad (3.66)$$

where $\delta(\mathbf{K} - \mathbf{K}')$ is the delta function and $F_n(\mathbf{K}, |z - z'|)$ is the two-dimensional power spectral density with the transform pair relation [3]

$$\begin{aligned} F_n(\kappa_x, \kappa_y, 0, |z|) &= \int_{-\infty}^{\infty} \Phi_n(\kappa_x, \kappa_y, \kappa_z) \cos(z\kappa_z) d\kappa_z \\ \Phi_n(\kappa_x, \kappa_y, \kappa_z) &= \frac{1}{2\pi} \int_{-\infty}^{\infty} F_n(\kappa_x, \kappa_y, 0, |z|) \cos(z\kappa_z) dz \end{aligned} \quad (3.67)$$

The second expression reduces for the case $\kappa_z = 0$ to

$$\int_{-\infty}^{\infty} F_n(\mathbf{K}, z) dz = 2\pi \Phi_n(\mathbf{K}). \quad (3.68)$$

Substituting (3.66) into the expression for $E_2(\mathbf{r}_1, \mathbf{r}_2)$ and using the sifting property of the delta function gives

$$\begin{aligned} E_2(\mathbf{r}_1, \mathbf{r}_2) = & k^2 \int_{-\infty}^{\infty} d^2 \kappa \int_0^L dz \int_0^L dz' F_n(\mathbf{K}, |z - z'|) \\ & \times \exp \left[i\gamma(z) \mathbf{K} \cdot \mathbf{r}_1 - i\gamma^*(z') \mathbf{K}' \cdot \mathbf{r}_2 - \frac{i\kappa^2 \gamma(z)}{2k} (L - z) + \frac{i\kappa'^2 \gamma^*(z')}{2k} (L - z') \right] \end{aligned} \quad (3.69)$$

Since $F_n(\mathbf{K}, |z - z'|)$ has significant value for $|z - z'|$ less than the correlation width, $z \cong z'$ and the limits of integration on z' can be extended without significantly affecting the results. Making the change of variables

$$\mu = z - z', \quad \eta = \frac{z + z'}{2} \cong z \cong z' \quad (3.70)$$

and rearranging the order of integration, the expression for E_2 becomes

$$E_2(\mathbf{r}_1, \mathbf{r}_2) = k^2 \int_{-\infty}^{\infty} d^2 \kappa \int_0^L d\eta \exp \left[i\mathbf{K} \cdot (\gamma \mathbf{r}_1 - \gamma^* \mathbf{r}_2) - \frac{i\kappa^2 (\gamma - \gamma^*)}{2k} (L - \eta) \right] \int_{-\infty}^{\infty} d\mu F_n(\mathbf{K}, |\mu|) \quad (3.71)$$

where $\gamma = \gamma(\eta)$. Recalling the last integral from equation (3.68) and rearranging the order of integration, this becomes

$$E_2(\mathbf{r}_1, \mathbf{r}_2) = 2\pi k^2 \int_0^L d\eta \int_{-\infty}^{\infty} d^2 \kappa \Phi_n(\mathbf{K}) \exp \left[i\mathbf{K} \cdot (\gamma \mathbf{r}_1 - \gamma^* \mathbf{r}_2) - \frac{i\kappa^2 (\gamma - \gamma^*)}{2k} (L - \eta) \right] \quad (3.72)$$

Following the same logic that we used in arriving at the equation for $E_2(r_1, r_2)$ we can solve for $E_3(r_1, r_2)$ where we use the fact that $n_1(s, z) = n_1^*(s, z)$ is a real function and utilize the Fourier transform property of conjugation so that

$$\begin{aligned}\langle d\nu(\mathbf{K}, z)d\nu(\mathbf{K}', z') \rangle &= \langle d\nu(\mathbf{K}, z)d\nu^*(-\mathbf{K}', z') \rangle \\ &= F_n(\mathbf{K}, |z - z'|) \delta(\mathbf{K} + \mathbf{K}') d^2\kappa d^2\kappa'\end{aligned}\quad (3.73)$$

In which case,

$$E_3(r_1, r_2) = -2\pi k^2 \int_0^L d\eta \int \int_{-\infty}^{\infty} d^2\kappa \Phi_n(\mathbf{K}) \exp \left[i\gamma \mathbf{K} \cdot (\mathbf{r}_1 - \mathbf{r}_2) - \frac{i\kappa^2 \gamma}{k} (L - \eta) \right]. \quad (3.74)$$

Using equation (3.63) and realizing that $\gamma' = \frac{1 + i\alpha_0 z'}{1 + i\alpha_0 z} \cong 1$ since $z \cong z'$ we

can solve for the statistical moment $E_1(r, r)$.

$$E_1(r, r) = -\pi k^2 \int_0^L d\eta \int \int_{-\infty}^{\infty} d^2\kappa \Phi_n(\mathbf{K}). \quad (3.75)$$

Since E_1 is not a function of r , $E_1(r, r) = E_1(0, 0)$. We will use the latter expression in the remainder of this work. Furthermore, because of the assumed homogeneity of the propagation path,

$$E_1(r, r) = -\pi k^2 L \int \int_{-\infty}^{\infty} d^2\kappa \Phi_n(\mathbf{K}) \quad (3.76)$$

3.3.3 Field Moments

In deriving the field moments, we will need to compute the exponential of expected values. This is readily done by taking advantage of a statistical relationship that is derived through the method of cumulants [3]. Namely,

$$\langle \exp(\psi) \rangle \cong \exp \left[\langle \psi \rangle + \frac{1}{2} (\langle \psi^2 \rangle - \langle \psi \rangle^2) \right] \quad (3.77)$$

It is easily shown that the mean field quickly drops to zero with propagation, however, higher order statistics do not.

3.3.3.1 Mean Intensity

The mean intensity is a second order field moment defined as

$$\begin{aligned} \langle I(\mathbf{r}, L) \rangle &= \langle U_0(\mathbf{r}, L) \exp[\psi(\mathbf{r}, L)] U_0^*(\mathbf{r}, L) \exp[\psi^*(\mathbf{r}, L)] \rangle \\ &= U_0(\mathbf{r}, L) U_0^*(\mathbf{r}, L) \langle \exp[\psi(\mathbf{r}, L) + \psi^*(\mathbf{r}, L)] \rangle \end{aligned} \quad (3.78)$$

The first part of which is simply the free-field intensity defined in equation (3.22).

Using the relationship found in (3.77),

$$\langle \exp[\psi(\mathbf{r}, L) + \psi^*(\mathbf{r}, L)] \rangle = \exp[2E_1(0, 0) + E_2(\mathbf{r}, \mathbf{r})] \quad (3.79)$$

And thus

$$\langle I(\mathbf{r}, L) \rangle = \left(\frac{1}{\Theta_0^2 + \Lambda_0^2} \right) \exp \left(-\frac{2r^2}{W^2} \right) \exp[2E_1(0, 0) + E_2(\mathbf{r}, \mathbf{r})] \quad (3.80)$$

It is convenient to express this as

$$\begin{aligned}
\langle I(\mathbf{r}, L) \rangle &= \left(\frac{1}{\Theta_0^2 + \Lambda_0^2} \right) \exp\left(-\frac{2r^2}{W^2}\right) \exp[2\sigma_r^2(\mathbf{r}, L) - T] \\
&= \left(\frac{1}{\Theta_0^2 + \Lambda_0^2} \right) \exp(-T) \exp\left(-\frac{2r^2}{W^2}\right) \exp[2\sigma_r^2(\mathbf{r}, L)]
\end{aligned} \tag{3.81}$$

where

$$T = -2E_1(0, 0) - E_2(0, 0) \tag{3.82}$$

and

$$\sigma_r^2(\mathbf{r}, L) = \frac{1}{2} [E_2(\mathbf{r}, \mathbf{r}) - E_2(0, 0)] \tag{3.83}$$

or

$$\sigma_r^2(\mathbf{r}, L) = \pi k^2 L \int_0^1 d\xi \int \int_{-\infty}^{\infty} d^2\kappa \Phi_n(\mathbf{K}) \exp\left(-\frac{\kappa^2 \Lambda L}{k} \xi^2\right) [\exp(2\Lambda \xi \mathbf{K} \cdot \mathbf{r}) - 1] \tag{3.84}$$

In this representation, T is independent of radial position and describes the on-axis change in intensity caused by turbulence and $\sigma_r^2(\mathbf{r}, L)$ describes the radial change in intensity caused by the turbulence.

Rather than absolute magnitude of the mean intensity, we will be interested in the radial variation in intensity resulting from propagation in a random media. So, for simplification we will drop the leading radially constant terms and redefine the mean intensity in its normalized form.

$$\langle I(\mathbf{r}, L) \rangle = \exp\left(-\frac{2r^2}{W^2}\right) \exp[2\sigma_r^2(\mathbf{r}, L)] \tag{3.85}$$

3.3.3.2 Second Order Moments of Intensity

In this work, we will be interested in the fourth order field moment of covariance of intensity and the special covariance case of scintillation index. The covariance of intensity is defined as a covariance divided by the product of the mean intensity at each point [3]

$$B_I(\mathbf{r}_1, \mathbf{r}_2) = \frac{\langle I(\mathbf{r}_1)I(\mathbf{r}_2) \rangle - \langle I(\mathbf{r}_1) \rangle \langle I(\mathbf{r}_2) \rangle}{\langle I(\mathbf{r}_1) \rangle \langle I(\mathbf{r}_2) \rangle} \quad (3.86)$$

or

$$B_I(\mathbf{r}_1, \mathbf{r}_2) = \frac{\langle I(\mathbf{r}_1)I(\mathbf{r}_2) \rangle}{\langle I(\mathbf{r}_1) \rangle \langle I(\mathbf{r}_2) \rangle} - 1 \quad (3.87)$$

Under the assumption of Gaussian statistics, early atmospheric propagation researchers focused on log amplitude statistics where the log amplitude of the optical wave is related to the Rytov phase perturbations by [3]

$$\chi(\mathbf{r}) = \frac{1}{2} [\psi(\mathbf{r}) + \psi^*(\mathbf{r})] \quad (3.88)$$

Inclusion of second order perturbations results in third and fourth order terms which are not included in a second order analysis. Thus, only the first order phase perturbation is needed and we define the first order log amplitude perturbation as

$$\chi_1(\mathbf{r}) = \frac{1}{2} [\psi_1(\mathbf{r}) + \psi_1^*(\mathbf{r})] \quad (3.89)$$

The log-amplitude covariance is then

$$\begin{aligned}
B_{\chi}(\mathbf{r}_1, \mathbf{r}_2) &= \langle \chi_1(\mathbf{r}_1) \chi_1(\mathbf{r}_2) \rangle - \langle \chi_1(\mathbf{r}_1) \rangle \langle \chi_1(\mathbf{r}_2) \rangle \\
&= \frac{1}{2} \text{Re} [E_2(\mathbf{r}_1, \mathbf{r}_2) + E_3(\mathbf{r}_1, \mathbf{r}_2)]
\end{aligned} \tag{3.90}$$

where Re denotes the real part and terms higher than second order have been dropped. The covariance of intensity can be approximated by

$$B_I(\mathbf{r}_1, \mathbf{r}_2) = 4B_{\chi}(\mathbf{r}_1, \mathbf{r}_2) \text{ [3] and thus}$$

$$B_I(\mathbf{r}_1, \mathbf{r}_2) = 2 \text{Re} [E_2(\mathbf{r}_1, \mathbf{r}_2) + E_3(\mathbf{r}_1, \mathbf{r}_2)]. \tag{3.91}$$

The scintillation index $\sigma_I^2(\mathbf{r})$ is the normalized variance of intensity.

$$\begin{aligned}
\sigma_I^2(\mathbf{r}) &= \frac{\langle I^2(\mathbf{r}) \rangle - \langle I(\mathbf{r}) \rangle^2}{\langle I(\mathbf{r}) \rangle^2} \\
&= \frac{\langle I^2(\mathbf{r}) \rangle}{\langle I(\mathbf{r}) \rangle^2} - 1
\end{aligned} \tag{3.92}$$

Comparing this to Equation (3.87), we see that the covariance of intensity reduces to the scintillation index when $\mathbf{r}_1 = \mathbf{r}_2$ in which case

$$\sigma_I^2(\mathbf{r}) = 2 \text{Re} [E_2(\mathbf{r}, \mathbf{r}) + E_3(\mathbf{r}, \mathbf{r})]. \tag{3.93}$$

Substituting in the values for $E_2(\mathbf{r}, \mathbf{r})$ and $E_3(\mathbf{r}, \mathbf{r})$ plus making the substitution

$$\xi = 1 - \frac{\eta}{L} \text{ this becomes}$$

$$\begin{aligned}
\sigma_I^2(\mathbf{r}) &= 4\pi k^2 L \text{Re} \int_0^1 d\xi \int \int_{-\infty}^{\infty} d^2 \kappa \Phi_n(\mathbf{K}) \\
&\times \left\{ \exp \left[2\Lambda \xi \left(\mathbf{K} \cdot \mathbf{r} - \frac{\kappa^2 L}{2k} \xi \right) \right] - \exp \left[-\frac{i\kappa^2 L}{k} (1 - \bar{\theta} \xi) \xi \right] \exp \left[-\frac{\kappa^2 \Lambda L}{k} \xi^2 \right] \right\}
\end{aligned} \tag{3.94}$$

The scintillation index can be divided into a longitudinal or on-axis component plus a term that is radially dependent so that

$$\sigma_I^2(\mathbf{r}) = \sigma_{I,l}^2 + \sigma_{I,r}^2(\mathbf{r}) \quad (3.95)$$

With this definition

$$\sigma_{I,l}^2 = 4\pi k^2 L \int_0^1 d\xi \iint_{-\infty}^{\infty} d^2\kappa \Phi_n(\mathbf{K}) \exp\left(-\frac{\kappa^2 \Lambda L}{k} \xi^2\right) \left\{ 1 - \cos\left[\frac{\kappa^2 L}{k} (1 - \bar{\theta}_\xi) \xi\right] \right\} \quad (3.96)$$

and

$$\sigma_{I,r}^2(\mathbf{r}) = 4\pi k^2 L \int_0^1 d\xi \iint_{-\infty}^{\infty} d^2\kappa \Phi_n(\mathbf{K}) \exp\left(-\frac{\kappa^2 \Lambda L}{k} \xi^2\right) [\exp(2\Lambda \xi \mathbf{K} \cdot \mathbf{r}) - 1] \quad (3.97)$$

Note that $\sigma_{I,r}^2(\mathbf{r}) = 4\sigma_r^2(\mathbf{r})$.

At this point, we have derived the integral equations that describe the effect of optical turbulence on beam statistics. Namely, we have derived the integral equations for mean intensity, covariance of intensity, and scintillation index of a Gaussian beam. In Chapters 4-7, we will apply these equations with nonclassical power spectrums and compare theoretical predictions to experimental results.

CHAPTER 4: LONG-TERM SPOT SIZE, NORMALIZED INTENSITY AND SCINTILLATION INDEX IN NONCLASSICAL OPTICAL TURBULENCE

The work represented in this section was published in [15]. The theoretical analyses described in the publication were developed by the first author, Melissa Beason, with advice and guidance of coauthors

As stated previously, most of the work to date has assumed homogenous, isotropic optical turbulence which follows the classical Kolmogorov $\kappa^{-11/3}$ power law as in Equation (2.17). This work extends theory into slight deviations in power law from $\kappa^{-11/3}$ and considers the possibility of anisotropic turbulence. We will, however, assume homogeneity throughout this work.

In this chapter, we will compare two different methods to compute beam diameter based on methods used in classical turbulence and develop a model for mean intensity and scintillation index of a Gaussian beam in nonclassical turbulence. This model will provide the basis of our understanding of the effect of nonclassical turbulence on mean intensity and scintillation index which will be used to evaluate experimental results in Chapters 6 and 7.

The index of refraction power spectral density in generalized turbulence can be represented as [16]

$$\Phi_n(\kappa_x, \kappa_y, \kappa_z) = \frac{A(\alpha) \tilde{C}_n^2 \mu_x \mu_y}{(\mu_x^2 \kappa_x^2 + \mu_y^2 \kappa_y^2 + \kappa_z^2)^{\alpha/2}} \quad (4.1)$$

$$A(\alpha) = \frac{1}{4\pi^2} \Gamma(\alpha - 1) \cos\left(\frac{\alpha\pi}{2}\right), \quad 3 < \alpha < 4$$

In this representation, μ_x and μ_y indicate the strength of turbulence in orthogonal directions where smaller values correspond to a greater strength of turbulence. It is often the anisotropy ratio μ_y/μ_x that is of particular interest because it indicates the relative strength of turbulence in orthogonal directions. α is the power law relating the transfer of energy between scale sizes within the inertial range and \tilde{C}_n^2 is the generalized index of refraction structure constant which indicates strength of turbulence relative to the generalized anisotropy parameters μ_x, μ_y and power law α . $A(\alpha)$ is a multiplicative constant which reduces to 0.033 when $\alpha = 11/3$. With the assumption that turbulence is uncorrelated in the direction of propagation, $\kappa_z = 0$.

The above representation of the index of refraction power spectrum assumes that all scale sizes from infinitesimally small to infinitely large exist. For short propagation distances, this simplified power spectrum is sufficient. However, for longer distances and/or stronger turbulence, it is important to consider that the inertial range is finite with an inner scale size determined by dissipation and outer scale limited by environmental and meteorological considerations. In this case, a more generalized power spectrum should be used. This will be discussed further later in this text.

Equations (3.85) and (3.84) are relevant to this analysis and will be repeated here for clarity and continuity of thought.

$$\begin{aligned}\langle I(\mathbf{r}) \rangle &= \exp\left(-\frac{2r^2}{W^2}\right) \exp[2\sigma_r^2(\mathbf{r})] \\ \sigma_r^2(\mathbf{r}) &= k^2 L \int_0^1 d\xi \iint_{-\infty}^{\infty} d^2\kappa \Phi_n(\mathbf{K}) \exp\left(-\frac{\kappa^2 \Lambda L}{k} \xi^2\right) [\exp(2\Lambda \xi \mathbf{K} \cdot \mathbf{r}) - 1]\end{aligned}\quad (4.2)$$

It is mathematically simpler to transform the anisotropic power spectral density, $\Phi_n(\mathbf{K}) = \Phi_n(\kappa_x, \kappa_y, 0)$, to an isotropic form through use of the transformation

$$\kappa_x = \frac{q_x}{\mu_x} = \frac{q \cos \varphi}{\mu_x}, \quad \kappa_y = \frac{q_y}{\mu_y} = \frac{q \sin \varphi}{\mu_y}, \quad (4.3)$$

where the spatial frequency variable has been transformed first to a scaled spatial variable and then to polar coordinates. In this transformation

$$d^2\kappa = \frac{q dq d\varphi}{\mu_x \mu_y}, \quad \mathbf{K} \cdot \mathbf{r} = \kappa_x x + \kappa_y y = \frac{q \cos \varphi}{\mu_x} x + \frac{q \sin \varphi}{\mu_y} y \quad (4.4)$$

Recognizing that the vector $\mathbf{r} = (x, y)$, we can write Equations (4.1) - (4.2) as

$$\Phi_n(q) = \frac{A(\alpha) \tilde{C}_n^2 \mu_x \mu_y}{q^\alpha} \quad (4.5)$$

and

$$(4.6)$$

$$\sigma_r^2(x, y) = \frac{\pi k^2 L}{\mu_x \mu_y} \int_0^1 \int_0^{2\pi} \int_0^\infty q \Phi_n(q) \exp \left[-\frac{q^2 \Lambda L}{k} \xi^2 \left(\frac{\cos^2 \varphi}{\mu_x^2} + \frac{\sin^2 \varphi}{\mu_y^2} \right) \right] \times \left\{ \exp \left[2\Lambda \xi q \left(\frac{x \cos \varphi}{\mu_x} + \frac{y \sin \varphi}{\mu_y} \right) \right] - 1 \right\} dq d\varphi d\xi \quad (4.7)$$

The small argument approximation for the quantity in braces gives

$$\exp \left[2\Lambda \xi q \left(\frac{x \cos \varphi}{\mu_x} + \frac{y \sin \varphi}{\mu_y} \right) \right] - 1 \cong 2\Lambda \xi q \left(\frac{x \cos \varphi}{\mu_x} + \frac{y \sin \varphi}{\mu_y} \right) + 2(\Lambda \xi q)^2 \left(\frac{x \cos \varphi}{\mu_x} + \frac{y \sin \varphi}{\mu_y} \right)^2 \quad (4.8)$$

the first term of which yields a zero contribution with polar integration and thus

will be dropped from the derivation. In which case, $\sigma_r^2(x, y)$ becomes

$$\sigma_r^2(x, y) = 2\pi k^2 L A(\alpha) \tilde{C}_n^2 \Lambda^2 \int_0^1 \xi^2 \int_0^{2\pi} \left(\frac{x \cos \varphi}{\mu_x} + \frac{y \sin \varphi}{\mu_y} \right)^2 \int_0^\infty q^{3-\alpha} \times \exp \left[-\frac{\Lambda L q^2 \xi^2}{k} \left(\frac{\cos^2 \varphi}{\mu_x^2} + \frac{\sin^2 \varphi}{\mu_y^2} \right) \right] dq d\varphi d\xi \quad (4.9)$$

Evaluating the inner-most integral and rearranging the order of integration, this

becomes

$$\sigma_r^2(x, y) = \pi A(\alpha) \tilde{C}_n^2 \Gamma \left(2 - \frac{\alpha}{2} \right) k^{4-\frac{\alpha}{2}} L^{\frac{\alpha}{2}-1} \Lambda^{\frac{\alpha}{2}} \times \int_0^{2\pi} \left(\frac{x \cos \varphi}{\mu_x} + \frac{y \sin \varphi}{\mu_y} \right)^2 \left(\frac{\cos^2 \varphi}{\mu_x^2} + \frac{\sin^2 \varphi}{\mu_y^2} \right)^{\frac{\alpha}{2}-2} d\varphi \int_0^1 \xi^{\alpha-2} d\xi \quad (4.10)$$

which simplifies to

$$\sigma_r^2(x, y) = \frac{\pi A(\alpha)}{\alpha-1} \Gamma \left(2 - \frac{\alpha}{2} \right) \tilde{C}_n^2 k^{4-\frac{\alpha}{2}} L^{\frac{\alpha}{2}-1} \Lambda^{\frac{\alpha}{2}} \int_0^{2\pi} \left(\frac{x \cos \varphi}{\mu_x} + \frac{y \sin \varphi}{\mu_y} \right)^2 \left(\frac{\cos^2 \varphi}{\mu_x^2} + \frac{\sin^2 \varphi}{\mu_y^2} \right)^{\frac{\alpha}{2}-2} d\varphi \quad (4.11)$$

In these equations, $\Gamma(\bullet)$ refers to the gamma function.

4.1 Comparison of Two Common Methods to Calculate Spot Size

There are two methods often employed by scientists to approximate the beam diameter of a Gaussian beam after propagation through optical turbulence. Both of these methods were developed under the assumption of isotropy in which case the beam diameter calculations generate similar results. Here we extend both of these methods into nonclassical turbulence where we see a significant difference between the methods. When we extend into calculations of intensity contours, we see a possible explanation for this discrepancy.

4.1.1 Method 1

Under the assumption that the beam remains Gaussian with propagation but can become elliptical with major and minor axes that align with the x- and y-axes, we can solve for the beam width in each of these directions and construct Gaussian beam profiles accordingly.

In this analysis, it is convenient to recognize that $W^2 = 2L/k\Lambda$. In which case Equation (4.11) becomes

$$\begin{aligned} \sigma_r^2(x, y) = & \frac{2\pi A(\alpha)}{\alpha - 1} \Gamma\left(2 - \frac{\alpha}{2}\right) \tilde{C}_n^2 k^{3 - \frac{\alpha}{2}} L^{\frac{\alpha}{2}} \Lambda^{\frac{\alpha}{2} - 1} \left(\frac{1}{W^2}\right) \\ & \times \int_0^{2\pi} \left(\frac{x \cos \varphi}{\mu_x} + \frac{y \sin \varphi}{\mu_y}\right)^2 \left(\frac{\cos^2 \varphi}{\mu_x^2} + \frac{\sin^2 \varphi}{\mu_y^2}\right)^{\frac{\alpha}{2} - 2} d\varphi \end{aligned} \quad (4.12)$$

To determine the beam width in the x-direction, we set $y=0$ in Equations (4.2) and (4.11).

$$\langle I(x,0) \rangle = \exp\left(-\frac{2x^2}{W^2}\right) \exp[2\sigma_r^2(x,0)] \quad (4.13)$$

Employing a method similar to that found in [3], we can write the mean intensity along the x-axis as

$$\begin{aligned} \langle I(x,0) \rangle &= \exp\left[-\frac{2x^2}{W^2}(1-T_x)\right] \\ &\cong \exp\left[-\frac{2x^2}{W^2(1+T_x)}\right], \quad |T_x| \ll 1 \end{aligned} \quad (4.14)$$

where

$$T_x = \frac{2\pi A(\alpha)}{(\alpha-1)\mu_x^2} \Gamma\left(2-\frac{\alpha}{2}\right) \tilde{C}_n^2 k^{4-\frac{\alpha}{2}} L^{\frac{\alpha}{2}-1} \Lambda^{\frac{\alpha}{2}} \int_0^{2\pi} \cos^2 \varphi \left(\frac{\cos^2 \varphi}{\mu_x^2} + \frac{\sin^2 \varphi}{\mu_y^2}\right)^{\frac{\alpha}{2}-2} d\varphi \quad (4.15)$$

Following the same procedure, we find that the mean intensity along the y-axis becomes

$$\begin{aligned} \langle I(0,y) \rangle &= \exp\left[-\frac{2y^2}{W^2}(1-T_y)\right] \\ &\cong \exp\left[-\frac{2y^2}{W^2(1+T_y)}\right], \quad |T_y| \ll 1 \end{aligned} \quad (4.16)$$

where

$$T_y = \frac{2\pi A(\alpha)}{(\alpha-1)\mu_y^2} \Gamma\left(2-\frac{\alpha}{2}\right) \tilde{C}_n^2 k^{4-\frac{\alpha}{2}} L^{\frac{\alpha}{2}-1} \Lambda^{\frac{\alpha}{2}} \int_0^{2\pi} \sin^2 \varphi \left(\frac{\cos^2 \varphi}{\mu_x^2} + \frac{\sin^2 \varphi}{\mu_y^2}\right)^{\frac{\alpha}{2}-2} d\varphi \quad (4.17)$$

The long term spot radius, W_{LT} , includes the broadening caused by turbulence.

In the weak turbulence regime, we can approximate the beam diameter by examination of the denominator of Equations (4.14) and (4.16) in which case

$$W_{LTx1} = W(1+T_x)^{1/2}, \quad W_{LTy1} = W(1+T_y)^{1/2} \quad (4.18)$$

However, researchers have reported [16] that a slightly higher power will extend this fit well into deep turbulence (Rytov variance exceeding one), at least when the turbulence is isotropic. Using their work, we will express the long-term beam radius as

$$W_{LTx1} = W(1+T_x)^{3/5}, \quad W_{LTy1} = W(1+T_y)^{3/5} \quad (4.19)$$

The number in the subscript indicates the method employed.

4.1.2 Method 2

The second method that we will examine is based upon calculating the long-term beam radius using the plane-wave spatial-coherence radius [3], ρ_0 .

The spatial-coherence radius is defined as the distance where the degree of coherence has dropped to its 1/e value. For isotropic turbulence, the normalized intensity can be expressed as

$$\langle I(r) \rangle = \exp\left(-\frac{2r^2}{W_{LT}^2}\right) \quad (4.20)$$

where the long-term beam radius is given by

$$W_{LT} = W \left(1 + \frac{4}{3} q \Lambda \right), \quad q = \frac{L}{k \rho_0^2} \quad (4.21)$$

Andrews, et al [16] derived the spatial coherence radius in generalized turbulence to be

$$\tilde{\rho}_0 = \left[\frac{\alpha \Gamma(\alpha - 1) \Gamma\left(-\frac{\alpha}{2}\right)}{2^\alpha \Gamma\left(\frac{\alpha}{2}\right)} \cos\left(\frac{\alpha \pi}{2}\right) \right]^{\frac{1}{2-\alpha}} \left(\tilde{C}_n^2 k^2 L \right)^{\frac{1}{2-\alpha}} \quad (4.22)$$

Assuming an elliptical shape for the coherence radius with major and minor axes that are scaled by the anisotropy parameters,

$$\tilde{\rho}_0 = \sqrt{\left(\frac{\tilde{\rho}_{0x}}{\mu_x} \right)^2 + \left(\frac{\tilde{\rho}_{0y}}{\mu_y} \right)^2} \quad (4.23)$$

Here, $\tilde{\rho}_{0x}$ and $\tilde{\rho}_{0y}$ refer to the coherence radius in the x, y directions, respectively.

Following a similar procedure to that of Method 1, we will solve for the coherence radius in the orthogonal directions by setting its counterpart to zero. In so doing, we find

$$\tilde{\rho}_{0x} = \mu_x \left[-\frac{\pi \Gamma\left(1 - \frac{\alpha}{2}\right)}{2^{\alpha-3} \Gamma\left(\frac{\alpha}{2}\right)} A(\alpha) \tilde{C}_n^2 k^2 L \right]^{\frac{1}{2-\alpha}} \quad (4.24)$$

and

$$\tilde{\rho}_{0y} = \mu_y \left[-\frac{\pi \Gamma\left(1 - \frac{\alpha}{2}\right)}{2^{\alpha-3} \Gamma\left(\frac{\alpha}{2}\right)} A(\alpha) \tilde{C}_n^2 k^2 L \right]^{\frac{1}{2-\alpha}} \quad (4.25)$$

The long-term beam radius in the x and y directions is then given by

$$W_{LTx2} = \left(W^2 + \frac{8L^2}{3k^2 \tilde{\rho}_{0x}^2} \right)^{1/2}, \quad W_{LTy2} = \left(W^2 + \frac{8L^2}{3k^2 \tilde{\rho}_{0y}^2} \right)^{1/2} \quad (4.26)$$

4.1.3 Comparison of Methods

The $1/e^2$ beam diameter in the vertical direction was calculated as a function of power law (α) based on each of the two methods for a $1.06 \mu m$ laser beam propagating a distance of 5 km with $\tilde{C}_n^2 = 1 \times 10^{-14} m^{3-\alpha}$. Two different size transmit apertures were considered as well as three anisotropy ratios. The results are shown in Figures 4 and 5. For this scenario, the Rytov variance is $\sigma_R^2 = 5.9$ which corresponds to moderate to deep turbulence since $\sigma_R^2 > 1$. As one might expect, both methods produce similar results when the turbulence is nearly classical (anisotropy ratio near one and power law near 11/3) but they can differ significantly the further the deviation is from classical turbulence and the higher the strength of turbulence. For the vertical direction, strength of turbulence is higher as the anisotropy ratio decreases.

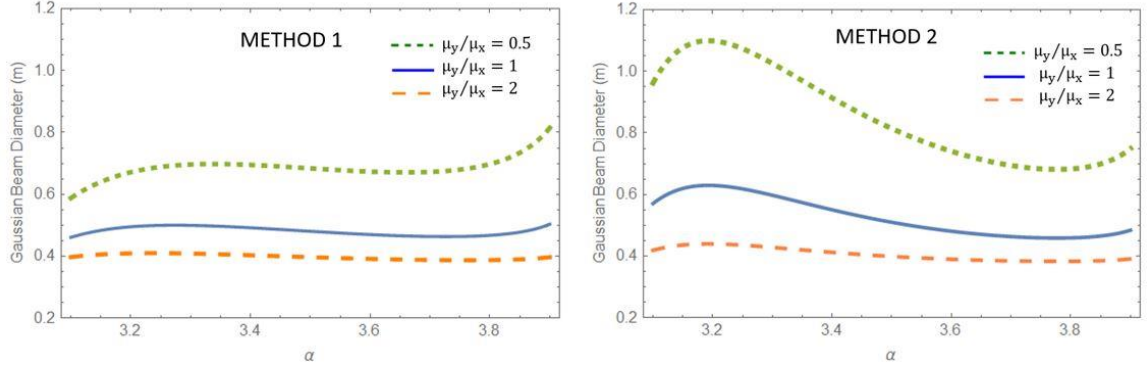


Figure 4. Comparison of two methods to compute beam diameter in the vertical (y) direction for three anisotropy ratios as a function of power law, α , for 50 cm transmit aperture with propagation distance of 5 km and $\tilde{C}_n^2 = 1 \times 10^{-14} m^{3-\alpha}$.

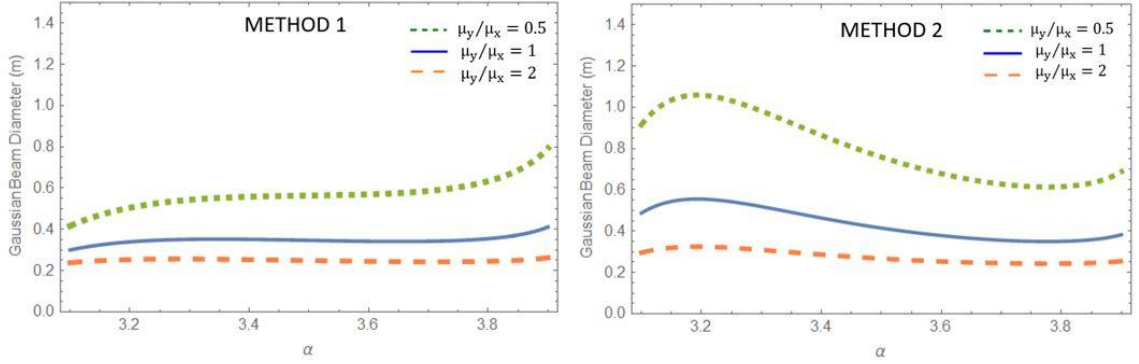


Figure 5. Comparison of two methods to compute beam diameter in the vertical (y) direction for three anisotropy ratios as a function of power law, α , for 5 cm transmit aperture with propagation distance of 5 km and $\tilde{C}_n^2 = 1 \times 10^{-14} m^{3-\alpha}$.

Assuming that the beam remains Gaussian with propagation, we can use the long-term beam diameters in the horizontal and vertical directions derived by Methods 1 and 2 to generate contours of equal intensity. In so doing, the assumed form for the intensity cross section is

$$\langle I(x, y) \rangle = \exp \left(-\frac{2x^2}{W_{LTx}^2} - \frac{2y^2}{W_{LTy}^2} \right) \quad (4.27)$$

Figures 6 and 7 show the resulting intensity contours for a 50 cm transmitter aperture, collimated, 1.06 μm beam after 5 km propagation with $\tilde{C}_n^2 = 1 \times 10^{-14} m^{3-\alpha}$. Equal intensity contours are shown for a combination of two different power laws and two different anisotropy parameters. These plots visually demonstrate that the predicted beam spot sizes for the two methods are most similar when α is near 11/3 and when $\mu_y / \mu_x > 1$ which corresponds to weaker turbulence.

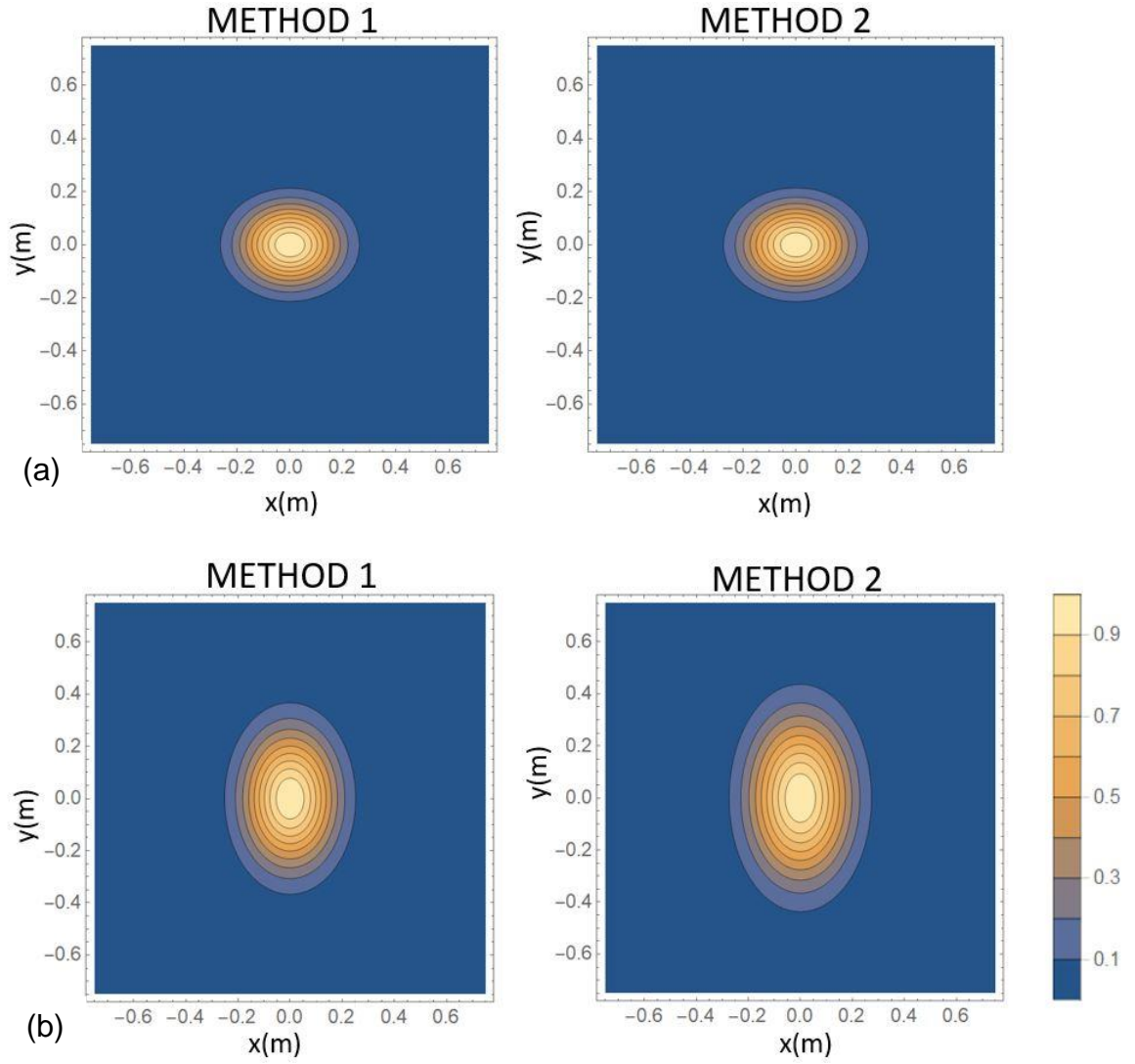


Figure 6. Comparison of beam contours for two methods with $\alpha = 3.5$, $L = 5$ km and $\tilde{C}_n^2 = 1 \times 10^{-14} m^{3-\alpha}$. (a) $\mu_y / \mu_x = 2$, (b) $\mu_y / \mu_x = 0.5$.

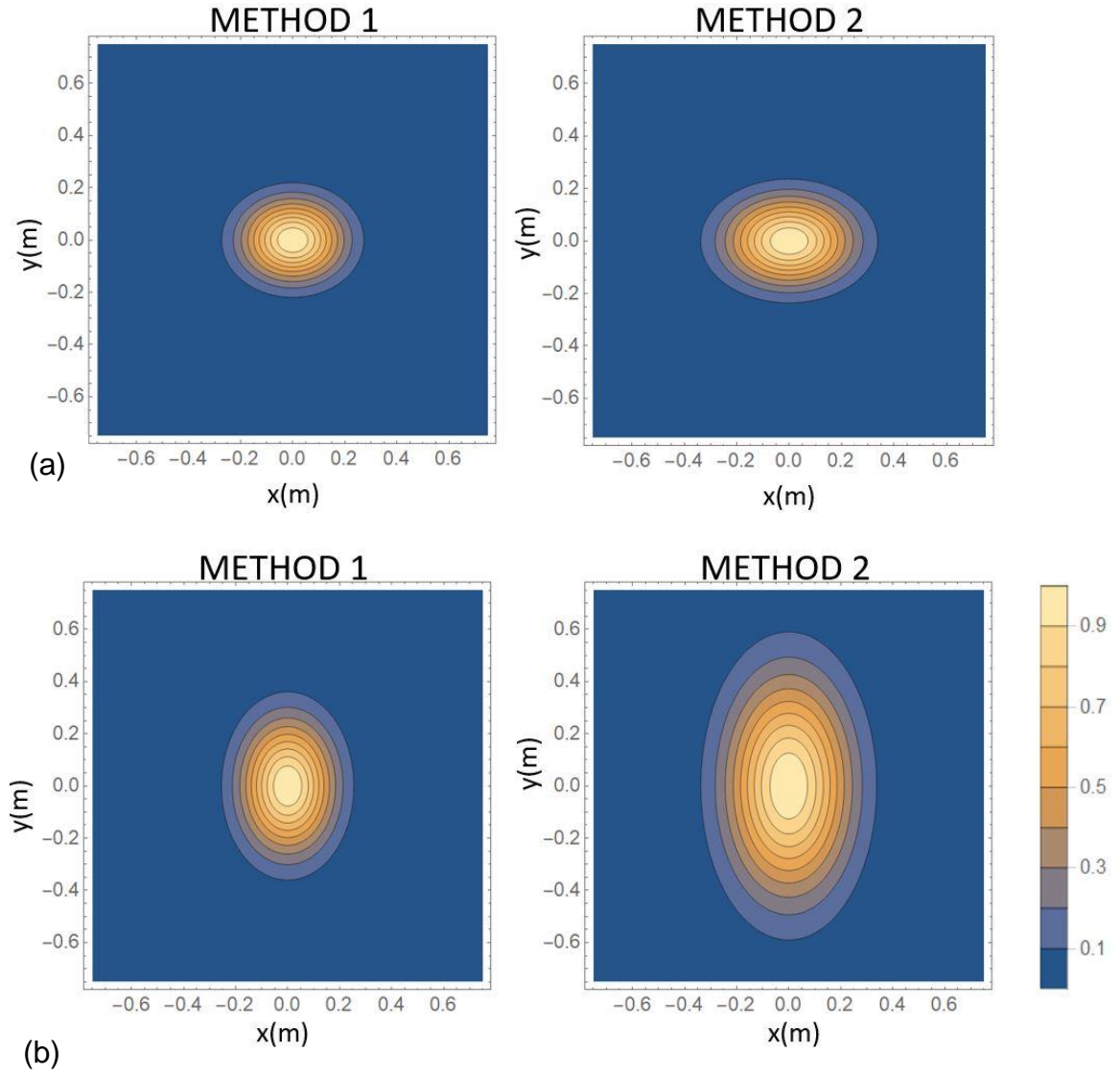


Figure 7. Comparison of beam contours for two methods with $\alpha = 3.2$, $L = 5$ km and $\tilde{C}_n^2 = 1 \times 10^{-14} m^{3-\alpha}$. (a) $\mu_y / \mu_x = 2$, (b) $\mu_y / \mu_x = 0.5$.

4.2 Normalized Intensity

Combining Equations (4.2) and (4.11) results in an equation for mean intensity valid in the weak irradiance-fluctuation regime;

$$\begin{aligned} \langle I(x, y) \rangle = & \exp \left[-\frac{2(x^2 + y^2)}{W^2} \right] \\ & \times \exp \left[\frac{2\pi A(\alpha) \Gamma(2 - \frac{\alpha}{2})}{(\alpha - 1)} \tilde{C}_n^2 k^{4 - \frac{\alpha}{2}} L^{\frac{\alpha}{2} - 1} \Lambda^{\frac{\alpha}{2}} \int_0^{2\pi} \left(\frac{x \cos \varphi}{\mu_x} + \frac{y \sin \varphi}{\mu_y} \right)^2 \left(\frac{\cos^2 \varphi}{\mu_x^2} + \frac{\sin^2 \varphi}{\mu_y^2} \right)^{\frac{\alpha}{2} - 1} d\varphi \right]. \end{aligned} \quad (4.28)$$

Figure 8 shows contours of equal mean intensity generated using Equation (4.28) for a 632.8 nm, 1 cm aperture, collimated Gaussian beam propagating in nonclassical turbulence with $\tilde{C}_n^2 = 1 \times 10^{-13}$, $\alpha = 3.5$ and anisotropy ratio $\mu_y / \mu_x = 0.33$ for increasing propagation distances. Figure 9 shows a radial cross section of this scenario along the positive y-axis. The center portion of the beam is plotted out to a distance equal to half the free-field radius. It is interesting to note that the initially circularly-symmetric beam becomes elliptical with propagation but seems to further distort and lose its Gaussian characteristic. This could explain the development of the discrepancy in beam size estimates in the previous section; when significant anisotropy is present, the Gaussian assumption for beam shape may no longer be adequate. As will be shown when we examine the scintillation index, the longer path lengths exceed the regime of

what is typically considered to be weak fluctuations, where the developed theory is strictly valid.

With further examination of Figures 8 and 9, one could conclude that beam shape is a poor measure for anisotropy. Anisotropic turbulence could be present and yet, depending on strength of turbulence, the path length may not be long enough for its effect to be evident on the beam shape. Furthermore, with propagation the beam becomes flatter and with measurement error and the imperfection of atmospheric statistics, changes across the beam may be harder to distinguish with significant propagation distance.

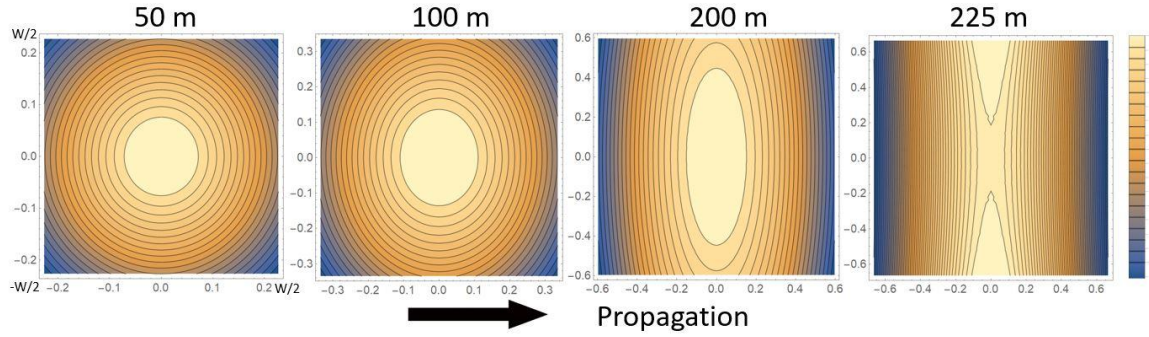


Figure 8. Equal mean-intensity contours resulting from propagation of 632.8 nm collimated beam with 1 cm transmitter diameter through nonclassical turbulence where $\alpha = 3.5$, $\mu_y / \mu_x = 0.33$ and $\tilde{C}_n^2 = 1 \times 10^{-13}$.

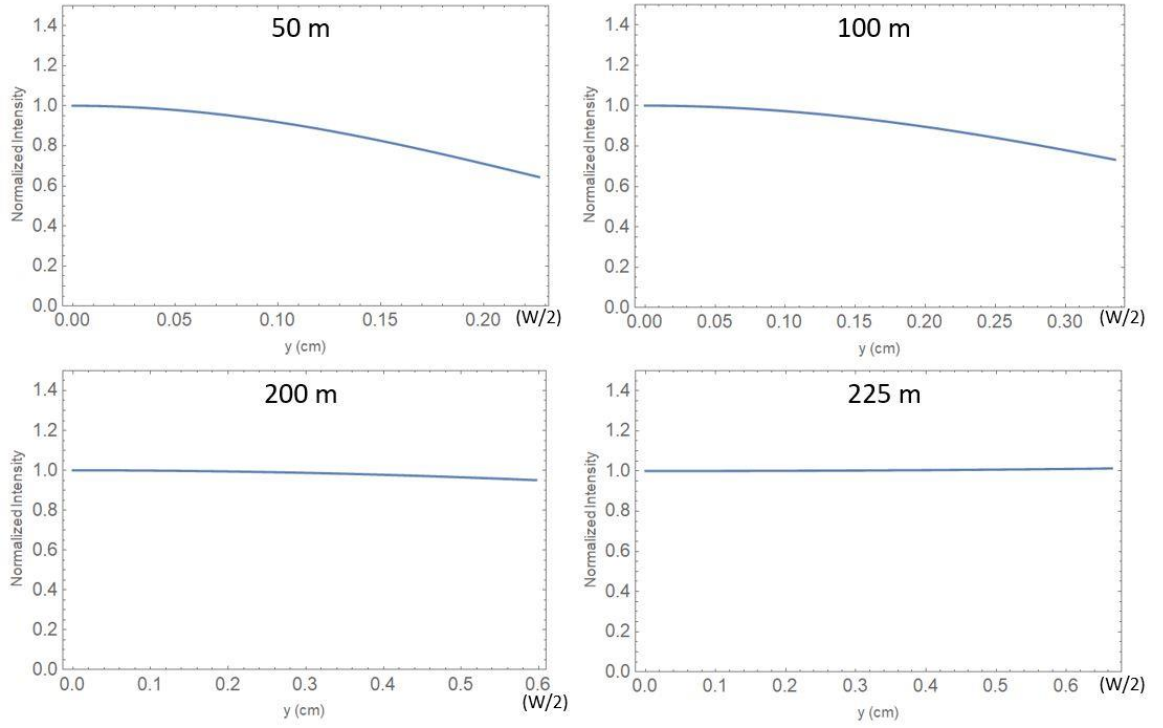


Figure 9. Mean intensity along vertical axis resulting from propagation of 632.8 nm collimated beam with 1 cm transmitter diameter through nonclassical turbulence where $\alpha = 3.5$, $\mu_y / \mu_x = 0.33$ and $\tilde{C}_n^2 = 1 \times 10^{-13}$.

4.3 Scintillation Index

The scintillation index was previously defined as the normalized variance of intensity given by Equations (3.95)-(3.97). For continuity, that definition for a Gaussian beam will be repeated here.

$$\begin{aligned}
 \sigma_I^2(\mathbf{r}) &= \sigma_{I,l}^2(\mathbf{r}) + \sigma_{I,r}^2(\mathbf{r}) \\
 \sigma_{I,l}^2(\mathbf{r}) &= 4\pi k^2 L \int_0^1 d\xi \int_{-\infty}^{\infty} d^2\kappa \Phi_n(\mathbf{K}) \exp\left(-\frac{\kappa^2 \Lambda L}{k} \xi^2\right) \left\{ 1 - \cos\left[\frac{\kappa^2 L}{k} (1 - \bar{\theta}\xi) \xi\right] \right\} \\
 \sigma_{I,r}^2(\mathbf{r}) &= 4\pi k^2 L \int_0^1 d\xi \int_{-\infty}^{\infty} d^2\kappa \Phi_n(\mathbf{K}) \exp\left(-\frac{\kappa^2 \Lambda L}{k} \xi^2\right) [\exp(2\Lambda \xi \mathbf{K} \cdot \mathbf{r}) - 1]
 \end{aligned} \tag{4.29}$$

In isotropic turbulence formulations, it is often convenient to express results in terms of the Rytov variance and the magnitude of this is often used to determine whether weak or strong fluctuation theory is most appropriate for use. Therefore, we find it expedient to define the generalized Rytov variance [16], $\tilde{\sigma}_R^2$, as the scintillation index of a plane wave propagating through generalized turbulence. For a plane wave, $\Lambda = 0$ and $\Theta = 1$ so $\bar{\Theta} = 0$. Note that the radial component of the scintillation index vanishes and the plane-wave scintillation index is given by

$$\sigma_R^2(\mathbf{r}) = 4\pi k^2 L \int_0^1 d\xi \int \int_{-\infty}^{\infty} d^2 \mathbf{K} \Phi_n(\mathbf{K}) \left[1 - \cos\left(\frac{\kappa^2 L \xi}{k}\right) \right] \quad (4.30)$$

To extend this definition to the generalized Rytov variance, we substitute the generalized spectrum defined by Equation (4.1) and perform the coordinate transformation prescribed by Equations (4.3) - (4.5).

$$\tilde{\sigma}_R^2 = 4\pi A(\alpha) \tilde{C}_n^2 k^2 L \int_0^{2\pi} \int_0^1 \int_0^\infty dq d\xi d\varphi q^{1-\alpha} \left\{ 1 - \cos\left[\frac{Lq^2 \xi}{k} \left(\frac{\cos^2 \varphi}{\mu_x^2} + \frac{\sin^2 \varphi}{\mu_y^2} \right) \right] \right\} \quad (4.31)$$

Which upon evaluation yields

$$\tilde{\sigma}_R^2 = -\frac{\Gamma(\alpha-1)}{\alpha\pi} \Gamma\left(1-\frac{\alpha}{2}\right) \sin\left(\frac{\alpha\pi}{4}\right) \cos\left(\frac{\alpha\pi}{2}\right) \tilde{C}_n^2 k^{3-\frac{\alpha}{2}} L^{\frac{\alpha}{2}} \int_0^{2\pi} \left(\frac{\cos^2 \varphi}{\mu_x^2} + \frac{\sin^2 \varphi}{\mu_y^2} \right)^{\frac{\alpha}{2}-1} d\varphi, \quad (4.32)$$

The power law is restricted to the interval $3 < \alpha < 4$.

To compute the scintillation index for a Gaussian beam wave in generalized turbulence, we return to Equations (4.29) and perform the coordinate

transformation as previously. This results in a longitudinal component to the scintillation index of

$$\sigma_{I,l}^2 = \frac{4\pi k^2 L}{\mu_x \mu_y} \int_0^{2\pi} \int_0^1 \int_0^\infty q \tilde{\Phi}_n(q) \exp \left[-\frac{q^2 \Lambda L}{k} \xi^2 \left(\frac{\cos^2 \varphi}{\mu_x^2} + \frac{\sin^2 \varphi}{\mu_y^2} \right) \right] \times \left\{ 1 - \cos \left[\frac{q^2 L}{k} \xi \left(1 - \bar{\Theta} \xi \right) \left(\frac{\cos^2 \varphi}{\mu_x^2} + \frac{\sin^2 \varphi}{\mu_y^2} \right) \right] \right\} dq d\xi d\varphi \quad (4.33)$$

With substitution of the generalized spectrum and writing the cosine as the real part of a complex exponential, evaluation of the resulting inner integral yields

$$\sigma_{I,l}^2 = \frac{\Gamma(\alpha-1)}{2\pi} \Gamma\left(1-\frac{\alpha}{2}\right) \cos\left(\frac{\alpha\pi}{2}\right) \tilde{C}_n^2 k^{3-\frac{\alpha}{2}} L^{\frac{\alpha}{2}} \times \int_0^{2\pi} \left(\frac{\cos^2 \varphi}{\mu_x^2} + \frac{\sin^2 \varphi}{\mu_y^2} \right)^{\frac{\alpha}{2}-1} \operatorname{Re} \int_0^1 \left\{ \xi^{\alpha-2} - \left[\Lambda \xi^2 + i\xi(1-\bar{\Theta}\xi) \right]^{\frac{\alpha}{2}-1} \right\} d\xi d\varphi \quad (4.34)$$

In this equation, $\operatorname{Re}[-]$ represents the real part and $i = \sqrt{-1}$. Evaluating the first half of the inner integral and rewriting the second half this becomes

$$\sigma_{I,l}^2 = \frac{\Gamma(\alpha-1)}{2\pi} \Gamma\left(1-\frac{\alpha}{2}\right) \cos\left(\frac{\alpha\pi}{2}\right) \tilde{C}_n^2 k^{3-\frac{\alpha}{2}} L^{\frac{\alpha}{2}} \times \int_0^{2\pi} \left(\frac{\cos^2 \varphi}{\mu_x^2} + \frac{\sin^2 \varphi}{\mu_y^2} \right)^{\frac{\alpha}{2}-1} \left\{ \frac{1}{\alpha-1} - i^{\frac{\alpha}{2}-1} \int_0^1 \frac{\xi^{\frac{\alpha}{2}-1}}{\left[1 - (\bar{\Theta} + i\Lambda)\xi \right]^{1-\frac{\alpha}{2}}} d\xi \right\} d\varphi \quad (4.35)$$

where

$$\int_0^1 \frac{\xi^{\frac{\alpha}{2}-1}}{\left[1 - (\bar{\Theta} + i\Lambda)\xi \right]^{1-\frac{\alpha}{2}}} d\xi = \frac{2}{\alpha} {}_2F_1\left(1-\frac{\alpha}{2}, \frac{\alpha}{2}; 1+\frac{\alpha}{2}; \bar{\Theta} + i\Lambda\right) \quad (4.36)$$

${}_2F_1(-,-;-)$ corresponds to the hypergeometric function defined by

$${}_2F_1(a,b;c;z) = \sum_{n=0}^{\infty} \frac{(a)_n (b)_n}{(c)_n} \frac{z^n}{n!} \quad (4.37)$$

Upon substitution of (4.36) the axial component of the scintillation index is given by

$$\begin{aligned} \sigma_{I,l}^2 = & -\frac{\Gamma(\alpha-1)}{\pi\alpha} \Gamma\left(1-\frac{\alpha}{2}\right) \cos\left(\frac{\alpha\pi}{2}\right) \tilde{C}_n^2 k^{3-\frac{\alpha}{2}} L^{\frac{\alpha}{2}} \int_0^{2\pi} \left(\frac{\cos^2 \varphi}{\mu_x^2} + \frac{\sin^2 \varphi}{\mu_y^2} \right)^{\frac{\alpha}{2}-1} d\varphi \\ & \times \operatorname{Re} \left[i^{\frac{\alpha}{2}-1} {}_2F_1\left(1-\frac{\alpha}{2}, \frac{\alpha}{2}; 1+\frac{\alpha}{2}; \bar{\Theta}+i\Lambda\right) - \frac{\alpha\Lambda^{\frac{\alpha}{2}-1}}{2(\alpha-1)} \right]. \end{aligned} \quad (4.38)$$

Use of the generalized Rytov variance simplifies this expression to

$$\sigma_{I,l}^2 = \frac{\tilde{\sigma}_R^2}{\sin\left(\frac{\alpha\pi}{4}\right)} \operatorname{Re} \left[i^{\frac{\alpha}{2}-1} {}_2F_1\left(1-\frac{\alpha}{2}, \frac{\alpha}{2}; 1+\frac{\alpha}{2}; \bar{\Theta}+i\Lambda\right) - \frac{\alpha\Lambda^{\frac{\alpha}{2}-1}}{2(\alpha-1)} \right]. \quad (4.39)$$

We can quickly derive the off-axis contribution to the scintillation index by taking advantage of the relationship $\sigma_{I,r}^2(\mathbf{r}) = 4\sigma_r^2(\mathbf{r})$. Using Equation (4.11) we find

$$\sigma_r^2(x,y) = \frac{4\pi A(\alpha)}{\alpha-1} \Gamma\left(2-\frac{\alpha}{2}\right) \tilde{C}_n^2 k^{4-\frac{\alpha}{2}} L^{\frac{\alpha}{2}-1} \Lambda^{\frac{\alpha}{2}} \int_0^{2\pi} \left(\frac{x \cos \varphi}{\mu_x} + \frac{y \sin \varphi}{\mu_y} \right)^2 \left(\frac{\cos^2 \varphi}{\mu_x^2} + \frac{\sin^2 \varphi}{\mu_y^2} \right)^{\frac{\alpha}{2}-2} d\varphi \quad (4.40)$$

As an example of the behavior of the scintillation index with nonclassical turbulence, we repeat the examples shown in Figures 8-9. Namely, we look at the scintillation index that results from propagation of a 632.8 nm, 1 cm aperture, collimated Gaussian beam with $\tilde{C}_n^2 = 1 \times 10^{-13}$, $\alpha = 3.5$ and anisotropy ratio

$\mu_y / \mu_x = 0.33$. Figure 10 shows contours of equal scintillation index resulting from 100 m propagation. Only this propagation distance is shown because contours from other distances appear identical with the only difference being the magnitude of scintillation index. Figure 11 shows the radial increase of the scintillation index along the vertical axis (strong turbulence direction).

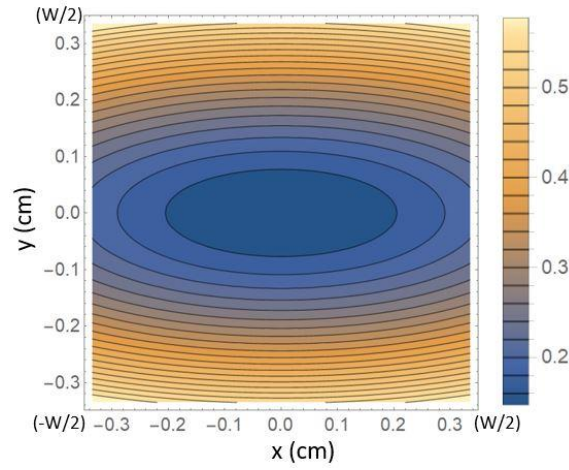


Figure 10. Contours of equal scintillation index resulting from 100 m propagation of 632.8 nm collimated beam with 1 cm transmitter diameter through nonclassical turbulence where $\alpha = 3.5$, $\mu_y / \mu_x = 0.33$ and $\tilde{C}_n^2 = 1 \times 10^{-13}$.

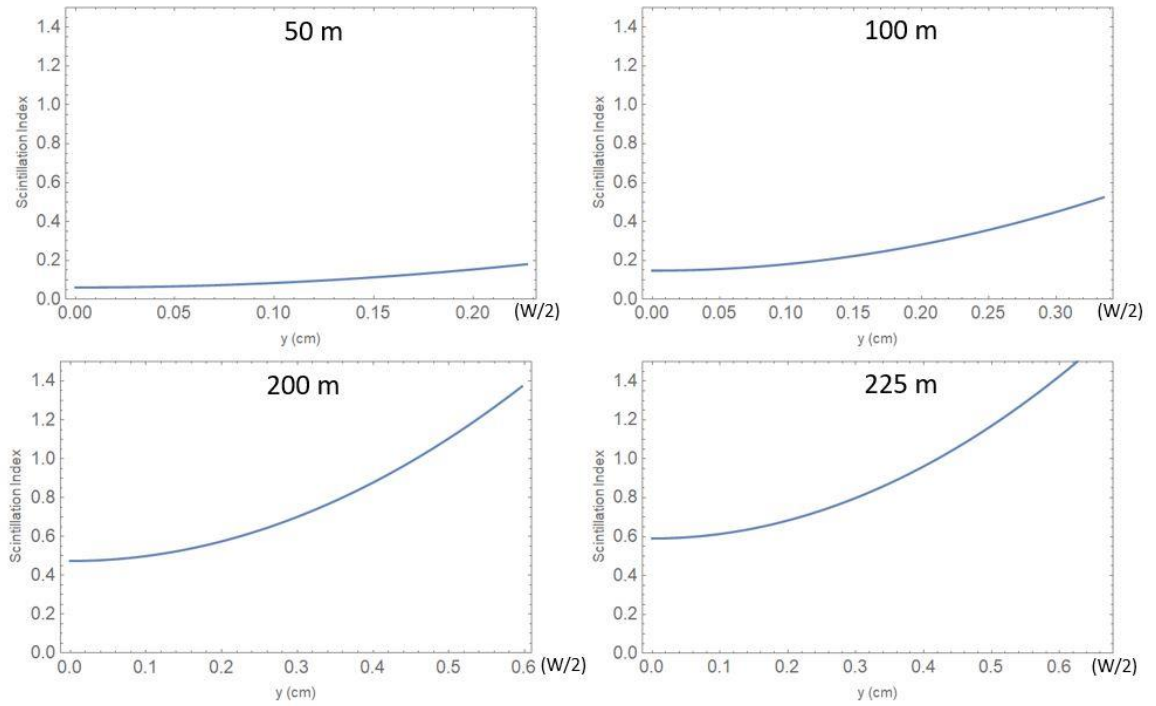


Figure 11. Scintillation index along vertical axis resulting from propagation of 632.8 nm collimated beam with 1 cm transmitter diameter through nonclassical turbulence where $\alpha = 3.5$, $\mu_y / \mu_x = 0.33$ and $\tilde{C}_n^2 = 1 \times 10^{-13}$. Propagation distance is shown on figure.

It is of interest to note that contour plots of equal scintillation index form ellipses which indicate the presence of anisotropy even with short propagation paths. The scintillation index is minimum at the center of the beam increasing with distance from the center. For this theory to be strictly valid, σ_I^2 should not exceed one. As can be seen with examination of Figure 11, the scintillation index for the outer edges of the beam with the longest propagation paths does exceed one and thus results from that portion of the beam may not be as accurately modeled. This also implies that we have exceeded what is strictly valid when

making conclusions about intensity for these distances. However, since we are not much in excess of one, the results probably show valid trends. For experimentation, we chose to limit the path length so that the developed theory would be strictly valid.

Another interesting observation about the scintillation index is that the resulting contours are a good indication of the magnitude of the anisotropy ratio. The author found that for all cases considered, the ratio of the axes in the scintillation index contours was about 10% different than the actual anisotropy ratio. Since the scintillation index always indicates the presence of anisotropy and since its ellipses are good indicators for the anisotropy ratio, the scintillation index of a Gaussian beam is an excellent tool to determine if the atmospheric statistics are anisotropic.

CHAPTER 5: COVARIANCE OF INTENSITY, THEORY AND MEASUREMENT IN NONCLASSICAL TURBULENCE

The work described in this chapter was published in Optics Letters 1 June 2018 [17]. Theoretical development and experimental analysis was done by Melissa Beason using data collected by coauthors. One of the coauthors, Christopher Smith, developed the code used to process frames of camera data and calculate relevant statistics.

During the week of January 30 – February 3, 2017, the UCF Wave Propagation Research Group participated in a program designed to measure atmospheric conditions near the ground at multiple times throughout the year at the Shuttle Landing Facility (SLF), Kennedy Space Center, Florida (Figure 12). The SLF is a concrete runway measuring 91 m x 4572 m with an approximately 100 m grass strip running along each side. It's sheer size leads to near homogenous conditions which makes it ideal for characterizing turbulence. As part of the activity during this week, the group was requested to provide video data of a beam propagated along the SLF for comparison to simulations. This was not part of the activity studying the presence and effect of nonclassical turbulence characteristics. However, when we calculated the Covariance of Intensity (CFI) corresponding to this data, we realized that it indicated the presence of anisotropic conditions at times and so we chose to add this data and analysis of CFI to this study.



Figure 12. Aerial view of SLF runway, Kennedy Space Center, Florida. Reprinted with permission from [17], Optical Society of America.

For this experiment, a 532 nm wavelength, 10 cm diameter Gaussian beam was propagated 1 or 2 km near the center and along the length of the runway at a height of 2 m above the ground. Because of the short wavelength and relatively large initial beam size, this beam has a nearly planar wave front which allows us to use the much simpler plane-wave theory. The flatness of the phase front is determined by the Fresnel ratio which corresponds to diffractive changes along the beam path. This is defined by [3]

$$\Lambda_0 = \frac{2L}{kW_0^2} \quad (5.1)$$

where L is the path length, $k = 2\pi/\lambda$ is the optical wavenumber, and W_0 is the initial $1/e^2$ intensity radius. For a perfect plane wave $\Lambda_0 = 0$. For the 1 and 2 km path lengths Λ_0 has values of 0.07 and 0.14, respectively. Since the Fresnel ratio is so near 0, the plane wave theoretical development is appropriate.

The theoretical development in this work is based on the assumption of weak-irradiance fluctuations while the Rytov variance for all cases studied exceeds one. This is a potential source of error; however, as can be seen in the following sections, this theory matches the data well.

5.1 Plane Wave CFI Theory

Using Equation (3.91), we find that the CFI is given by

$$B_I(\mathbf{r}_1 - \mathbf{r}_2) = 4\pi k^2 L \text{Re} \int_0^1 \int_{-\infty}^{\infty} \int_{-\infty}^{\infty} \Phi_n(\boldsymbol{\kappa}) \exp(i\boldsymbol{\kappa} \cdot \mathbf{p}) \left[1 - \cos\left(\frac{\kappa^2 L \xi}{k}\right) \right] d^2 \kappa d\xi \quad (5.2)$$

where $\boldsymbol{\kappa} = (\kappa_x, \kappa_y, 0)$ is the spectral spatial wave-number vector and $\mathbf{p} = \mathbf{r}_1 - \mathbf{r}_2$ is the vector separation between points \mathbf{r}_1 and \mathbf{r}_2 .

For this analysis, we used a generalized power spectrum model which incorporates both inner and outer scales of turbulence. In this model, all scale sizes are considered to be anisotropic. Inner scale is modeled through the terms κ_{mx} and κ_{my} and outer scale through the terms κ_{0x} and κ_{0y} .

$$\Phi_n(\boldsymbol{\kappa}) = A(\alpha) \tilde{C}_n^2 \frac{\mu_x \mu_y \exp(-\kappa_x^2 / \kappa_{mx}^2) \exp(-\kappa_y^2 / \kappa_{my}^2)}{\left(\mu_x^2 \kappa_x^2 + \mu_y^2 \kappa_y^2 + \mu_x^2 \kappa_{ox}^2 + \mu_y^2 \kappa_{oy}^2 \right)^{\alpha/2}} \quad (5.3)$$

$$A(\alpha) = \frac{\Gamma(\alpha - 1) \cos\left(\frac{\alpha\pi}{2}\right)}{4\pi^2} \quad (5.4)$$

Recall that for classical isotropic turbulence $\mu_x = \mu_y = 1$ and $\alpha = 11/3$ in which case $A(\alpha) = 0.033$. Anisotropy is found when the ratio $\mu_y / \mu_x \neq 1$. While this

spectral model offers the opportunity to vary α , in this work we assumed the classical value of 11/3 and limited our study to evidence of anisotropy.

Following the same procedure that we did in Chapter 4, we transform the spectrum and covariance to first a stretched then cylindrical coordinate system from which we can numerically evaluate the results. The aforementioned transformations are

$$\kappa_x = \frac{q_x}{\mu_x} = \frac{q \cos \theta}{\mu_x}, \quad \kappa_y = \frac{q_y}{\mu_y} = \frac{q \sin \theta}{\mu_y} \quad (5.5)$$

and

$$q = \sqrt{q_x^2 + q_y^2}, \quad d^2 \kappa = \frac{d^2 q}{\mu_x \mu_y} \quad (5.6)$$

With these transformations, the CFI becomes

$$B_I(\rho) = \frac{4\pi k^2 L}{\mu_x \mu_y} \text{Re} \int_0^1 \int_0^\infty \int_0^{2\pi} q \Phi_n(q) \exp(iq\rho) \left[1 - \cos\left(\frac{q^2 L t \xi}{k}\right) \right] d\theta dq d\xi \quad (5.7)$$

where

$$\rho = \frac{\rho_x}{\mu_x} \cos \theta + \frac{\rho_y}{\mu_y} \sin \theta, \quad t = \frac{\cos^2 \theta}{\mu_x^2} + \frac{\sin^2 \theta}{\mu_y^2}. \quad (5.8)$$

Since we are concerned with the shape of the CFI rather than its magnitude, we normalize it by dividing by its peak value, $B_I(0)$, or scintillation index.

$$b_I(\rho) = B_I(\rho)/B_I(0) \quad (5.9)$$

In the stretched coordinate system, the power spectrum takes on a simpler isotropic form

$$\Phi_n(q) = A(\alpha) \tilde{C}_n^2 \frac{\mu_x \mu_y \exp\left(-\frac{q^2}{q_m^2}\right)}{(q^2 + q_o^2)^{\alpha/2}}. \quad (5.10)$$

The inner and outer scale parameters are given by (see Appendix 1).

$$q_o = \frac{2\pi}{L_o}, \quad q_m = \frac{\left(\frac{\Gamma(\alpha-1) \cos\left(\frac{\alpha\pi}{2}\right) \Gamma\left(\frac{5-\alpha}{2}\right)}{6\pi} \right)^{\frac{1}{\alpha-5}}}{l_o} \quad (5.11)$$

l_o and L_o correspond to the inner and outer scales of turbulence, respectively.

When $\alpha = 11/3$, $q_m = 5.92/l_o$, the spectrum is recognizable as the modified von Karman spectrum model from classical turbulence theory.

The triple integral from (5.7) - (5.11) was numerically evaluated using *Mathematica*. The results were rotated to correspond to experimental images.

5.2 CFI Experimental Setup and Processing

The experimental configuration (Figure 13) consisted of a 532 nm laser which was collimated and expanded to 10 cm diameter and propagated for 1 or 2 km at a height of 2 m above the runway. The laser was the source for both experiments at 532 nm described in this report. It is a frequency doubled Nd:YAG manufactured by OEM Laser Systems (model number VIA-532-00800-05) with 800 mW power. Neutral density filters were placed in front of the source to

prevent saturation of the camera. The beam was collimated visually by adjusting the separation of the collimating optics to minimize beam expansion at the receiver. The fluctuating intensity was collected at the receiver and focused down onto the charge-coupled device (CCD) array of a Prosilica GC660 camera which has 659 (horizontal) x 453 (vertical) pixels of physical diameter $5.6 \mu\text{m}$ on each side. The CCD array was placed short of the focus of the receiver lens in such a way that the full lens was visible on the CCD (see Figure 14 for typical CCD image). Each pixel corresponded to a square area of approximately 0.29 mm on each side depending on the lens adjustment. The irradiance fluctuations were recorded in 1 minute increments at a rate of 60 frames per second. Frame statistics were calculated in post processing including mean, scintillation index, correlation, and covariance of intensity. The correlation and covariance were calculated relative to the centroid where the centroid was determined by calculating the mean of all pixel locations that exceeded a certain threshold. Since the beam is nearly planar, the results should be the same regardless of center. During this week of testing, data was taken with this system four times on each of the two measurement days with data collection cycles distributed throughout the day.

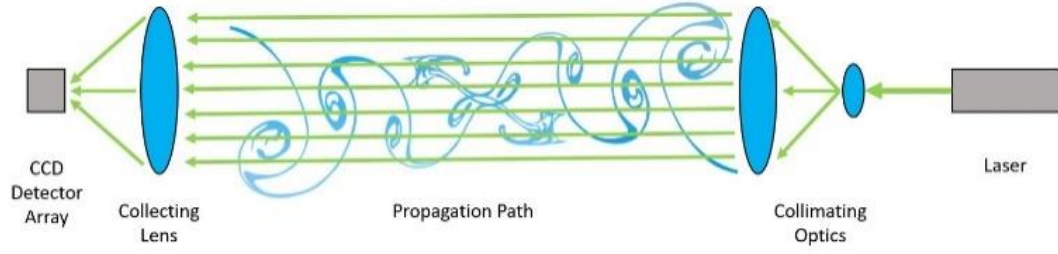


Figure 13. Experimental configuration. The transmitter consisted of a 532 nm collimated laser with a 10 cm Gaussian spatial profile. A GC660 camera was placed before the focus of the 12 cm receiver lens. Reprinted with permission from [17], Optical Society of America.

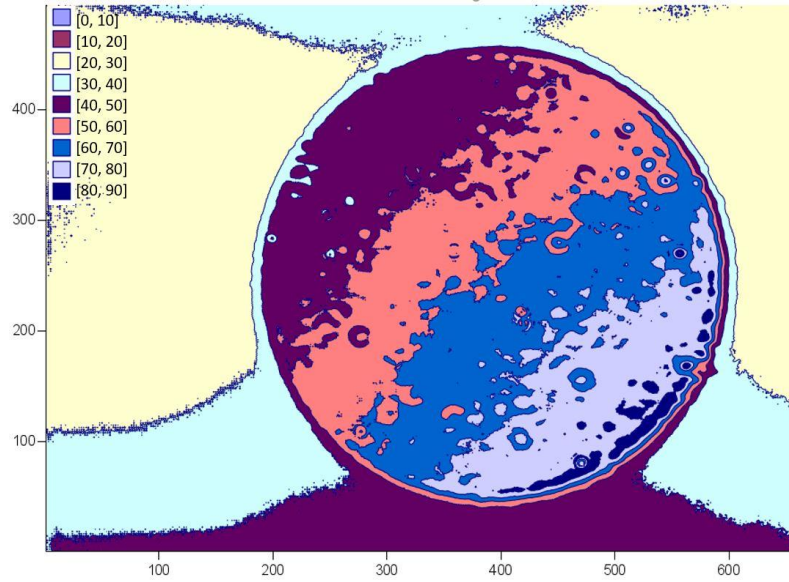


Figure 14. Typical CCD image. Note how the entire circular lens is visible on the CCD.

The CFI of two points r_1 and r_2 on the beam is defined as [3]

$$B_I(r_1, r_2) = \frac{\langle I(r_1)I(r_2) \rangle}{\langle I(r_1) \rangle \langle I(r_2) \rangle} - 1 \quad (5.12)$$

Note that when $r_1 = r_2$, this reduces to the scintillation index.

Expressing this discretely in terms of the centroid, ρ_c , and a point on the CCD array, ρ_{xy} ,

$$B_I(\rho_{xy}) = \frac{\frac{1}{N} \sum_{n=1}^N I^{(n)}(\rho_c) I^{(n)}(\rho_{xy})}{\bar{I}(\rho_c) \bar{I}(\rho_{xy})} - 1 \quad (5.13)$$

where

$$\bar{I}(\rho) = \frac{1}{N} \sum_{n=1}^N I^{(n)}(\rho) \quad (5.14)$$

Furthermore, with normalization by the scintillation index at the centroid this becomes

$$b_I(\rho) = B_I(\rho_c, \rho) / B_I(\rho_c, \rho_c). \quad (5.15)$$

5.3 Comparison of Theory to Experimental Results

The SLF was instrumented with multiple atmospheric devices including a pyrometer, hygrometer, two sonic anemometers as well as air and ground temperature probes. Anemometer (1) was located near the transmitter. During the January 31 experiment, anemometer (2) was located mid-path while it was moved near the receiver for the February 2 experiment. The data collected from these instruments for the times relevant to this work are shown in Table 1. The complete data collected throughout the day is shown in Chapter 6. The Rytov variance for the particular propagation conditions is shown in this table.

Intensity fluctuation data were collected on 31 January 2017 corresponding to a path length of 1 km and on 2 February 2017 corresponding to a path length of 2 km. The normalized CFI was calculated from the data and compared to numerical integration results from Equations (5.7) - (5.11). Because of the method used to achieve collimation, the beam was slightly divergent or convergent. To account for this when comparing experimental data to theoretical predictions, a spatial scaling factor equivalent to a geometrical optics focus or defocus was incorporated. This scaling factor varied between a 0.45 (slight focus) to 1.9 (slight defocus). A small correlated background signal of between 10 – 15% of the peak correlation was subtracted from the experimental CFI prior to comparison with theory. A spectral power law of $\alpha = 11/3$ was assumed in the theoretical calculations. Also, only the center portion of the CCD is shown to emphasize regions with nonzero CFI. Inner and outer scales of 5 mm and 1 m, respectively, were assumed in this analysis which correspond to typical near ground conditions, however, power law as well as inner and outer scale sizes had little impact on the CFI curves.

While more data was available than was used to compare with theory, the author chose to study three contrasting cases. All of the data from the two days of testing is shown in Chapter 6. Equal normalized CFI as well as major and minor axis cross sections are shown in Figures 15 - 17. The anisotropy ratio μ_y/μ_x was chosen for best fit to data and the theoretical CFI contours were rotated to match data.

Experimental and theoretical curves matched well for cases that were nearly isotropic ($\mu_y / \mu_x \cong 1$). As the anisotropy ratio increased, the comparison of the axis with less strength of turbulence (major axis) continued to fit well. The stronger turbulence axis (minor axis) fit well near the centroid of the CFI but experimental data had “shoulders” which were not present in theoretical results. This could have resulted from measurement methods, the slight Gaussian characteristic of the beam, or that the experiment extended beyond the weak fluctuation regime of the theory. Ideally, the experimental setup would have imaged the pupil plane rather than recording irradiance data from a region between the pupil and focal planes as in this experimental arrangement. This could explain the difference between experiment and theory under anisotropic conditions, however, we believe a more likely explanation is that theory is based on weak irradiance fluctuations, while experimental data exceeded this regime.

Other researchers reported a significant tilt angle in measured CFI from 210 m propagation of a spherical wave [6, 18]. The SLF data, however, demonstrated little or no tilt.

During this experiment, the SLF data show a wide range of anisotropy ratio as well as a rotation of the direction of stronger turbulence. During times that the data appear to indicate anisotropy, the solar flux was low and the strength of turbulence also tended to be low. The data in Figure 15 showed statistical isotropy during the highest solar flux and when the strength of turbulence was mid-range for the data collected.

It has previously been reported that the CFI of a spherical wave [6] and the scintillation index of a beam wave [15] have equal contours which are elliptical where the axes ratio of the ellipse have nearly the same value as the anisotropy ratio used to generate it. Ellipses of equal CFI contours do not display the same relationship to anisotropy ratio. The contour ellipses near the centroid are nearly the same as the CFI, however, unlike the other mentioned cases, the ellipse ratio increases with distance from the centroid.

The CFI from the measured data corresponds to what we would theoretically expect for propagation through anisotropic turbulence. In the next chapter, we will examine the characteristics of contours of equal CFI from this data set as well as contours of equal scintillation index from another test set. With the understanding of the behavior of the CFI from propagation in anisotropic turbulence from this chapter and the behavior of the scintillation index of a Gaussian beam from Chapter 4, we will be equipped to study how turbulence evolves between isotropy and anisotropy throughout the course of multiple days.

Table 1. Time, Atmospheric Conditions, and Rytov Variance Corresponding to Measurement Times. Anemometer (1) was located near the transmitter and anemometer (2) was located mid-path on 31 January and near the receiver on 2 February. The wind direction is relative to the propagation direction where 0° is wind blowing in the direction of propagation. σ_R^2 is the Rytov variance. Reprinted with permission from [17], Optical Society of America.

Fig #	Date and Time	C_n^2 ($\text{m}^{-2/3}$)	σ_R^2	Relative Humidity (%)	Solar Flux (W/m^2)	Ground Temp ($^{\circ}\text{C}$)	Air Temp ($^{\circ}\text{C}$)	(1) Wind Speed (m/s)	(1) Wind Direction (Deg)	(2) Wind Speed (m/s)	(2) Wind Direction (Deg)
15	31 Jan 17 9:12 am	1.9×10^{-14}	1.3	75.0	346	10.9	12.7	0.7	286.0	1.8	260.9
16	31 Jan 17 5:05 pm	2.8×10^{-14}	1.9	43.8	185	20.7	18.9	1.8	0.0	2.6	333.5
17	2 Feb 17 5:41 pm	7.6×10^{-15}	1.9	76.6	37	21.7	20.7	1.5	67.9	1.4	304.7

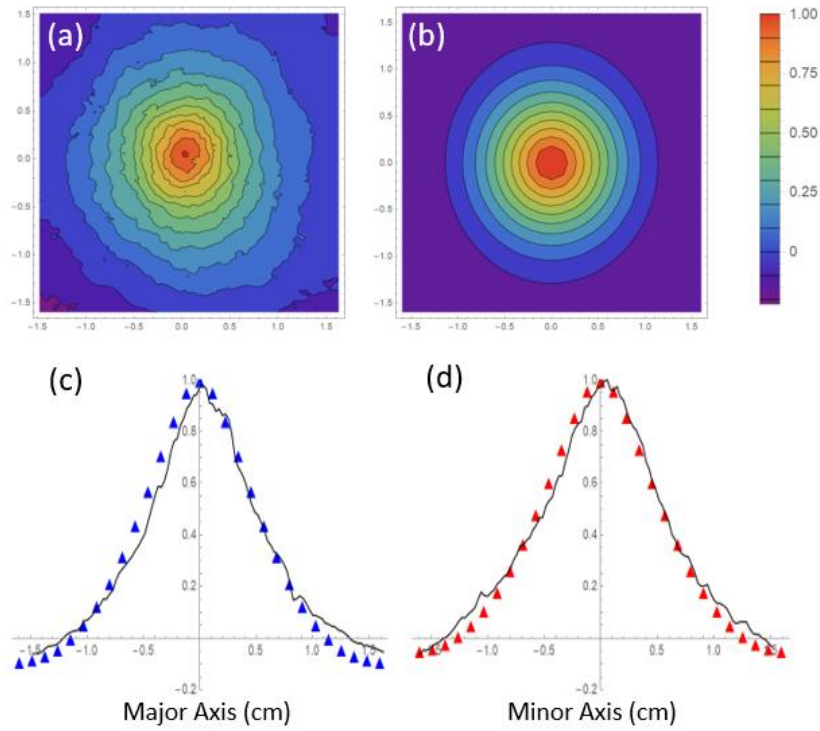


Figure 15. January 31, 2017, 9:12 am. Normalized CFI resulting from 1 km propagation (line) compared to theoretical calculation (triangle). Theoretical anisotropy ratio $\mu_y / \mu_x = 1/0.95$. No rotation angle. Scale factor of 0.75 (slight focus) was used in comparing data to theory. (a) measured normalized CFI, (b) theoretical normalized CFI, (c) measured (line) and theoretical (triangles) cross section through major axis (d) measured (line) and theoretical (triangles) cross section through minor axis. Reprinted with permission from [17], Optical Society of America.

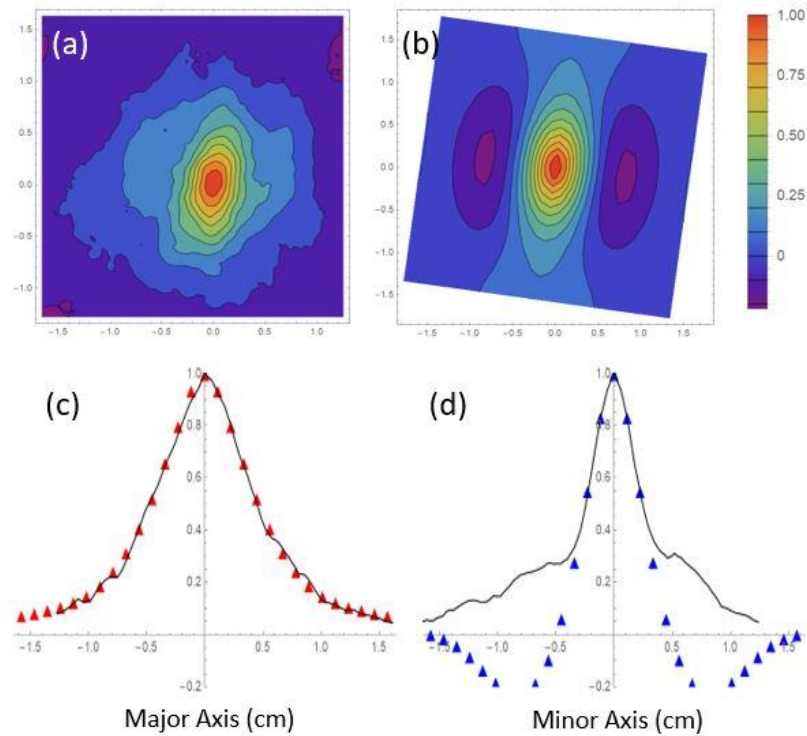


Figure 16. January 31, 2017, 5:05 pm. Normalized CFI resulting from 1 km propagation (line) compared to theoretical calculation (triangle). Theoretical anisotropy ratio $\mu_y/\mu_x = 1/0.6$. Theoretical were results rotated -8 degrees to obtain tilt of measured results. Scale factor of 0.45 (slight focus) was used in comparing data to theory. (a) measured normalized CFI, (b) theoretical normalized CFI, (c) measured (line) and theoretical (triangles) cross section through major axis (d) measured (line) and theoretical (triangles) cross section through minor axis. Reprinted with permission from [17], Optical Society of America.

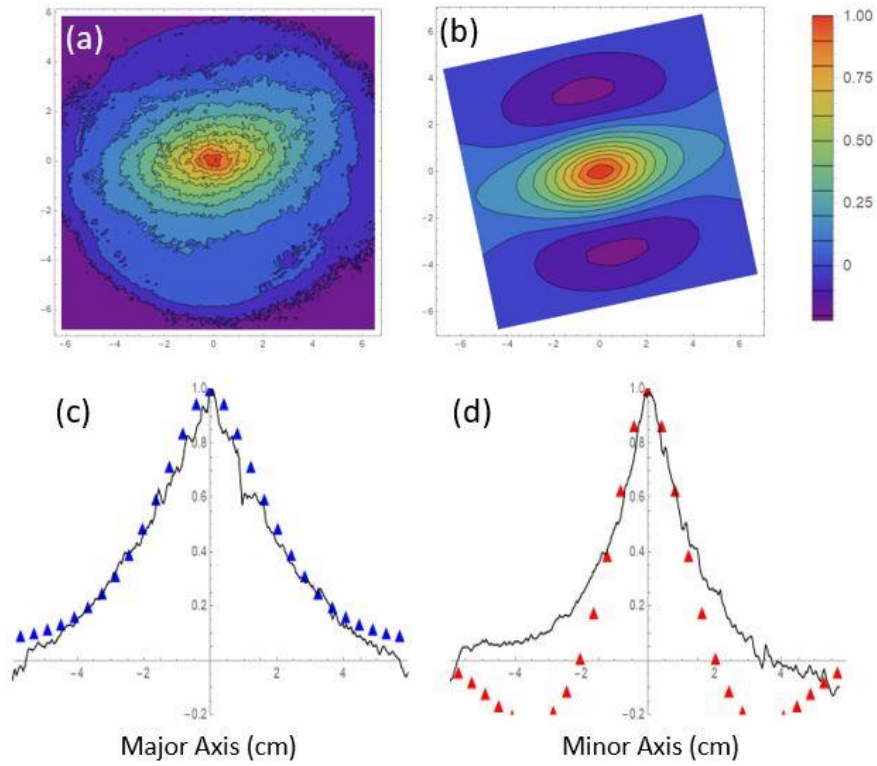


Figure 17. February 2, 2017, 5:41 pm. Normalized CFI resulting from 2 km propagation distance (solid line) compared to theoretical calculation (triangle). Theoretical anisotropy ratio $\mu_y/\mu_x = 0.6/1$. Theoretical results were rotated 12 degrees to obtain tilt of measured results. Scale factor of 1.9 (slight defocus) was used in comparing data to theory. (a) measured normalized CFI, (b) theoretical normalized CFI, (c) measured (line) and theoretical (triangles) cross section through major axis (d) measured (line) and theoretical (triangles) cross section through minor axis. Reprinted with permission from [17], Optical Society of America.

CHAPTER 6: EVOLUTION OF TURBULENCE OVER MULTIPLE DAYS

The work described in this chapter was published in JOSA A dated 27 June 2018 [19]. Data shown is the combination of two experiments. The first is the same experiment as described in Chapter 5, where coauthors performed the experiment but this author compiled and processed the data as well as analyzed the results. Joseph Coffaro assembled the system used in the second experiment; however, this author collected and analyzed all data. Both experiments were part of a large atmospheric data collection activity sponsored by Office of Naval research for atmospheric propagation of high energy lasers. This activity involved multiple atmospheric instruments and multiple researchers. This author utilized the collected data to aid in understanding of the phenomena. The camera data processing software was created by Christopher Smith and utilized by the author. Christopher Smith, Joseph Coffaro, Sarah Belichki, Jonathon Spsychalsky, Franklin Titus, Frank Sanzone, Bruce Berry and the author were responsible for collecting atmospheric data.

From Chapter 5, we know that anisotropic turbulence will cause equal contours of covariance function of intensity for a propagated plane wave to be elliptically shaped. In this case, the ellipticity of the center of the contours is a good indicator of the anisotropy ratio. Similarly, from Chapter 4, we discovered that equal contours of the scintillation index of a Gaussian beam are elliptical

after propagation through anisotropic turbulence. In this case, the ratio of major to minor axes of the scintillation index is nearly the same as the anisotropy ratio. In this chapter, we will consider the changing turbulence characteristics throughout four days over the SLF by examining the resulting CFI from propagation of a plane wave during the winter of 2017 and the resulting scintillation index from propagation of a Gaussian beam during summer of 2017. To our knowledge, this is the first time that the changing atmospheric statistics between isotropy and varying degrees of anisotropy throughout the day have been presented.

The SLF measurements were part of a large on-going collection of atmospheric data relevant to the propagation of high energy lasers which included many atmospheric devices. The data obtained from several of these devices is included in this work to help with understanding the complicated interaction of conditions which lead to isotropy or anisotropy of atmospheric turbulence statistics. Data from a Scintec BLS 900 located near the path of our laser is shown with the winter data while the data from a UCF-developed Short Range Scintillometer (SRS) located on a parallel path to our laser is shown with the summer results. Also, ground and air temperature probes as well as a pyrometer were located near the beginning of the propagation path for all tests. Sudden drops in solar flux indicate times of cloud cover over the pyrometer.

The conditions varied significantly for the two sets of measurements. For instance, during the winter measurements the temperature varied from a low of

3 C to a high of 29 C and the humidity was low. During the summer data collection, the temperature varied much less with a low of 24 C and a high of 33 C and it was hot and muggy with afternoon storms.

For all experiments, we propagated a 532 nm laser beam and measured the intensity fluctuation data using a Charge Coupled Device (CCD) array of a Prosilica GC660 camera with 659x493 pixels. In the January-February experiment, a near-plane wave beam was propagated either one or two kilometers at a height of 2 m above the ground. In the August experiments, the propagation path was 100 m again at a height of nearly 2 m.

Plots of wind data are shown for two anemometers located within the propagation path for the winter data and for one located near the receiver for the summer data. One minute averages were computed from the 10 Hz anemometer data to generate (u, v, w) velocity data. Wind direction was determined from the angle between horizontal components of the average wind based on a local coordinate system where 0° corresponds to wind blowing in the direction of propagation and 90° and 270° correspond to wind blowing perpendicular to the beam direction. Because of the inherent multivalued nature of angle calculations, large excursions are occasionally present in the plots which actually correspond to small angle changes. Five 90° quadrants are used in the plots to minimize the number of near 2π excursions.

As we have seen in previous chapters, a spectrum model such as given in Equations (4.1) or (5.3) will generate equal CFI or equal scintillation index

contours which are elliptical. Results from the following sections are based on this understanding.

6.1 CFI for Near Plane Wave, Winter 2017

On January 31 and February 2 of 2017, we recorded various atmospheric data at the SLF based on the requirements of a high energy laser program. During this, we propagated a 532 nm collimated Gaussian beam for one or two kilometers at a height of 2 m above the SLF runway. The experimental configuration is the same as that shown in Chapter 5 (Figure 13). The transmitted beam was 10 cm in diameter and was collimated by minimizing beam expansion at the receiver. The receiver consisted of a focusing lens and the CCD array of a Prosilica GC660 camera with 659x493 pixels. The CCD array was placed prior to the focus of the receiver lens such that the entire lens was visible on the CCD array. Spatial-temporal fluctuations of intensity were recorded at a rate of 60 frames per second for one minute. The camera exposure time was chosen based on the requirements of the project, which was not initially to determine anisotropy of turbulence. For this experiment, the exposure varied from 4.4 to 5.8 ms on January 31 and from 10 μ s to 1.2 ms on February 2. The camera has a global shutter so that data is collected from the entire CCD array simultaneously. Each pixel corresponded to a square of physical dimensions of approximately 0.2 mm x 0.2 mm. The intensity data was post processed for mean intensity, scintillation index and covariance of intensity. Even though measuring anisotropy of the

turbulence was not the focus of this experiment, we realized during post processing that anisotropy was often indicated. In evaluating this data, it is important to note that because of the relatively long exposure times for some of the data, some smearing may have occurred between pixels. However, since the wind direction was more nearly in the direction of propagation rather than transverse to propagation for the cases that indicated anisotropy, this is expected to have had a minimal effect.

As explained in Chapter 5, even though we are propagating a collimated Gaussian beam, the phase front of the beam is nearly planar since its Fresnel number is near zero and is well approximated by the plane wave CFI theory as developed in Chapter 5. To determine the isotropy/anisotropy of the turbulence, we will generate equal normalized CFI contours as described by Equations (5.13) - (5.15) recalling that ellipticity of the contours corresponds to propagation through anisotropic turbulence and that the strength of anisotropy is approximated by the major/minor axes ratio near the center of the figure. Only the center of the CCD is shown so as to emphasize the nonzero values of the CFI.

Figure 18 shows the normalized CFI for the morning and afternoon of January 31, 2017 after 1 km propagation of the near-plane wave beam. The near-circular symmetry of the 9:12 ET contours indicates isotropic turbulence while the ellipticity of the afternoon contours indicates the probable anisotropy of the turbulence. The strong turbulence direction (minor axis) is vertical at

15:32 ET and rotates to horizontal at 17:05 ET. Of the four measurement days, this is the only time that a 90° rotation in strong turbulence direction is seen over a short time. Both afternoon data sets correspond to an anisotropy ratio, μ_y / μ_x , of about 1.7 but with major/minor axes inverted between the two figures.

Because of the long camera exposure times during this data collection, there exists the possibility of elongation of the CFI in the horizontal direction, especially when the wind is blowing transverse to propagation ($\pm 90^\circ$). Because of similar wind speeds and directions, if elongation were occurring one would expect to see similar results in Figure 18 (a) and (b), but one appears nearly isotropic, and the other appears anisotropic. Also, the wind direction for the data corresponding to Figure 18 (c) was near 90°, and yet this figure is elongated vertically rather than horizontally.

The corresponding atmospheric and wind data are shown in Figures 19 and 20.

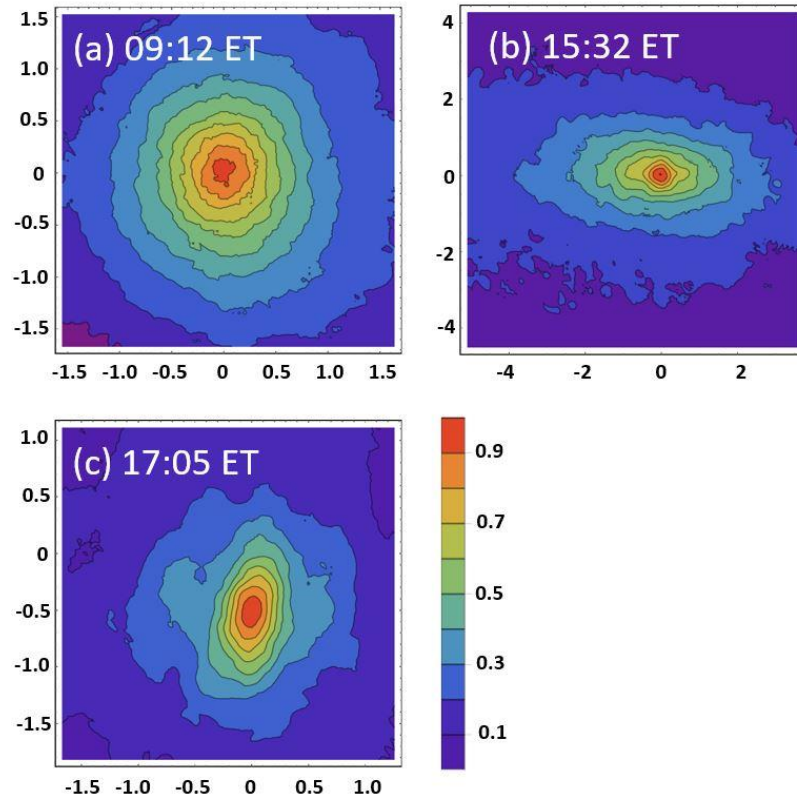


Figure 18. Contours of equal normalized CFI from 1 km propagation of 532 nm near-plane wave beam on January 31, 2017. Dimensions are in centimeters. Measurement times for (a)-(c) are given on the images. Reprinted with permission from [19], Optical Society of America.

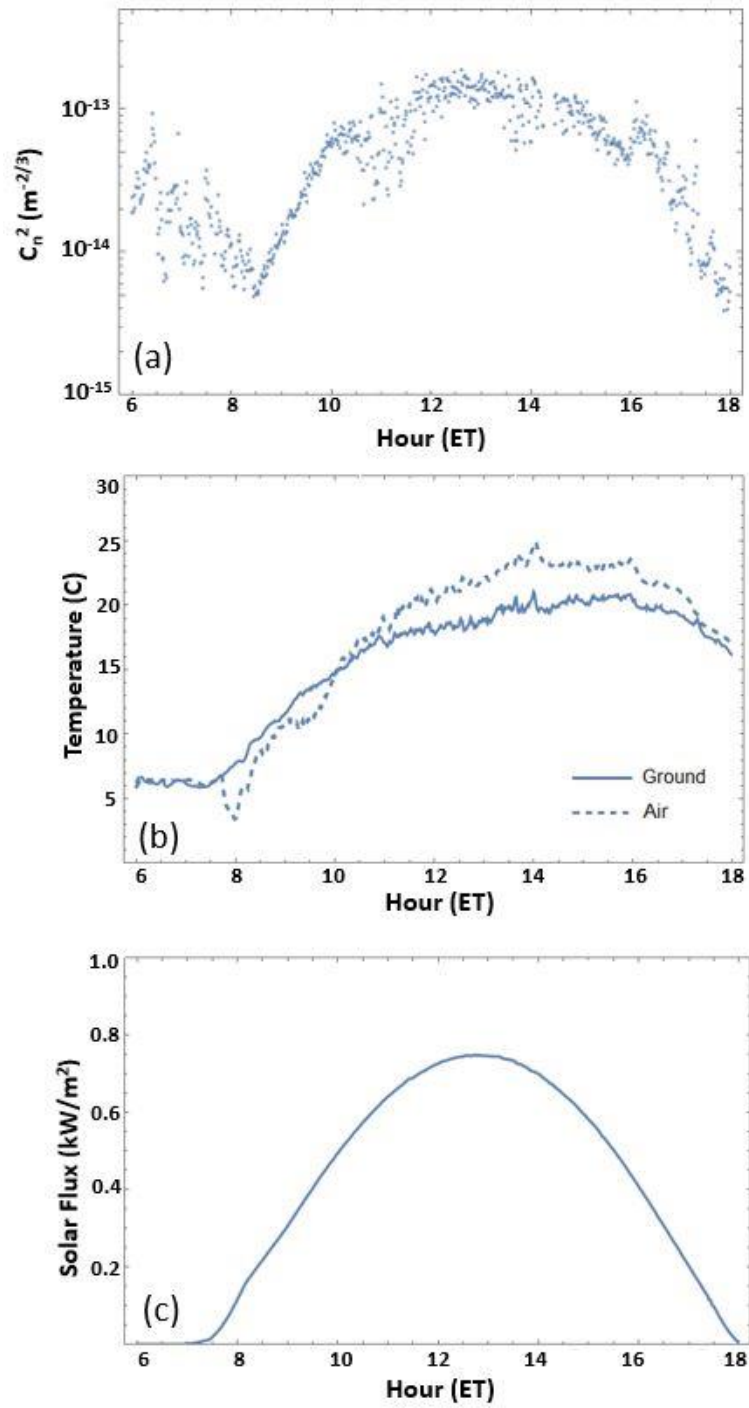


Figure 19. Atmospheric data from instruments located on SLF, January 31, 2017. (a) C_n^2 from Scintec BLS 900; (b) air and ground temperature on runway; (c) solar flux on runway. Reprinted with permission from [19], Optical Society of America.

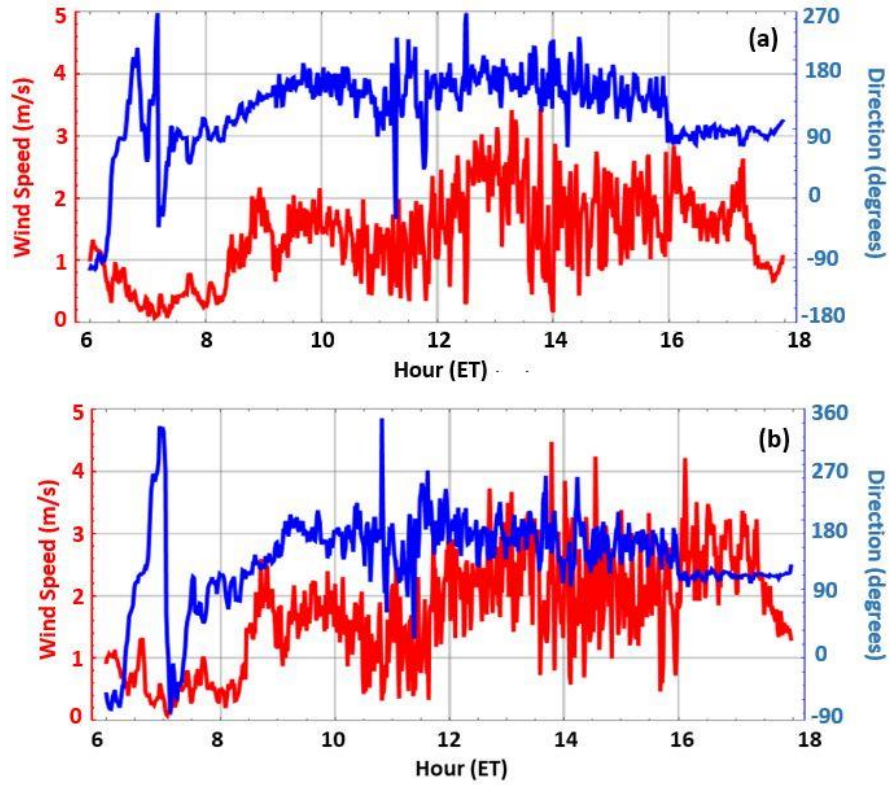


Figure 20. Wind magnitude (red) and direction (blue) from sonic anemometers located along propagation path on January 31, 2017. (a) Near start of path; (b) near middle of path. Reprinted with permission from [19], Optical Society of America.

Figure 21 appears to demonstrate the presence of relatively large anisotropic turbulence in the morning and late afternoon of February 2, 2017, with isotropic conditions during midday. Based on the center contour of the normalized CFI, anisotropy ratios of approximately 1.8 and 1.7 are present in the data from 7:50 ET and 17:41 ET, respectively. Since the camera exposure time was shorter for these data collection periods, there is less potential for broadening of the CFI in the horizontal direction than in the last data set. The

wind direction corresponding to 7:50 ET and 12:52 ET was within about 10° of being transverse to propagation, however, the wind speed was low (<0.5 m/s) at 7:50 ET, reducing the likelihood of data correlation between adjacent pixels, and the data from 12:52 ET appears to indicate isotropy.

Corresponding atmospheric and wind data are shown in Figures 22 and 23.

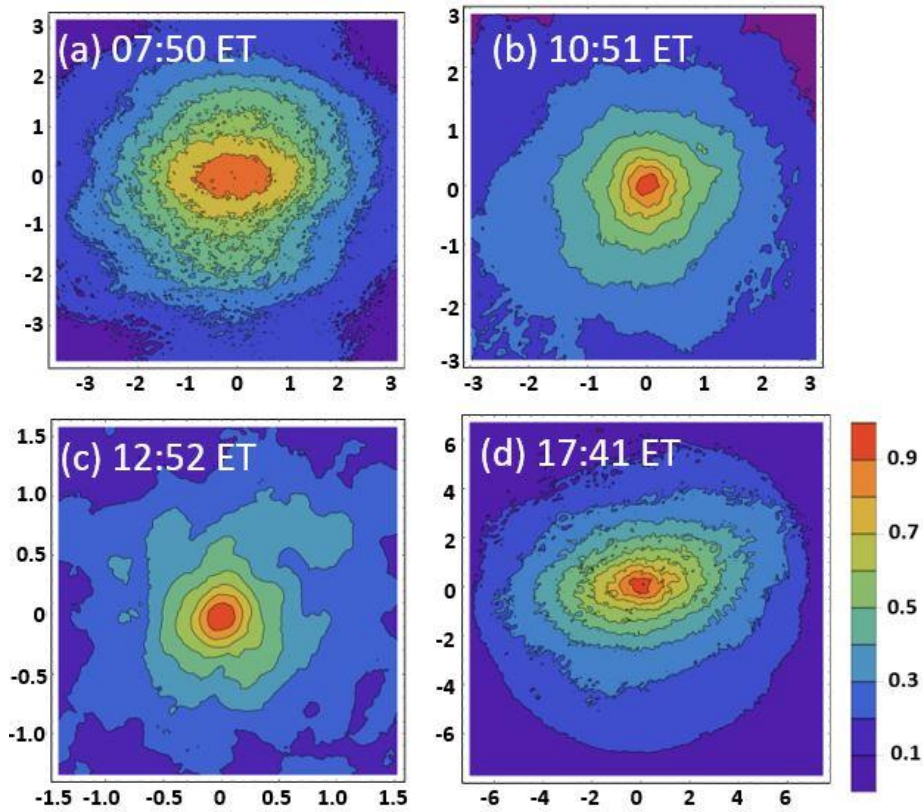


Figure 21. Contours of equal normalized CFI from 2 km propagation of 532 nm near-plane wave beam on February 2, 2017. Dimensions are in centimeters. Measurement times for (a)-(d) are given on the images. Reprinted with permission from [19], Optical Society of America.

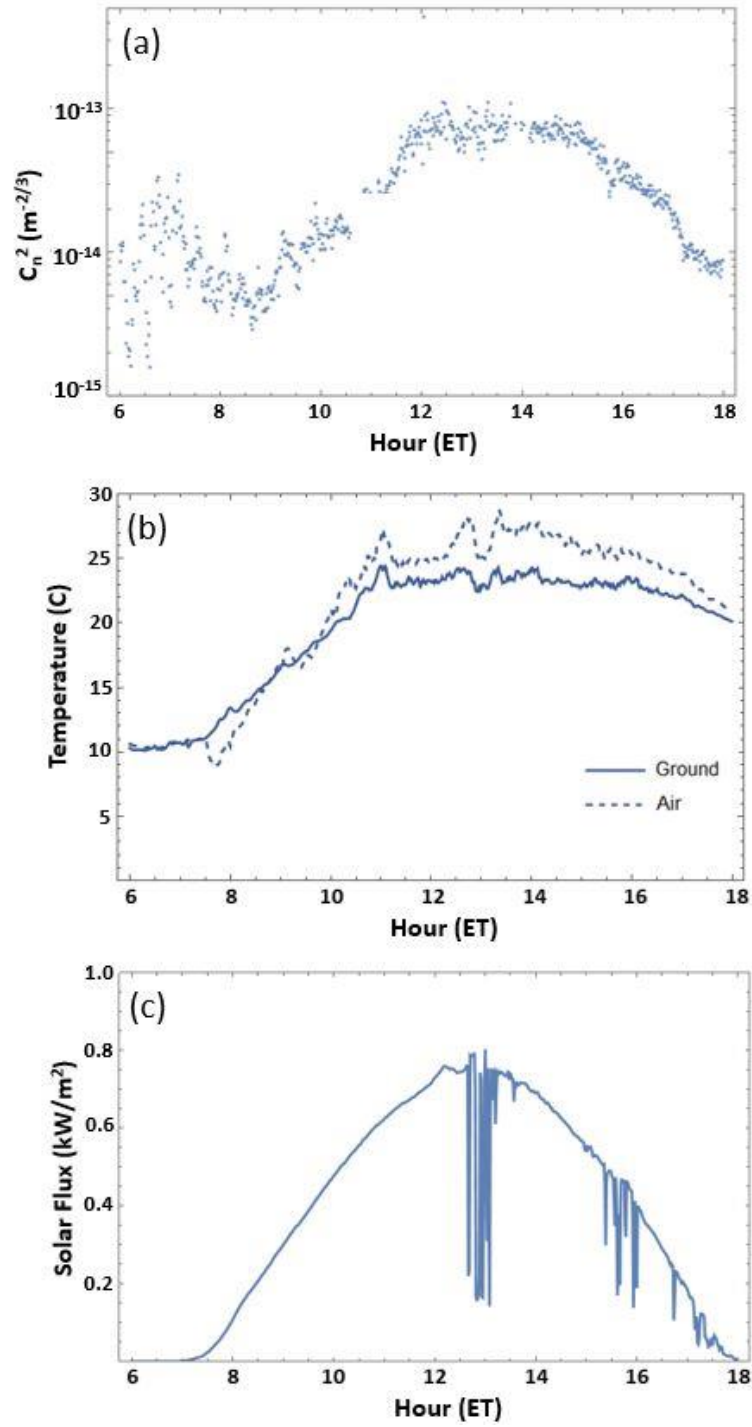


Figure 22. Atmospheric data from instruments located on SLF, February 2, 2017. (a) C_n^2 from Scintec BLS 900; (b) air and ground temperature on runway; (c) solar flux on runway. Reprinted with permission from [19], Optical Society of America.

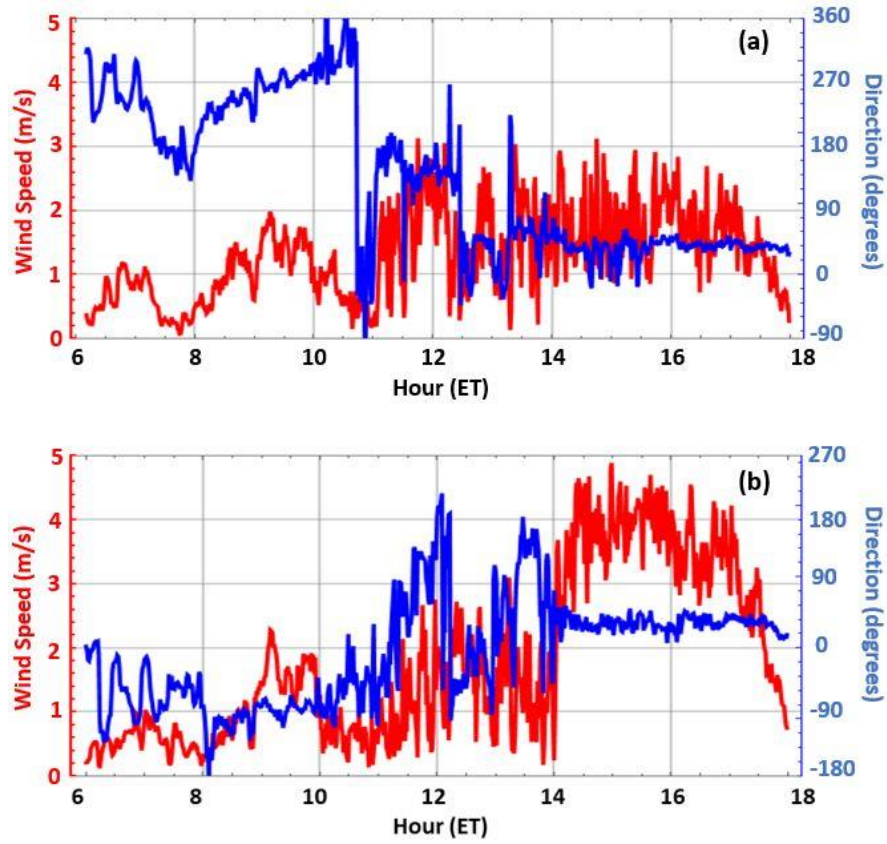


Figure 23. Wind magnitude (red) and direction (blue) from sonic anemometers located along propagation path on February 2, 2017. (a) Near start of path; (b) near end of path. Reprinted with permission from [19], Optical Society of America.

6.2 Scintillation Index for Gaussian Beam, Summer 2017

On August 1 and 3 of 2017, we propagated a collimated 532 nm Gaussian beam for 100 m over the SLF and collected intensity fluctuation data. Figure 24 shows an image of the beam as seen by the camera prior to propagation through the turbulence. From the previous work described in Chapter 4, we anticipated that if the beam propagated through anisotropic turbulence then contours of equal

scintillation index would be elliptical. The propagated beam was slightly elliptical with $1/e^2$ diameters of 25.8 mm and 24.0 mm in the horizontal and vertical directions, respectively, determined by fitting a Gaussian power curve to knife-edge data measurements. Intensity fluctuation data was collected at a rate of 120 frames per second for three minutes using a Prosilica GC660 CCD camera array with global shutter so that the entire image was collected simultaneously. Physically, one pixel corresponded to a square of approximately 0.25mm x 0.25mm. The transmitter was placed on an optical table inside a mobile lab at a height from ground of 2 m, and the receiver was in the back of a covered truck at a height of 1.7 m. The experimental layout is shown in Figure 25.

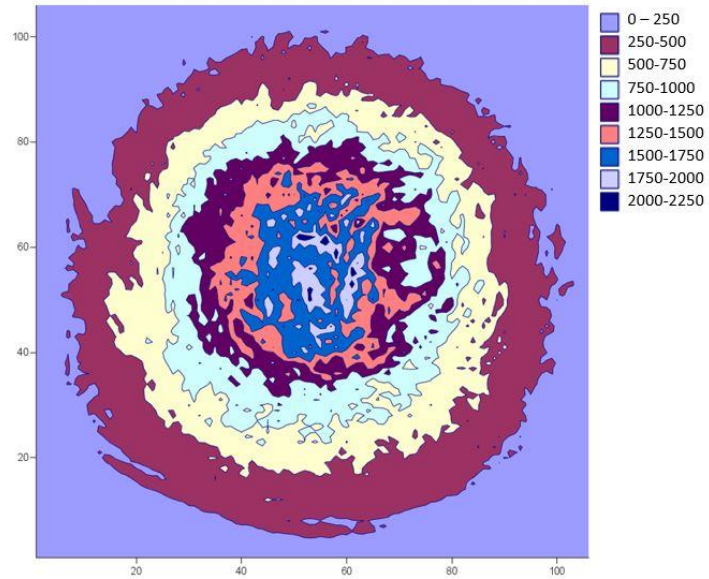


Figure 24. Equal intensity contours of 532 nm beam prior to propagation through turbulence. Axes correspond to pixels where only the region of the CCD with the beam is shown.

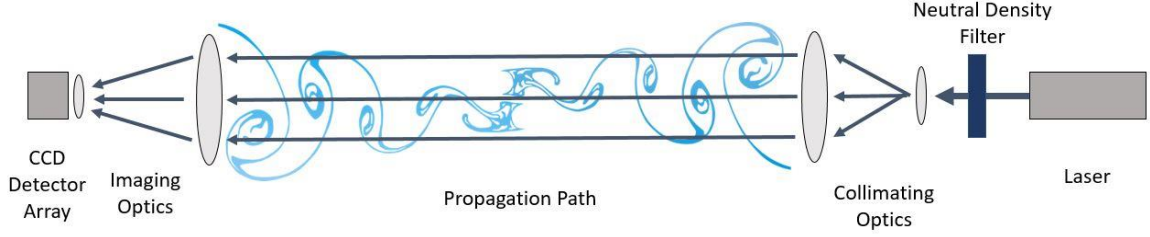


Figure 25. Experimental layout at SLF, August 2017. Reprinted with permission from [19], Optical Society of America.

The camera focus was adjusted to image a grid placed on the front of the receiver lens. However, the dominant source of energy was the beam passing directly through the lens and being focused down onto the CCD array rather than that scattering from the front surface of the lens. The camera aperture was smaller than the beam and thus the signal was clipped around the outer edges. There was also an additional effect, at first thought to be a slight tilt of the camera lens, which caused the major axis of the slightly elliptical beam to rotate from horizontal to vertical.

In Chapter 3 we defined the scintillation index as

$$\sigma_I^2(\mathbf{r}) = \frac{\langle I^2(\mathbf{r}) \rangle}{\langle I(\mathbf{r}) \rangle^2} - 1. \quad (6.1)$$

To compute the scintillation index contours from intensity fluctuation data, we used the discrete form of (6.1)

$$\sigma_I^2(x, y) = \frac{\frac{1}{N} \sum_{n=1}^N [I^{(n)}(x, y)]^2}{\bar{I}(x, y)} - 1 \quad (6.2)$$

where (x, y) represents a point on the CCD array and \bar{I} is as defined previously by Equation (5.14).

Examining the contours of equal scintillation index from August 1 (Figure 26), anisotropic turbulence appears to be present during the morning and late afternoon with conditions near isotropy occurring midday. As discussed in Chapter 4, theoretical models indicate that the true anisotropy ratio, μ_y / μ_x , is within about 10% of the major/minor axes ratio of the scintillation index contours. In Figure 26, the major/minor axes ratio varies from a high of around 1.8 early in the day to a low of about 1.3 midafternoon, increasing to around 1.6 late in the day. This indicates an anisotropy ratio of at least 1.6 during peak anisotropy periods to a low of as little as 1.2 in the afternoon. More exact estimates are not possible due to the slight ellipticity of the beam.

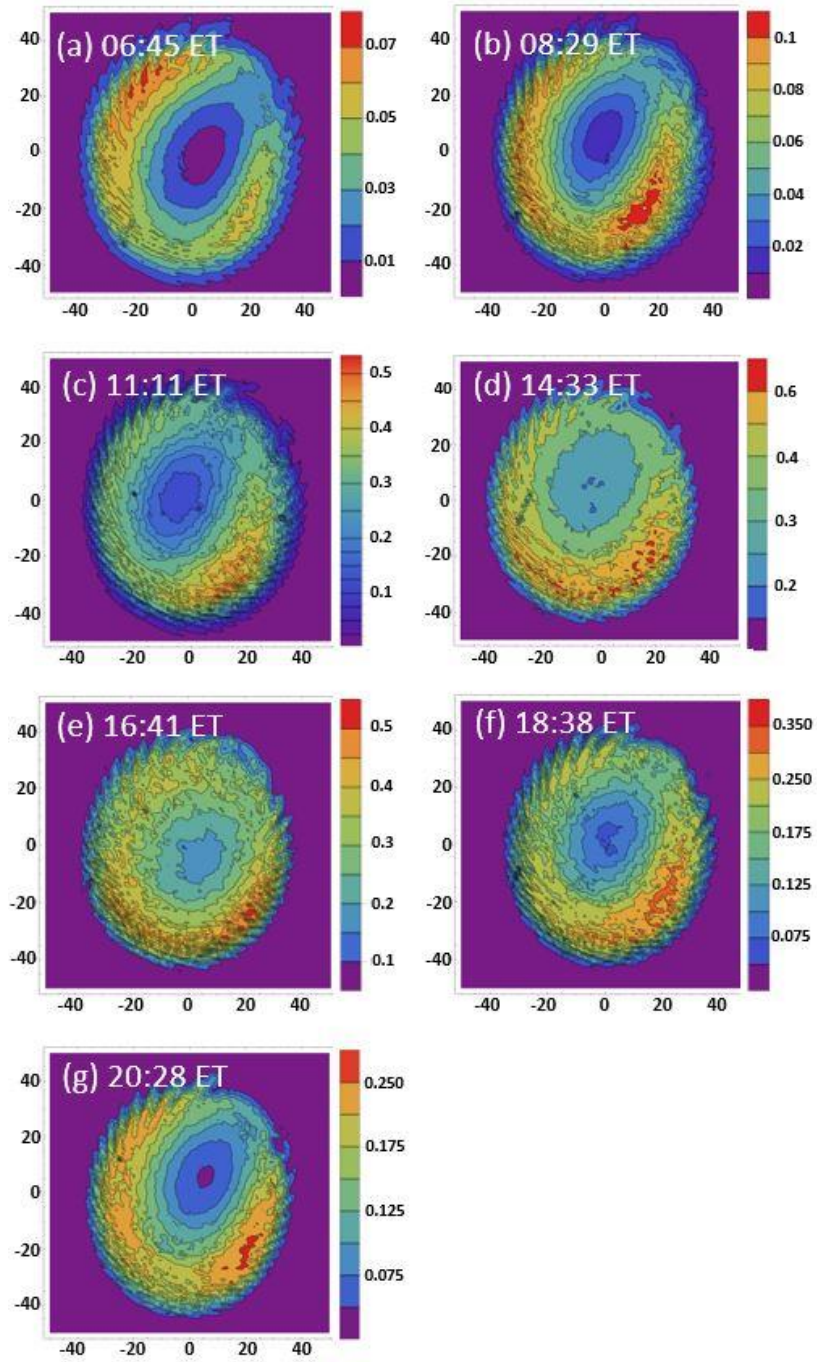


Figure 26. Contours of equal scintillation index from 100 m propagation of 532 nm Gaussian beam on August 1, 2017. Axes dimensions correspond to pixels. Measurement times for (a)-(g) are given on the images. Reprinted with permission from [19], Optical Society of America.

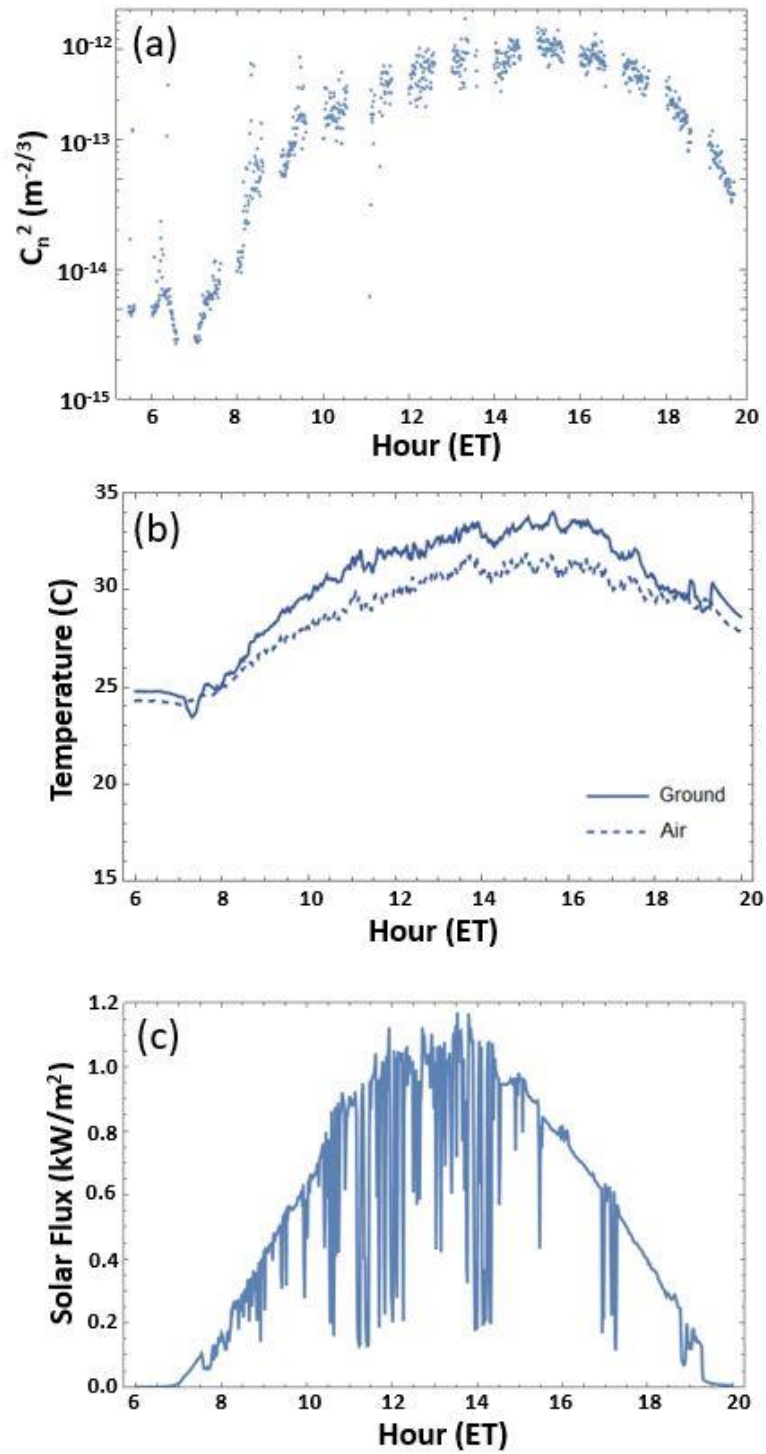


Figure 27. Atmospheric data from instruments located on SLF, August 1, 2017. (a) C_n^2 from SRS; (b) air and ground temperature on runway; (c) solar flux on runway. Reprinted with permission from [19], Optical Society of America.

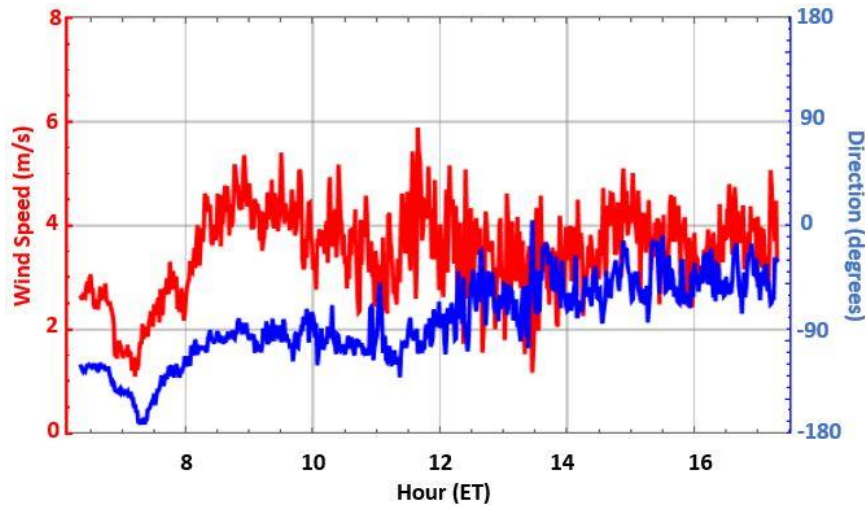


Figure 28. Wind magnitude (red) and direction (blue) from sonic anemometer located near receiver on August 1, 2017. Reprinted with permission from [19], Optical Society of America.

Multiple atmospheric instruments were located in the vicinity of the propagation path. This included ground and air temperature probes and pyrometer placed before the propagation path, UCF-developed SRS placed on a parallel path, and sonic anemometer placed near the receiver. The data from the instruments are shown in Figures 27 and 28.

The data collected on August 3 demonstrated similar behavior to that of previous days (Figure 29). Namely, the effect on the beam of propagation through the optical turbulence appeared to indicate anisotropy in the morning and late afternoon with nearly isotropic conditions midday. The major/minor axes ratio of the scintillation index contours varied from a high of about 1.7 in the morning to nearly isotropic midday and increased to about 1.6 later in the day. This implies a peak anisotropy ratio, μ_y / μ_x of at least 1.5 with a gradual transition

from its morning high to a value near 1 midday. Again, estimates are limited because of the ellipticity of the beam. The experimental configuration was changed slightly before taking the data represented by (f) and (g) by adding a diffuse surface in front of the receiver input lens. In this case, the recorded image was a blurred version of what impinged on the receiver lens rather than the dominant energy transmitted through the system as in all earlier data. As can be seen, the behavior when imaging off of the diffuse surface is the same as in all previous data sets which confirms that the data collection method is accurate.

Atmospheric and wind data are shown in Figures 30 and 31.

6.3 Experimental Observations

During all four days on the SLF and using two different experimental configurations, anisotropic conditions consistently appeared to be present in the morning and early afternoon while the statistics calculated from midday propagation appeared to indicate isotropic or near isotropic turbulence. The first data taken on the morning of January 31 appeared isotropic but earlier data may have indicated anisotropy. From the consistent turbulence evolution demonstrated in this data, it seems worth investigating to see if this trend continues throughout the night. For this large homogeneous concrete surface, isotropy may occur for only a few hours out of the day and anisotropy may be the more prevalent condition.

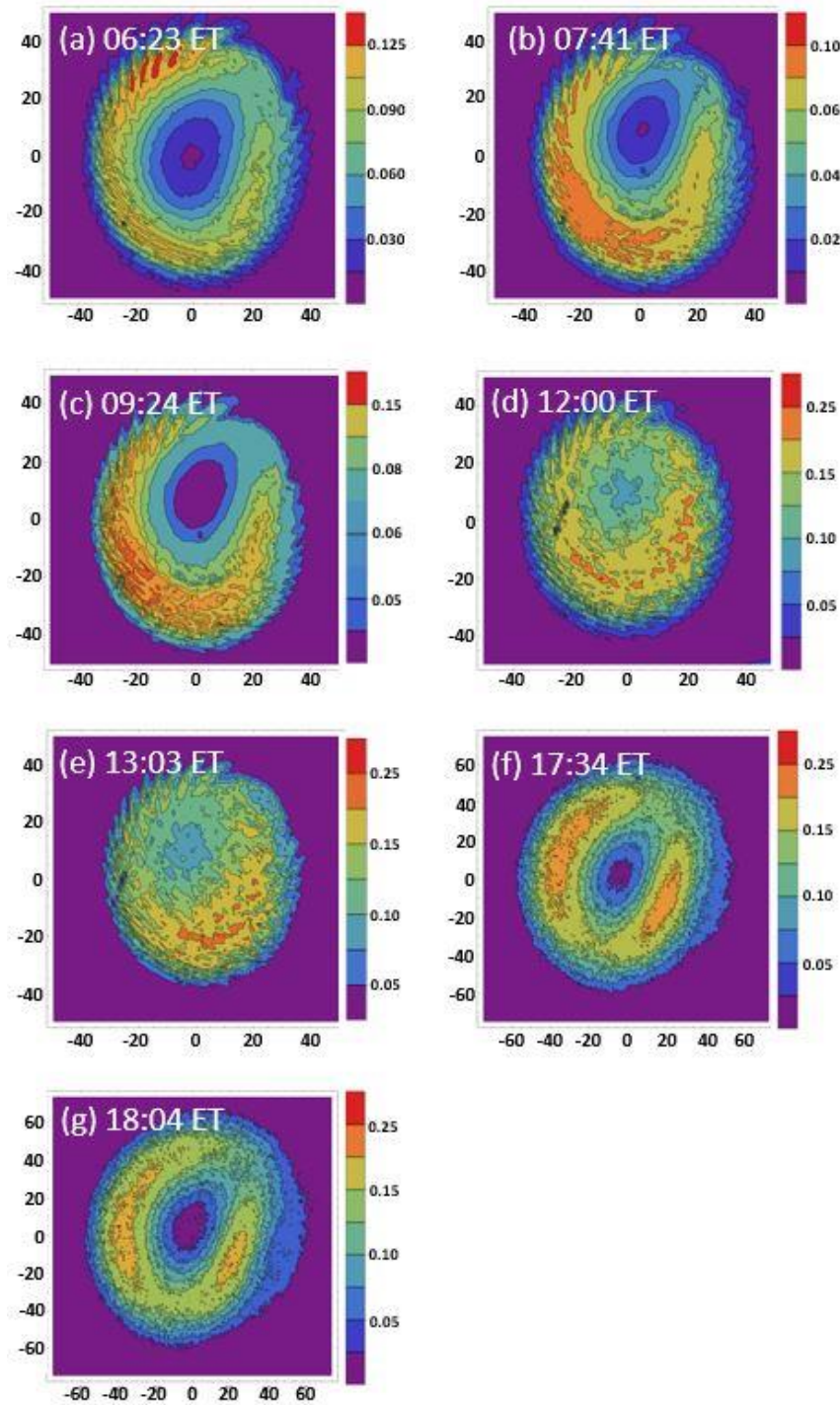


Figure 29 . Contours of equal scintillation index from 100 m propagation of 532 nm Gaussian beam on August 3, 2017. Axes dimensions correspond to pixels. Measurement times for (a)-(g) are given on the images. Reprinted with permission from [19], Optical Society of America.

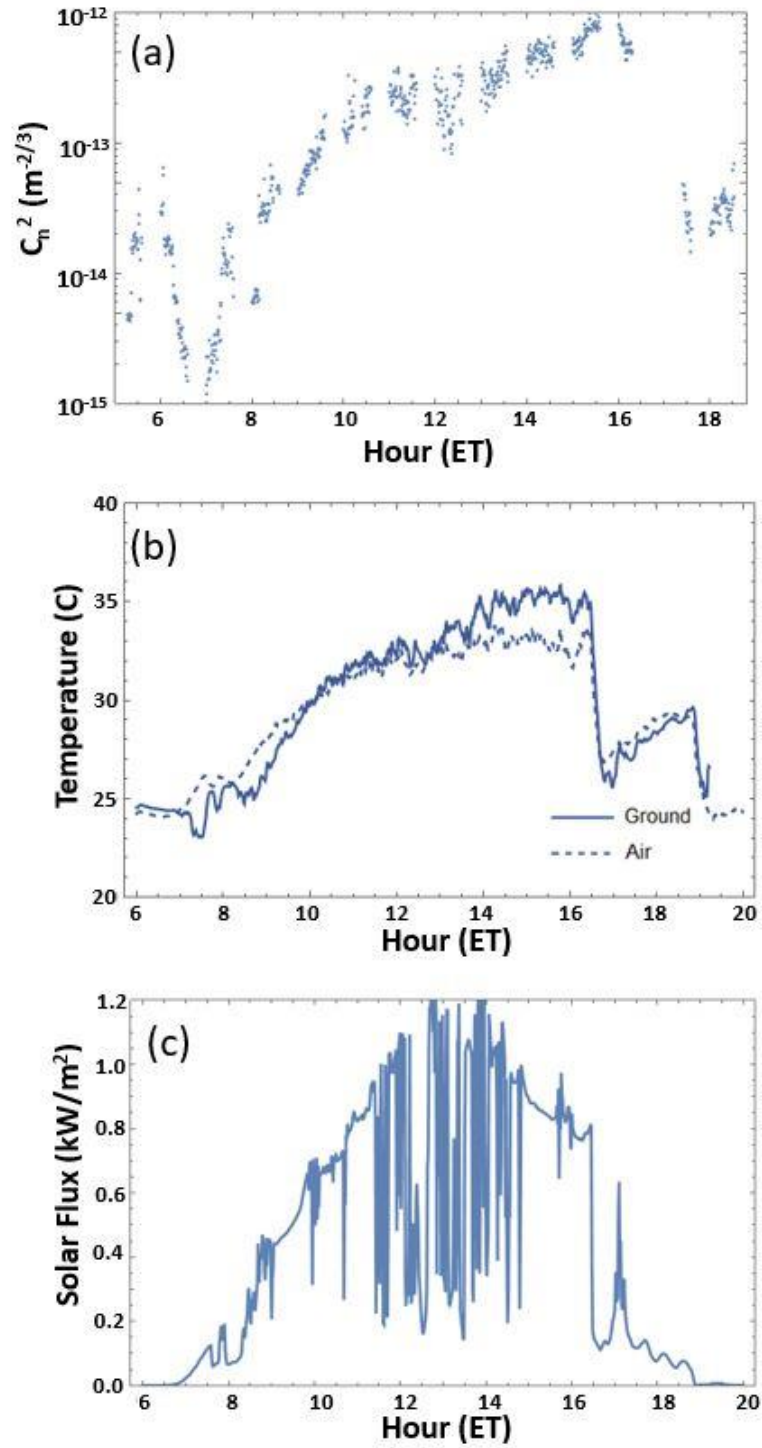


Figure 30. Atmospheric data from instruments located on SLF, August 3, 2017. (a) C_n^2 from SRS; (b) air and ground temperature on runway; (c) solar flux on runway. Reprinted with permission from [19], Optical Society of America.

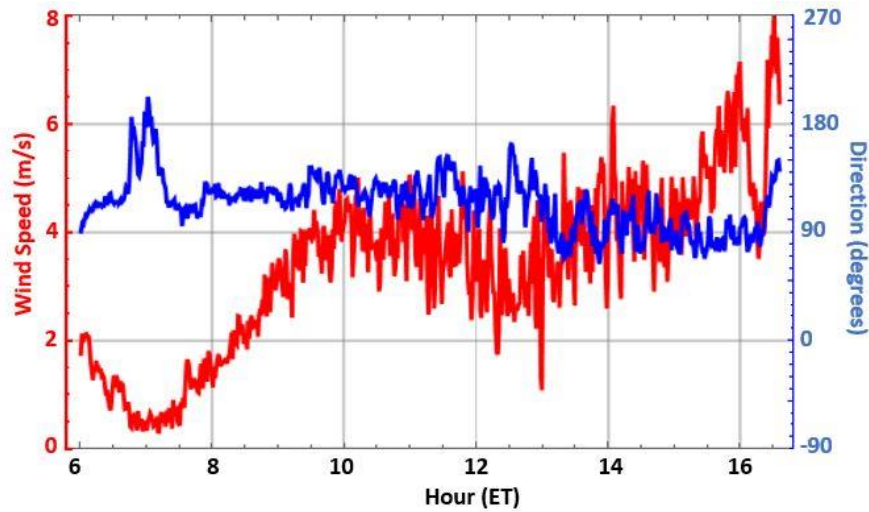


Figure 31. Wind magnitude (red) and direction (blue) from sonic anemometer located near receiver on August 3, 2017. Reprinted with permission from [19], Optical Society of America.

For this environment the anisotropy ratio achieved a maximum of less than 2 where over grass other researchers have reported a ratio as high as 3 [6]. During the winter experiments the maximum major/minor axes ratio was 1.7-1.8 and during the summer it was at least 1.6 with the ratio changing as the turbulence evolved and became more fully developed. The Rytov variance was generally much less than one with a short period of time during one day that it exceeded one slightly.

It is difficult to draw strong conclusions regarding conditions which lead to anisotropy by examining atmospheric data. We can make some generalizations but these are not consistent across all of the data. In general, anisotropic conditions were accompanied by lower C_n^2 and lower solar flux. Often the turbulence appeared to be anisotropic when the ground temperature was lower

than the air temperature, but again, not consistently. When measurements were made during the middle portion of the day, the data always indicated isotropic turbulence. At this time the wind speed was often higher and wind direction was more variable increasing mixing and leading to better developed turbulence.

Other researchers have reported a significant “tilt” in the anisotropy ellipses [6, 18] with similar wind speeds as during our measurements which has been attributed to wind direction [18]. However, in the data presented here, the normalized CFI from the winter data displays little or no tilt. In contrast, the scintillation-index contours from the summer experiments does display a significant tilt which varied little for all measurements regardless of wind direction. Due to the long path, the winter data represented had much larger irradiance fluctuations with all Rytov variances exceeding one. The lack of tilt in the winter data could be an integrated path effect or due to the stronger fluctuations.

If anisotropy were induced by the ground-air temperature difference, we would expect that the strong turbulence direction (minor axis of ellipse) would be vertical. In the January-February data, the strong turbulence direction was vertical except for the one case late in the afternoon where it was rotated. In contrast, when anisotropy appeared to be present in the August measurements, its strong direction was always more nearly horizontal than vertical.

While we made significant progress in proving the existence of anisotropic turbulence near the ground and developed methods to measure it, neither experiment was optimum; some of the exposure times were longer than optimum

for the winter experiments presenting the opportunity for correlation, or smearing, between adjoining pixels and the propagated beam changed from slightly elliptical horizontally to slightly elliptical vertically. Based on these experiences, we developed a significantly improved experimental configuration which will be discussed in the next chapter.

CHAPTER 7: BEAM SHAPING AND ANISOTROPY

The work discussed in this chapter was presented at the SPIE Laser Communications and Propagation through the Atmosphere and Oceans VII conference in August of 2018 and published in the conference proceedings [20]. This work continued the multi-team atmospheric propagation of high energy lasers project sponsored by the Office of Naval Research. As part of this, the paper coauthors collected the atmospheric and wind data which the author analyzed and plotted. The author developed all of the theory and performed all analysis of collected data. With the aid of Frank Sanzone, she designed and assembled the optical system. The author also set up the system and collected the data with help from coauthors where multiple sets of hands were needed.

During recent experiments at two significantly different locations, we saw unexpected results when examining the intensity statistics resulting from propagation of a Gaussian beam. With the theoretical development discussed in previous chapters, we had expectations of what equal mean-intensity and scintillation-index contours should look like after propagation of a Gaussian beam through either isotropic or anisotropic turbulence. While some of the contours display the expected behavior, many did not. At times, the mean intensity and scintillation index contours were elliptical in ways that did not correspond to propagation through anisotropic turbulence. Because of this, we considered other effects that could lead to the observed intensity and scintillation index contours.

With the understanding that the index of refraction is the mechanism that causes changes in the beam, we began to consider the possibility of a quasi-deterministic gradient in the index of refraction in addition to the statistical index variations. We realized that propagation through a nonlinear index gradient could reshape the beam and scintillation index in the manner evidenced by the data. Recently, Voronsov and Kulikov have begun to consider the effect of propagating a beam a long distance in the vicinity of a temperature inversion layer [21, 22] which lends validation to our supposition.

While we do not have definitive data supporting the conjecture of a nonlinear temperature gradient, temperature patterns near the ground are complicated and could affect the beam. In this chapter, we introduce a simple model that incorporates both a nonlinear index gradient and anisotropic turbulence. This model is based on a “thought experiment” to extend existing theory and is not sufficient for in-depth analysis however this model yields interesting results that help us to understand the behaviors that were seen in the data. In the part 7.1 of this chapter, we develop the model and show simulated results for conditions which include isotropy/anisotropy and nonlinear index gradient. In section 7.2, we will discuss experimental results from three days of experimentation that took place between the SLF concrete runway in May of 2018 and the TISTEF grass range in July of 2018.

7.1 Mathematical Model and Predicted Behavior

To gauge the possible impact of a nonlinear index gradient on the beam shape, we begin by evaluating the diffraction equation in the absence of turbulence (free-field) but with the introduction of an index function, $n(x)$. It is interesting to note that propagation through a linear gradient retains the original beam shape; a nonlinear function is necessary to shape the beam. For simplicity, the function is chosen to be one dimensional. Because some of the data seems to behave somewhat like propagation through a very long focal length lens, we chose a form for the index function that is similar to a Gaussian lens. In particular, let's examine what happens with propagation through an index gradient of the form

$$n(x) = \Delta n \exp\left(-\frac{x^2}{2W_0^2}\right). \quad (7.1)$$

The above index function is likely not what is actually present near the ground. For instance, the beam could propagate through multiple gradients along the path. The integrated effect on the beam from propagation over a long path seems to behave similarly to assuming a gradient index of the form of (7.1) over the extended path.

Incorporating an index function into the diffraction equation, the propagated free-field form of a collimated beam is

$$u_0(x', y', z) = -\frac{ik}{2\pi z} \int_{-\infty}^{\infty} \int_{-\infty}^{\infty} n(x) \exp(in(x)kz) \exp\left[\frac{in(x)k}{2z}((x-x')^2 + (y-y')^2)\right] u_0(x, y, 0) dx dy \quad (7.2)$$

Here (x, y) correspond to a location on the beam transverse to the propagation direction, z is path length in direction of propagation, and $k = 2\pi / \lambda$ is the wavenumber.

The initial form of the beam is the TEM_{00} mode defined by

$$u_0(x, y, 0) = \exp\left[-\frac{(x^2 + y^2)}{W_0^2}\right] \quad (7.3)$$

We will evaluate this using parameters that correspond to the experimental configuration discussed later. Namely, an initial $1/e^2$ intensity radius of the beam $W_0 = 6.5 \text{ mm}$, path length $z = 100 \text{ m}$, and wavelength $\lambda = 632.8 \text{ nm}$. Figure 32 compares the resulting intensity contours from propagation with no index gradient and when the magnitude of the gradient $\Delta n = 2 \times 10^{-9}$.

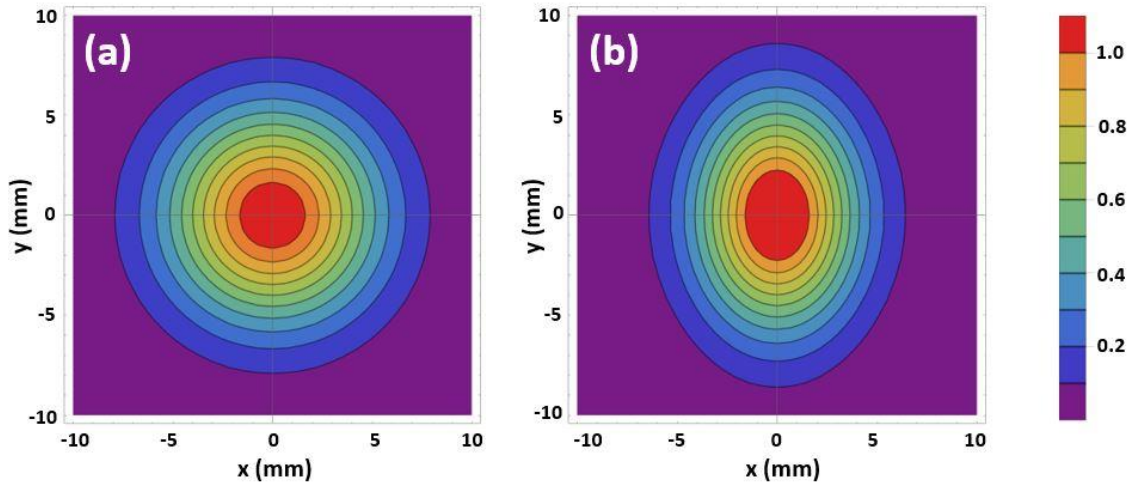


Figure 32. Effect of an index gradient on free-field propagation of a Gaussian beam. (a) Beam after 100 m propagation with no index gradient; (b) beam after 100 m propagation with index gradient of $\Delta n = 2 \times 10^{-9}$.

We can find the magnitude of the temperature gradient that would correspond to an index gradient along the path of $\Delta n = 2 \times 10^{-9}$ using [23]

$$n \cong 1 + 0.000293 \frac{P}{P_0} \frac{T_0}{T} \quad (7.4)$$

where $T_0 = 300 \text{ K}$, P is pressure and P_0 is standard atmospheric pressure. With the assumption that $P = P_0$, the corresponding temperature gradient is given by

$$\Delta T = T_2 - T_1 = T_1 \left[1 - \left(1 - 11.38 \Delta n T_1 \right)^{-1} \right] \quad (7.5)$$

Setting $T_1 = 300.15 \text{ K} (27 \text{ C})$, gives a corresponding magnitude for the temperature gradient of only $\Delta T = 2 \times 10^{-3} \text{ C}$. Therefore, as demonstrated by the contours in Figure 32, a slight temperature gradient that persists for the entire path length could result in significant beam shaping even over a short path.

The analysis up to this point has shown that an index gradient of the form of (7.1) *could* result in a beam shaping similar to our experimental results. Now that we understand the possible source of the beam shaping, we will develop a simple model for mean intensity and scintillation index that considers only the final shape of the beam and not the process by which that shape was generated.

The scintillation index of a Gaussian beam can be divided into the sum of an axial (or longitudinal) component and a radial component.

$$\sigma_I(x, y, L) = \sigma_{I,l}(L) + \sigma_{I,r}(x, y, L) \quad (7.6)$$

where L is the propagation distance and (x, y) correspond to a transverse location relative to the propagation path. Noting that the axial component,

$\sigma_{I,l}(L)$, is additive across all points and thus will not impact the shape of equal-contour plots, we will focus our work on the radial component, $\sigma_{I,r}^2(x, y, L)$.

Neglecting the effect of inner and outer scale, the radial component of the scintillation index can be approximated by [3]

$$\sigma_{I,r}^2(x, y, L) \cong 4.42 \sigma_R^2 \Lambda^{5/6} \frac{(x^2 + y^2)}{W^2} \quad (7.7)$$

where $\sigma_R^2 = 1.23 C_n^2 k^{7/6} L^{11/6}$ is the Rytov variance, $\Lambda = \frac{2L}{kW^2}$ and W is the $1/e^2$ beam radius at distance L .

The mean intensity after propagation through is given by

$$\langle I(x, y, L) \rangle = \exp \left[-\frac{2(x^2 + y^2)}{W^2} \right] \exp \left[\frac{\sigma_{I,r}^2(x, y, L)}{2} \right]. \quad (7.8)$$

where $\langle I(x, y, L) \rangle$ has been normalized by the on-axis mean intensity.

To simulate the effect of an index gradient, we will carry out a “thought experiment” to help us develop a model that incorporates the complicated phenomena of both anisotropy and beam shaping. The following discussion is preliminary and does not incorporate the rigorous mathematics necessary for a deep understanding of these effects. However, prior to development of these rigorous models, this thought experiment may provide insight into the complicated combination of these effects.

Consider a Gaussian beam propagating through *isotropic turbulence* which by some force, possibly the above discussed index gradient, becomes

elliptical after propagating distance L with beam radii in the x and y directions given by W_x and W_y , respectively. Let us also write the radial component of the scintillation index at any point (x, y, L) as the sum of the x contribution and the y contribution as we did when expressing the scintillation index as the sum of a radial and a longitudinal component. In this case, we can rewrite (7.7) and (7.8) as

$$\begin{aligned}\sigma_{I,r}^2(x, y, L) &\cong 4.42 \sigma_R^2 \left(\frac{\Lambda_x^{5/6} x^2}{W_x^2} + \frac{\Lambda_y^{5/6} y^2}{W_y^2} \right) \\ \langle I(x, y, L) \rangle &= \exp \left[-2 \left(\frac{x^2}{W_x^2} + \frac{y^2}{W_y^2} \right) \right] \exp \left[\frac{\sigma_{I,r}^2(x, y, L)}{2} \right]\end{aligned}\quad (7.9)$$

In this equation, $\Lambda_x = \frac{2L}{k W_x^2}$ and $\Lambda_y = \frac{2L}{k W_y^2}$.

To introduce *anisotropic turbulence* into our model, we recall the expression for the radial component of the scintillation index resulting from nonclassical turbulence (anisotropy and nonKolmogorov power law) developed in Chapter 4. In weak turbulence with no inner and outer scales, the off-axis component of the scintillation index can be approximated by

$$\begin{aligned}\sigma_{I,r}^2(x, y, L) &\cong \frac{4\pi \Gamma\left(2 - \frac{\alpha}{2}\right)}{\alpha - 1} A(\alpha) \tilde{C}_n^2 k^{4 - \frac{\alpha}{2}} L^{\frac{\alpha}{2} - 1} \Lambda^{\frac{\alpha}{2}} \int_0^{2\pi} \left(\frac{x \cos \phi}{\mu_x} + \frac{y \sin \phi}{\mu_y} \right)^2 \left(\frac{\cos^2 \phi}{\mu_x^2} + \frac{\sin^2 \phi}{\mu_y^2} \right)^{\frac{\alpha}{2} - 2} d\phi \\ A(\alpha) &= \frac{1}{4\pi^2} \Gamma(\alpha - 1) \cos\left(\frac{\alpha\pi}{2}\right)\end{aligned}\quad (7.10)$$

where \tilde{C}_n^2 is a generalized version of the structure function parameter with units of $m^{3-\alpha}$, α corresponds to the turbulence power law, μ_x and μ_y are the

anisotropy parameters as described previously. For this work, we will assume the classical value of $\alpha = 11/3$ for consistency with Equation (7.7) and utilize the definition of Λ to obtain

$$\sigma_{I,r}^2(x, y, L) = 1.73 \tilde{C}_n^2 k^{7/6} L^{11/6} \int_0^{2\pi} \frac{\Lambda^{5/6}}{W^2} \left(\frac{x \cos \phi}{\mu_x} + \frac{y \sin \phi}{\mu_y} \right)^2 \left(\frac{\cos^2 \phi}{\mu_x^2} + \frac{\sin^2 \phi}{\mu_y^2} \right)^{-1/6} d\phi. \quad (7.11)$$

As in the isotropic case, we will assume different beam diameters in the x and y directions. Grouping the x and y related terms, we can estimate

$$\sigma_{I,r}^2(x, y, L) \cong 1.73 \tilde{C}_n^2 k^{7/6} L^{11/6} \int_0^{2\pi} \left(\frac{\Lambda_x^{5/12} x \cos \phi}{W_x \mu_x} + \frac{\Lambda_y^{5/12} y \sin \phi}{W_y \mu_y} \right)^2 \left(\frac{\cos^2 \phi}{\mu_x^2} + \frac{\sin^2 \phi}{\mu_y^2} \right)^{-1/6} d\phi \quad (7.12)$$

We have now developed a model which should yield a rough estimate for the behavior of the beam in a scenario involving both anisotropic turbulence and a force which shapes the beam such as a nonlinear index gradient. The expected mean intensity is still given by (7.9) but with this modified form for the radial component of the scintillation index. This effort began from seeking possible explanations for experimental results where we do not know what caused the beam to become elliptical at some times but we do know the final beam diameters in orthogonal directions as well as the scintillation index across the beam. It was for this reason that we developed a simple model where we could use approximate values for beam diameter in orthogonal directions to estimate how the scintillation index and mean intensity contours might behave under various combinations of anisotropy and index gradient.

We will now look at the four possible combinations of anisotropy and beam shaping to gain understanding of the more complicated experimental results. Note that since the beam is infinite in extent in the theoretical model, the scintillation index will increase infinitely. This is not realistic; beams have finite extent. This results experimentally in the scintillation index increasing with distance from the optical axis and falling off as it reaches the beam edge. Figures 33 - 35 show equal mean-intensity and equal radial-component of the scintillation index for various combinations of anisotropy and beam shaping. Axial cuts are included along the contour sides to aid in understanding of the phenomena.

Figure 33 shows equal contours for mean intensity and radial scintillation index for a collimated Gaussian beam of initial $1/e^2$ intensity radius of 6.5 mm and propagation distance of 125 m path length with strength of turbulence of $C_n^2 = 5 \times 10^{-14} m^{-2/3}$ and with no nonlinear index gradient but with and without anisotropy. As expected, with isotropy both the mean intensity and scintillation index are circularly symmetric. In contrast, with an anisotropy ratio of $\mu_y / \mu_x = 1/2$ and moderate strength of turbulence, the mean intensity contours remain circular over this short path but the radial scintillation index is elliptical. When the strength of turbulence is increased to $C_n^2 = 5 \times 10^{-13} m^{-2/3}$ (Figure 34) the beam begins to appear elliptical while the scintillation index contours appear the same as with less turbulence but the scintillation has increased by an order of magnitude. It is important to note that in the case of anisotropy leading to an

elliptical beam, the major axis for the mean intensity contours is rotated 90° from that of the scintillation index.

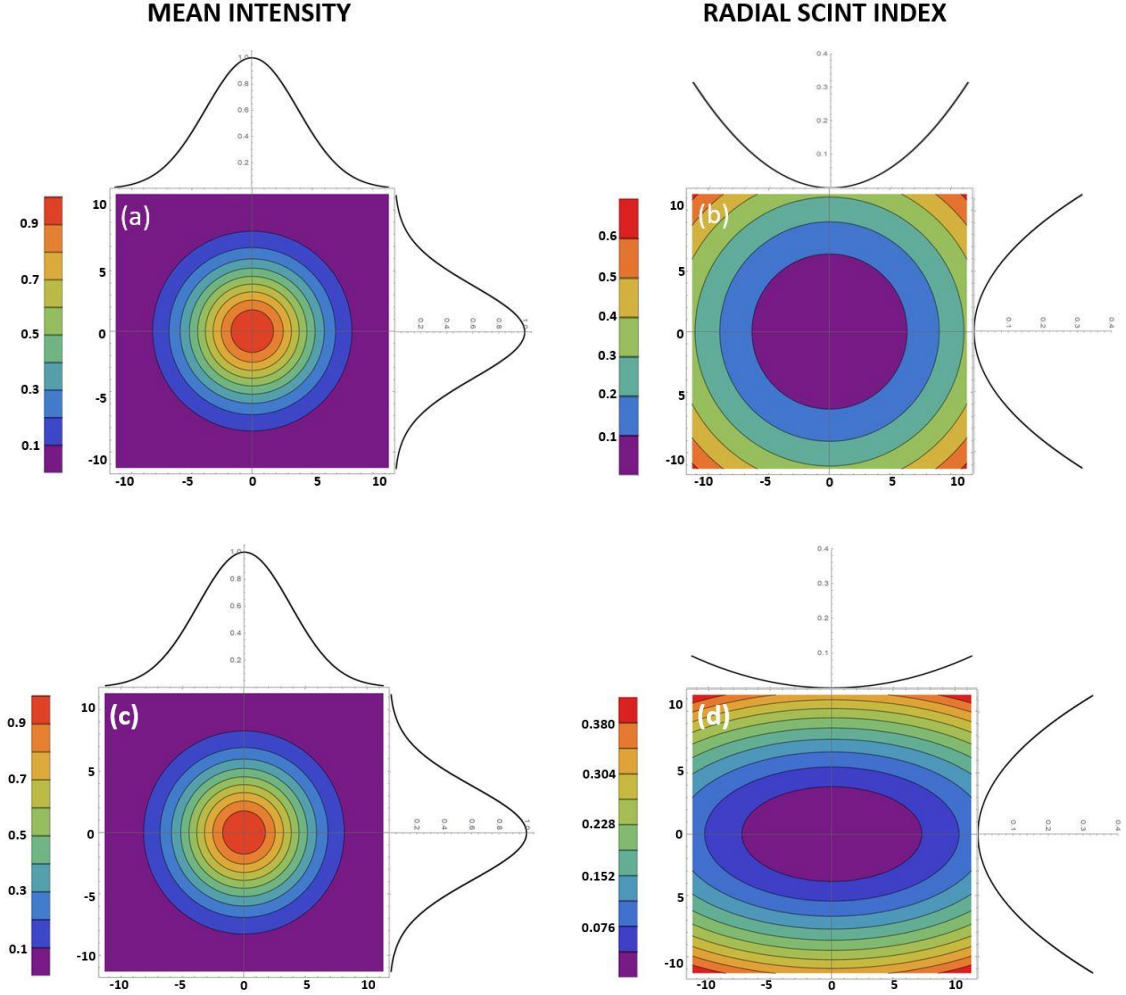


Figure 33. Anisotropy combinations without index gradient and $C_n^2 = 5 \times 10^{-14} m^{-2/3}$. Figure dimensions are in mm. (a), (b) Mean intensity and radial component of scintillation index for isotropic turbulence. (c), (d) Mean intensity and radial component of scintillation index for anisotropic turbulence with $\mu_y / \mu_x = 1/2$.

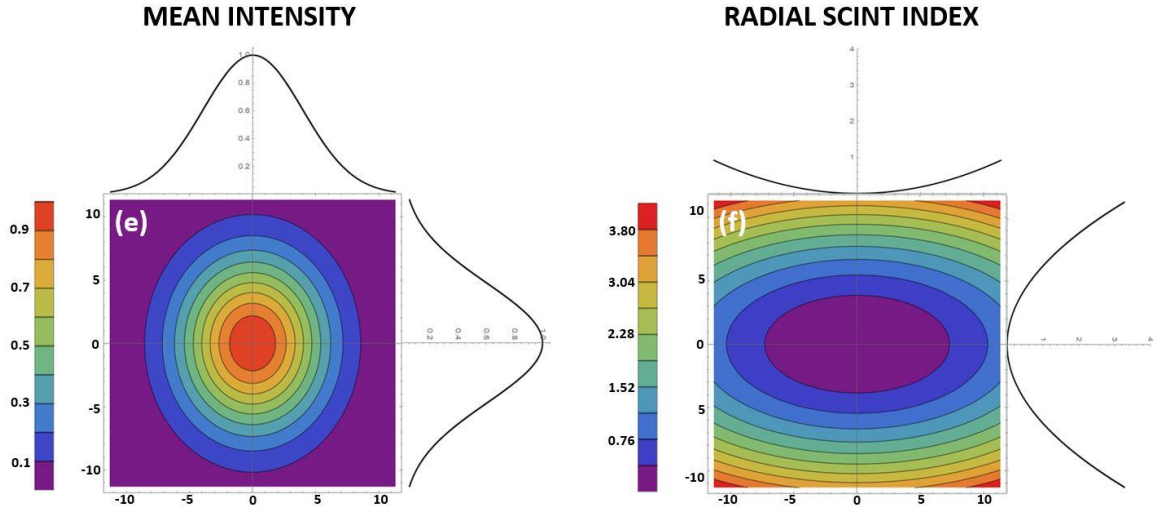


Figure 34. (a), (b) Mean intensity and radial component of scintillation index for anisotropic turbulence with $\mu_y / \mu_x = 1/2$, $C_n^2 = 5 \times 10^{-13} m^{-2/3}$ and no beam shaping.

The theoretical results for the same beam propagated through an index gradient with and without anisotropy are shown in Figure 35. For these contours $W_x = 0.75W_y$, $W_y = 7.2mm$, $C_n^2 = 5 \times 10^{-14} m^{-2/3}$ and the path length was again 125 m. With beam shaping and isotropic turbulence, the mean intensity and radial scintillation index are both elliptical with major axes in the same direction. However, when anisotropy is also present, the mean intensity over this short path will retain the same ellipticity but the scintillation index contours can vary from round to elliptical in any direction depending on the direction and strength of anisotropy. The tendency for the scintillation index ellipses to mimic the mean intensity ellipses could in essence be canceled as shown in the figure.

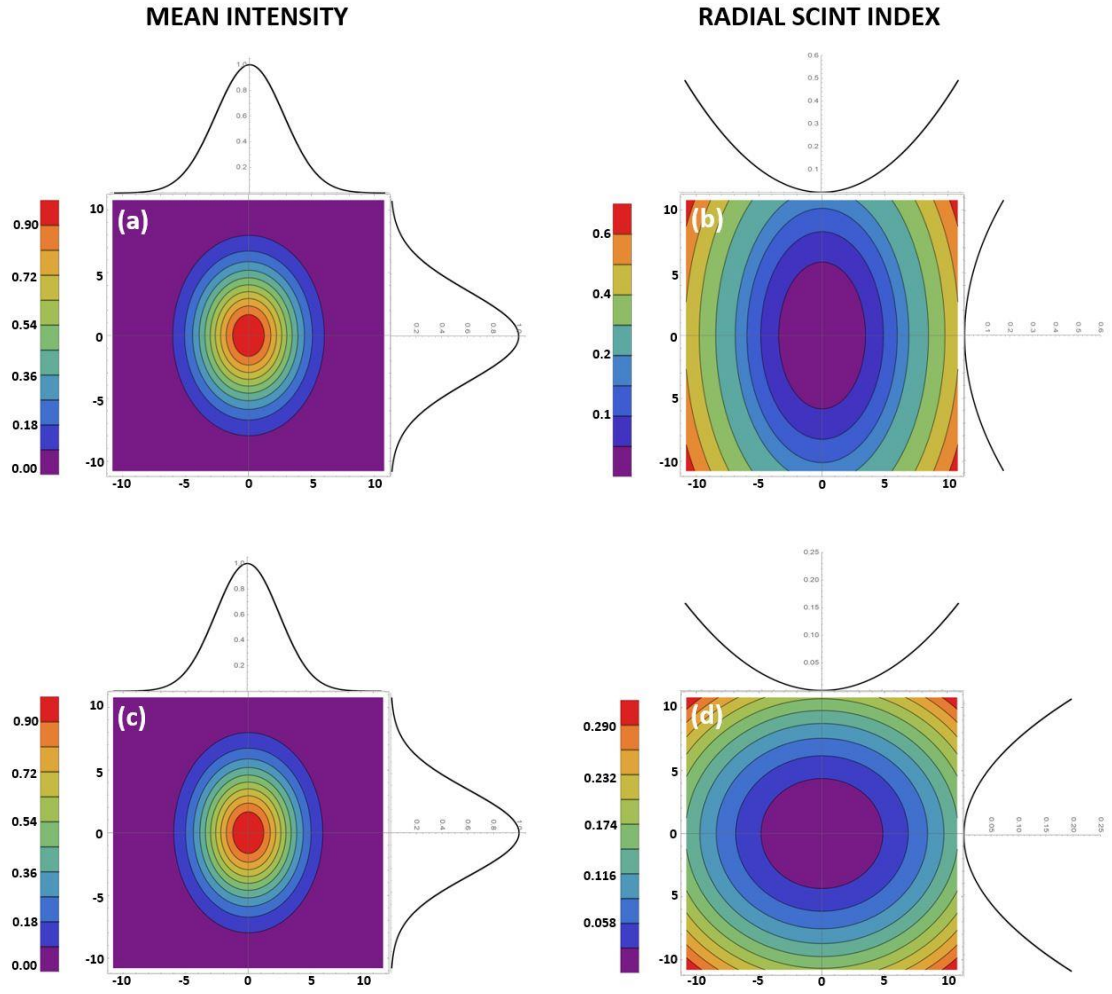


Figure 35. Anisotropy combinations with beam shaping where $W_x = 0.75W_y$ and $C_n^2 = 5 \times 10^{-14} m^{-2/3}$. (a), (b) Mean intensity and radial component of scintillation index for isotropic turbulence. (c), (d) Mean intensity and radial component of scintillation index for anisotropic turbulence with $\mu_y / \mu_x = 1/2$.

7.2 Experiment

In an effort to characterize the anisotropy and power law of optical turbulence near the ground, we propagated a collimated Gaussian beam for 100 m or 125 m at one of two locations and calculated the resulting mean intensity and scintillation index. The first experiments took place over the SLF runway on May 1 and 3, 2018. We repeated the same experimental set up at the TISTEF grass range on July 3, 2018. As can be seen from Figure 36, these propagation environments are significantly different. The SLF is a large concrete runway measuring 4,572 m in length by 91 m wide with well-maintained grass along each side. In contrast, the maintained portion of the TISTEF range is grass 1 km in length by 30 m wide with heavy brush along each side.

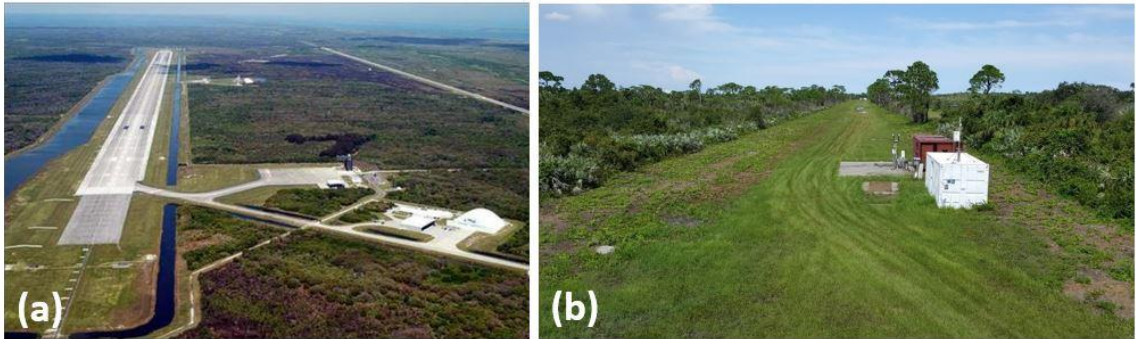


Figure 36. (a) SLF concrete runway; (b) TISTEF grass range.

7.2.1 Experimental layout

The transmitter consisted of a 0.8 mW, 632.8 nm, TEM₀₀ mode, helium neon laser (Edmunds Scientific Model 1107P) and collimating optics. The beam which exited the transmitter was collimated to have a $1/e^2$ radius of 6.5 mm. Particular care was given to system alignment to ensure that a circularly symmetric beam left the transmitter and that in the laboratory the beam remained circular as seen by the CCD array (Figure 37). The beam was propagated along the center of the range at a height of 2 m to the back of an enclosed truck which housed the receiver unit. The receiver was the combination of down collimating optics and a Prosilica GC660 CCD array. Two by two pixels were binned together on the array to increase the available frame rate. The camera exposure was set to 15 – 30 μ s depending upon strength of scintillation and data was collected at a rate of 150 fps. The data was processed using an algorithm which centered the frame based on its centroid so as to remove beam wander from the data. The layout is shown in Figure 38.

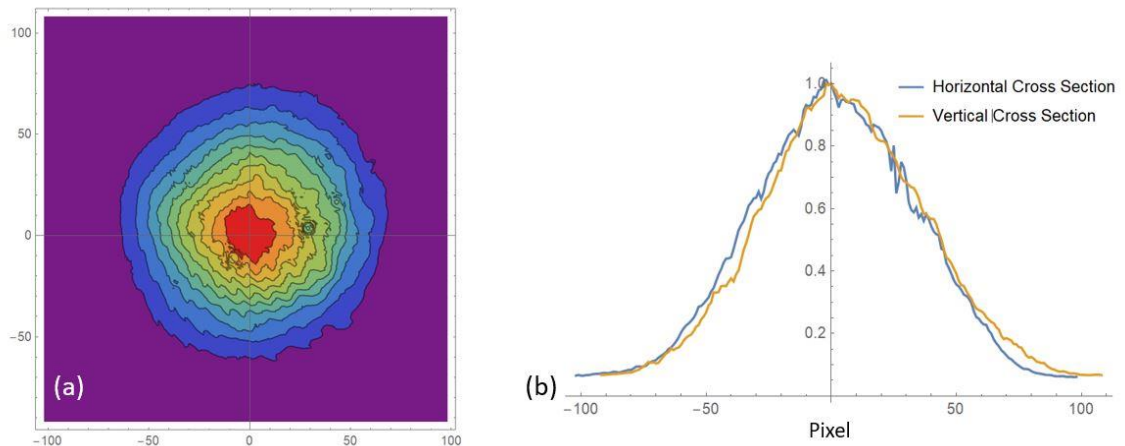


Figure 37. (a) Beam as seen by camera; (b) cross sections of beam at center.

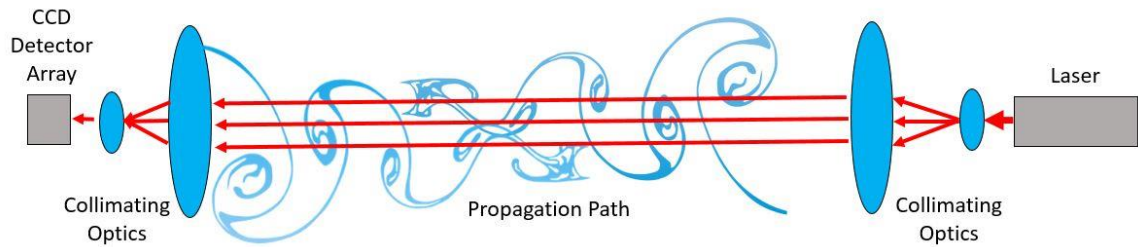


Figure 38. Experimental layout.

7.2.2 Experimental results

Equal mean-intensity and scintillation-index contours are shown in Figures 39-41 corresponding to selected data from the three days of testing. Mean intensity plots were normalized for consistency amongst the data. The contours

shown indicate the extremes of the variability in mean intensity and scintillation index measured over the multiple days. The turbulence appeared to vary from isotropic to anisotropic and often had ellipticity in intensity which seemed to indicate the presence of a beam-shaping phenomena. Specific details of each day are discussed below.

On May 1, 2018 we propagated the circularly symmetric Gaussian beam for 100 m along the center of the SLF. A UCF-developed optically-based scintillometer was on a parallel path nearby measuring C_n^2 and inner scale and a sonic anemometer was placed mid path to gather wind data (Table 2). The anemometer data was taken by colleagues from the Air Force Institute of Technology and supplied to us as part of the multi-group atmospheric measurement effort. The body of data from May 1 seemed to indicate various combinations of index gradient type event and anisotropy during the morning and evening with isotropic turbulence with no beam shaping during the middle portion of the day. Figure 39 shows two examples from this data set. The plots from 10:52 ET indicates the presence of a nonlinear shaping event while that from 14:32 ET has no beam shaping and appears to correspond to isotropic turbulence.

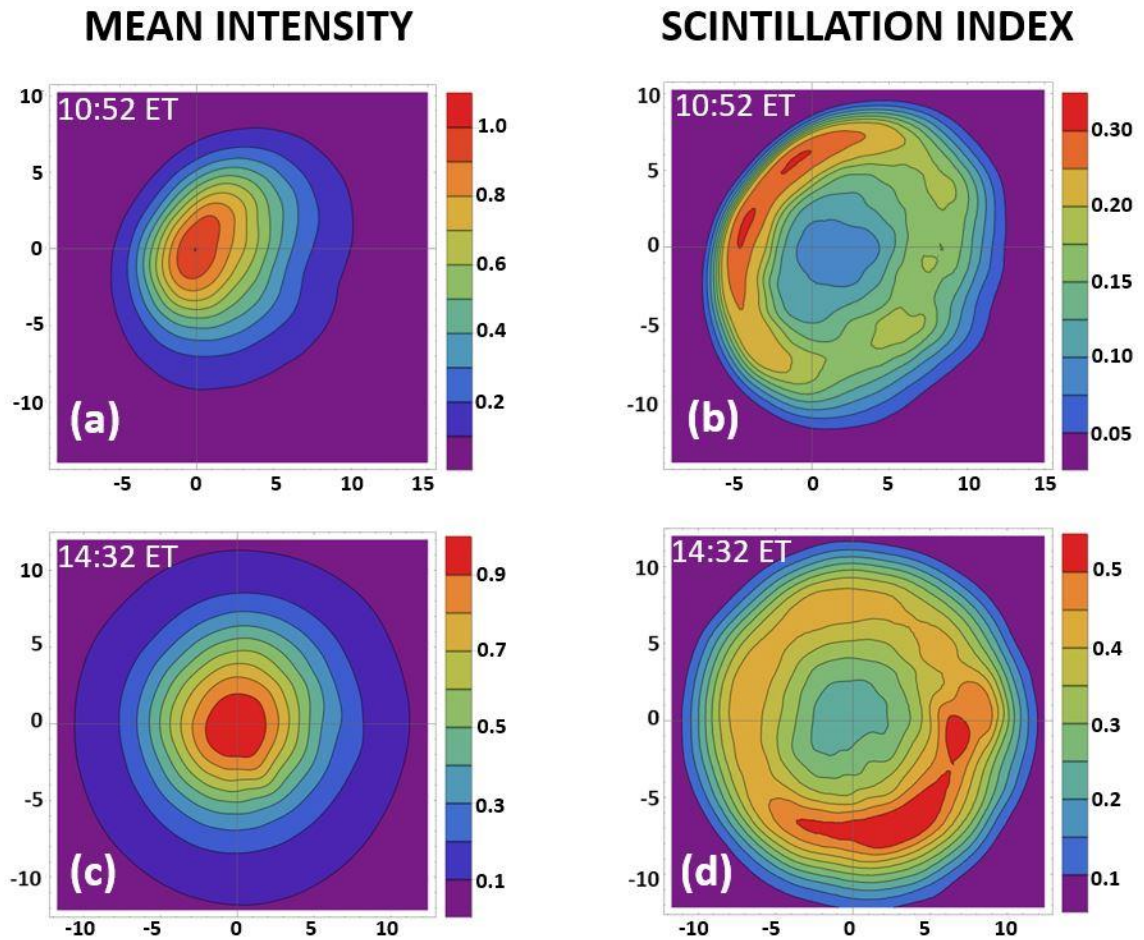


Figure 39. Measured mean intensity and corresponding scintillation index contours resulting from propagation of 6.5 mm radius beam for 100 m at SLF on 1 May 2018. Dimensions are in mm. (a-b) 10:52 ET; (c-d) 14:32 ET.

Because of the low levels of scintillation at 100 m, we decided to increase the path length to 125 m on May 3. The UCF scintillometer and anemometer maintained the same relative location as during the earlier test. Selected mean-intensity and scintillation-index contours are shown in Figure 40. Throughout this day, the beam rarely indicated the presence of isotropy without beam shaping. Instead, measurements often displayed characteristics of propagation through

anisotropy, an index gradient, or some combination of both. At 7:43 ET both the mean intensity and scintillation index are round indicating near isotropic conditions and no index gradient along the path. The mean intensity and scintillation index contours from 9:10 ET correspond to our theoretical prediction of a beam shaping event like an index gradient since both sets of contours have major axes in the same direction. At 10:32 ET, the mean intensity contours are circular but the center of the scintillation index is elliptical suggesting the presence of anisotropic turbulence. In contrast, the beam at 13:48 ET is elliptical but the center of the scintillation index contours is nearly round which may correspond to the presence of both effects.

The same experimental layout was assembled over the center of the TISTEF grass range propagating for 125 m on July 3, 2018. An anemometer was placed midrange to collect wind data and a Scintec BLS 900 measured C_n^2 over the full 1 km length of the range. There were periods of time in the early morning and afternoon where the data appeared to correspond to isotropic turbulence with no beam shaping effects. However, as at the SLF, there were also periods of time where the beam statistics appeared to indicate anisotropy or propagation through an index gradient or a combination of both. Selected mean-intensity and scintillation-index contours are shown in Figure 41. The data from 9:18 ET corresponds to that predicted for propagation through an index gradient since both the mean intensity and scintillation index have elliptical contours with major axis in the same direction. At 10:07 ET the beam is elongated which seems to

indicate a gradient type effect but the scintillation index contours are round in the center. As in the theoretical example, this may indicate the presence of both a beam shaping effect and anisotropic turbulence. At 18:51 ET the beam is round but the center of the scintillation index is elliptical which is what we expect for anisotropic turbulence with no index gradient.

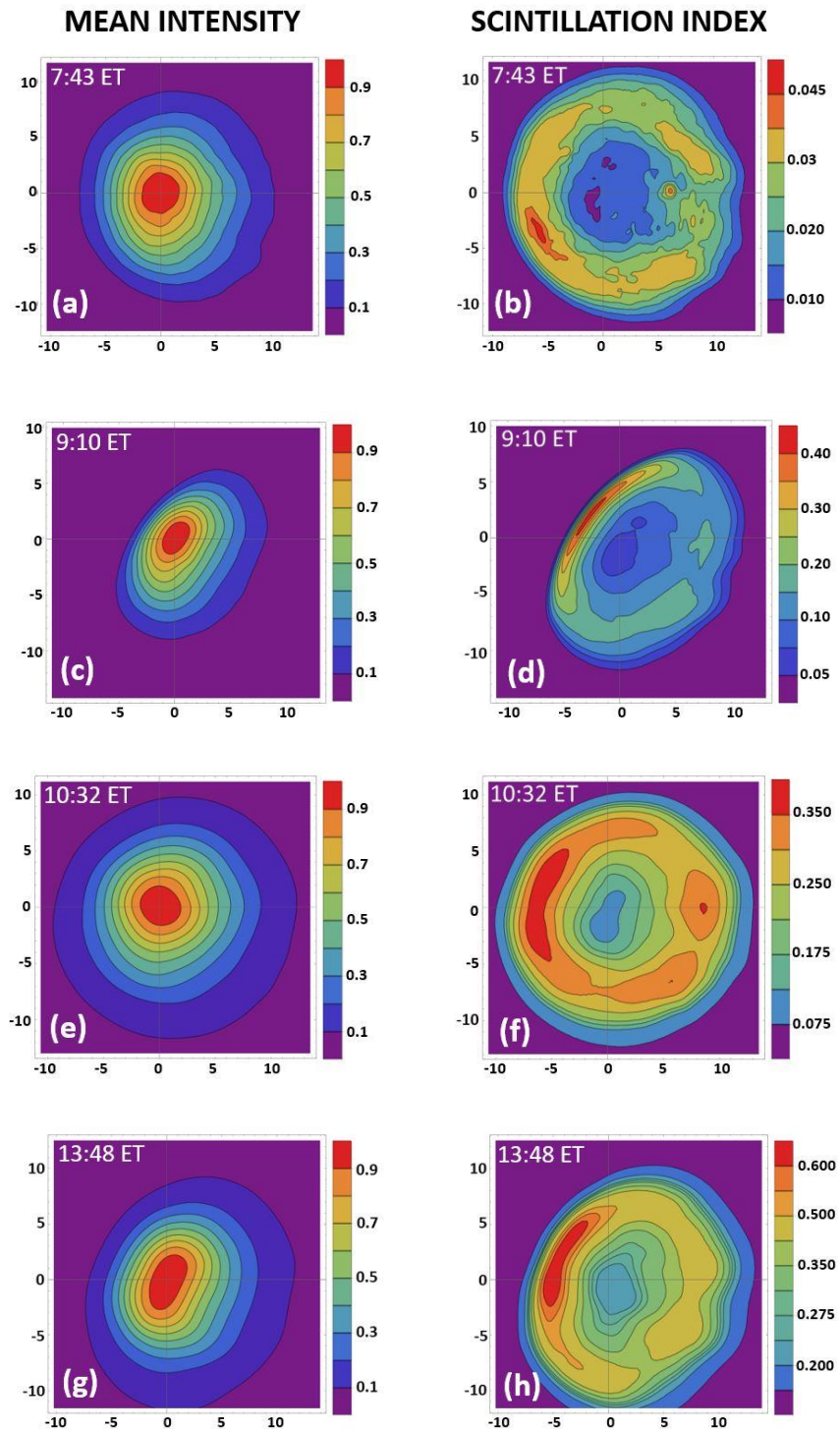


Figure 40. Measured mean intensity and corresponding scintillation index contours resulting from propagation of 6.5 mm radius beam for 125 m at SLF on 3 May 2018. (a-b) 7:43 ET; (c-d) 9:10 ET; (e-f) 10:32 ET; (g-h) 13:48 ET.

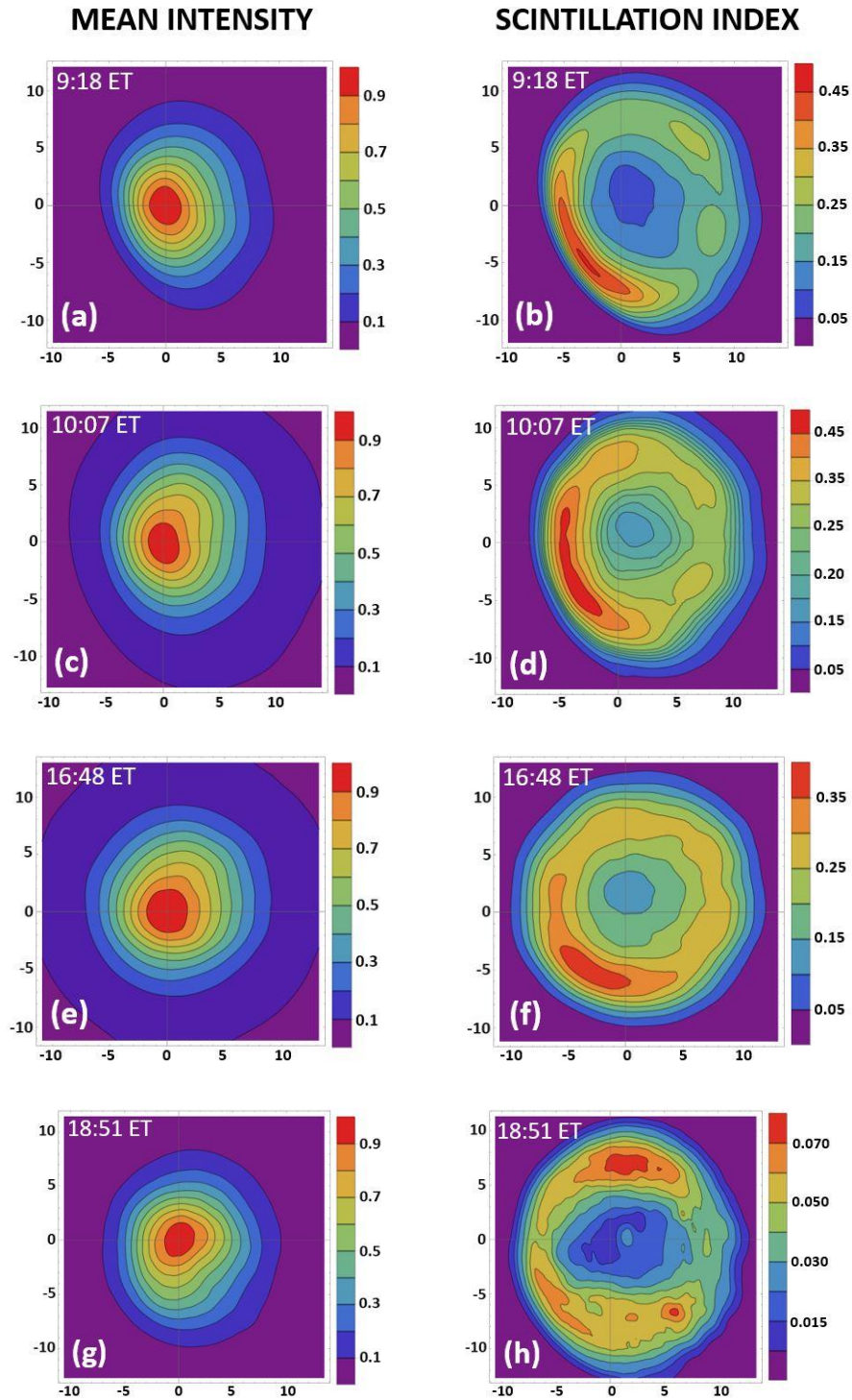


Figure 41. Measured mean intensity and corresponding scintillation index contours resulting from propagation of 6.5 mm radius beam for 125 m at TISTEF on 3 July 2018. Dimensions in mm. (a-b) 9:18 ET; (c-d) 10:07 ET; (e-f) 16:48 ET; (g-h) 18:51 ET.

7.3 Experimental Observations

In examining the data, some interesting trends can be observed. For instance, the scintillation index curves have a “statistical hot spot” on one side of the beam where it peaks (red in the plots). The mean intensity contours are compressed in this same area and the beam center is shifted from the original center toward this hot spot. Also, the center of the mean intensity contours and scintillation index contours are often misaligned due to the shift of the beam center.

Studying the atmospheric effects on a propagated Gaussian beam offers benefits not seen by some other methods of gauging atmospheric effects. It could be assumed that if the beam statistics had elliptical contours, then the turbulence was anisotropic. However, our simple math model demonstrates how things such as an index (or temperature) gradient could also cause beam statistics to appear elliptical when anisotropy may not be present. Study of the effect on a Gaussian beam gives us contrasting statistics to validate or contradict the assumption of anisotropic turbulence.

Table 2. Wind and turbulence strength information for measurement times. C_n^2 is measured using BLS900 at TISTEF and UCF manufactured device at SLF.

Location and Date	Local Time	C_n^2 (m ^{-2/3})	Transverse Wind		Horizontal Wind		Category
			Speed (m/s)	Angle (deg)	Speed (m/s)	Angle (deg)	
SLF 1 May	10:52	2.6×10^{-13}	3.7	178	4.5	60	Gradient
	14:32	6.5×10^{-13}	3.7	159	5.0	48	Isotropic
SLF 3 May	07:43	2.6×10^{-15}	1.8	-150	2.5	44	Isotropic
	09:10	3.8×10^{-14}	2.0	-127	2.7	5	Gradient
	10:32	2.3×10^{-13}	4.2	172	4.5	71	Anisotropic
	13:48	4.0×10^{-13}	4.7	141	5.0	74	Mixed
TISTEF 3 July	09:18	3.3×10^{-14}	0.6	180	0.6	76	Gradient
	10:07	7.5×10^{-14}	1.0	180	1.1	119	Mixed
	16:48	6.9×10^{-14}	1.4	3	2.8	151	Isotropic
	19:51	1.5×10^{-15}	0.7	-176	2.1	161	Anisotropic

CHAPTER 8: CONCLUSIONS

8.1 Summary of Contributions

In the work associated with this dissertation, methods were considered to detect the presence of anisotropic optical turbulence by the impact that it had on a beam and a mathematical model was developed for generalized turbulence which is valid in weak-irradiance fluctuation for the scintillation index of a Gaussian beam. Theory for the covariance function of intensity for a plane wave was extended to incorporate nonclassical turbulence. The derived theoretical behavior of a beam propagated through anisotropic turbulence was verified by multiple field experiments.

Mathematical analysis assumed that all size turbulent eddies exist and have equal anisotropy. Based on this assumption the author developed a mathematical model for the scintillation index of a Gaussian beam propagated through anisotropic turbulence neglecting inner and outer scale. The model showed that the mean intensity may or may not appear elliptical in the presence of anisotropy but the scintillation index is always predicted to have equal contours that are elliptical with anisotropy. Furthermore, we found that the ratio of major/minor axes of the scintillation index is nearly the same as the anisotropy ratio of the turbulence. The predicted behaviors were verified by experiments at the Shuttle Landing Facility and Townes Institute Science and Technology Experimentation Facility. Data from an August 2017 experiment showed

evidence of the beam having propagated through times of isotropic and anisotropic turbulence.

It was demonstrated theoretically that the covariance function of intensity of a plane wave would also have contours that are elliptical where the anisotropy ratio is similar to the major/minor axes ratio of the center of the covariance. In this analysis, a form of the turbulence spectral model was used which incorporated inner and outer scale. Furthermore, it was shown that previously collected data for a near-plane wave exhibited the predicted covariance contours. The turbulence appeared to vary from isotropic to anisotropic with an anisotropy ratio of 1.7.

Based on these previous experiments, an experiment was designed in which a 13 mm collimated Gaussian beam was propagated for 100 m or 125 m. This experiment was carried out for two days in May at the SLF and for one day in July at TISTEF. By comparing the effect of turbulence on the beam mean intensity and scintillation index to theoretical predictions, it is anticipated that we should be able to detect both anisotropy and deviations in the power law. The data that was collected using this high-quality system seemed to indicate the presence of turbulence which varied from isotropic to anisotropic but, unexpectedly, we found that at times the beam was also elliptical in ways that could not be explained by anisotropy. A simplistic model was developed that included beam ellipticity and successfully reproduced the behaviors seen in the data.

8.2 Future Work

The mathematical models and analysis completed for this dissertation represent only a start to the work necessary to successfully model beam effects from propagation through nonclassical turbulence. For instance, the anisotropy ratio probably changes with scale sizes physically while current models assume anisotropy ratio is equal for all scale sizes. Also, the mathematical models developed herein are valid only for short propagation paths. It will be valuable to extend this work into the strong irradiance fluctuation regime to study the effect of anisotropic turbulence on beams propagated long distances.

First and foremost to this researcher, the May and July 2018 experiments produced massive amounts of data which have only begun to be analyzed. For instance, even with the existing spectrum models, we could compare the mean intensity and scintillation index data to predictions based on spectral power law to estimate deviations from classical turbulence near the ground. And as changes are made to the anisotropic spectral model, this bed of data could be used for model validation. Also, this data indicated that there may be another physical effect which causes beam shaping with propagation. This effect needs further study and should be incorporated into propagation models.

APPENDIX A: DERIVATION OF THE INNER SCALE PARAMETER

To determine the value of the inner scale parameter, q_m , we can use a simpler form of the isotropic spectrum which does not include the outer scale cutoff. Also, throughout this derivation we will use the isotropic scaled spatial frequency coordinate q whereas such a derivation as given below would normally use the spatial frequency coordinate κ . The spectral model used in this derivation is

$$\Phi_n(q) = A(\alpha) \tilde{C}_n^2 \mu_x \mu_y \frac{\exp\left(-\frac{q^2}{q_m^2}\right)}{q^\alpha} \quad (\text{A.1})$$

For isotropic turbulence, the structure function simplifies from to

$$D_n(R) = 8\pi \int_0^\infty q^2 \Phi_n(q) \left(1 - \frac{\sin(qR)}{qR}\right) dq \quad (\text{A.2})$$

To evaluate this integral we substitute the series representation

$$1 - \frac{\sin(qR)}{qR} = \sum_{n=1}^{\infty} \frac{(-1)^{n-1}}{(2n+1)!} q^{2n} R^{2n} \quad (\text{A.3})$$

and integrate term wise which yields

$$D_n(R) = 4\pi A(\alpha) \tilde{C}_n^2 \mu_x \mu_y q_m^{3-\alpha} \sum_{n=1}^{\infty} \frac{(-1)^{n-1}}{(2n+1)!} (q_m R)^{2n} \Gamma\left(n + \frac{3-\alpha}{2}\right) \quad (\text{A.4})$$

where $\Gamma(\bullet)$ is the gamma function. This can be rewritten as

$$D_n(R) = 4\pi A(\alpha) \tilde{C}_n^2 \mu_x \mu_y q_m^{3-\alpha} \Gamma\left(\frac{3-\alpha}{2}\right) \left[1 - \sum_{n=0}^{\infty} \frac{\left(-\frac{q_m^2 R^2}{4}\right)^n}{n!} \frac{\left(\frac{3-\alpha}{2}\right)_n}{\left(\frac{3}{2}\right)_n} \right] \quad (\text{A.5})$$

In the above expression $(\bullet)_n$ is the Pochhammer symbol defined by

$$(a)_n = \frac{\Gamma(a+n)}{\Gamma(a)} \quad (\text{A.6})$$

Equation (A.5) can be written in terms of the confluent hypergeometric function of the first kind defined by

$${}_1F_1(a; c; z) = \sum_{n=0}^{\infty} \frac{(a)_n}{(c)_n} \frac{z^n}{n!} \quad (\text{A.7})$$

This gives a value for the structure function of

$$D_n(R) = 4\pi A(\alpha) \tilde{C}_n^2 \mu_x \mu_y q_m^{3-\alpha} \Gamma\left(\frac{3-\alpha}{2}\right) \left[{}_1F_1\left(\frac{3-\alpha}{2}; \frac{3}{2}; -\frac{q_m^2 R^2}{4}\right) \right] \quad (\text{A.8})$$

For $R \ll l_0$, we can use the small term asymptotic expression [3]

$${}_1F_1(a; c; -x) \sim 1 - \frac{a}{c} x \quad (\text{A.9})$$

With simplification, utilization of gamma function properties and substitution of the value of $A(\alpha)$, this yields

$$D_n(R) \sim \frac{\Gamma(\alpha-1) \cos(\alpha\pi/2)}{6\pi} \Gamma\left(\frac{5-\alpha}{2}\right) q_m^{5-\alpha} R^2 \tilde{C}_n^2 \mu_x \mu_y \quad (\text{A.10})$$

Using dimensional analysis, we know that in the dissipation range the structure function should be of the form [3]

$$D_n(R) = \mu_x \mu_y \tilde{C}_n^2 R^2 l_0^\beta \quad (\text{A.11})$$

Since $D_n(R)$, μ_x and μ_y are unitless, we can easily determine the value of β .

Recalling that \tilde{C}_n^2 has units of $3-\alpha$, this requires that $\beta = \alpha - 5$.

We can now determine the value for q_m by equating (A.10) and (A.11). By so doing we find

$$q_m = \frac{\left(\frac{\Gamma(\alpha-1) \cos\left(\frac{\alpha\pi}{2}\right) \Gamma\left(\frac{5-\alpha}{2}\right)}{6\pi} \right)^{\frac{1}{\alpha-5}}}{l_o} \quad (\text{A.12})$$

APPENDIX B: COPYRIGHT PERMISSIONS

Relevant to SPIE Conference Proceedings Publications:

“Study on the effect of anisotropy on a propagating beam”

“Near ground measurements of beam shaping and anisotropic turbulence over concrete runway and grass range”

TRANSFER OF COPYRIGHT TO SOCIETY OF PHOTO-OPTICAL INSTRUMENTATION ENGINEERS (SPIE)

Title _____ of _____ Paper: _____

SPIE Paper Number: (xxxx-xx) _____ Contact Author Email: _____

Author(s): _____

This signed statement must be returned to SPIE prior to the scheduled publication of the Proceedings or Journal in which the Paper will be published. The intent of this Agreement is to protect the interests of both SPIE and authors/employers and to specify reasonable rights for both parties related to publication and reuse of the material.

The undersigned hereby assign(s) to Society of Photo-Optical Instrumentation Engineers (SPIE) copyright ownership in the above Paper, effective if and when the Paper is accepted for publication by SPIE and to the extent transferable under applicable national law. This assignment gives SPIE the right to register copyright to the Paper in its name as claimant and to publish the Paper in any print or electronic medium.

Authors, or their employers in the case of works made for hire, retain the following rights:

1. All proprietary rights other than copyright, including patent rights.
2. The right to make and distribute copies of the Paper for internal purposes.
3. The right to use the material for lecture or classroom purposes.
4. The right to prepare derivative publications based on the Paper, including books or book chapters, journal papers, and magazine articles, provided that publication of a derivative work occurs subsequent to the official date of publication by SPIE.
5. The right to post an author-prepared version or an official version (preferred version) of the published paper on an internal or external server controlled exclusively by the author/employer, provided that (a) such posting is noncommercial in nature and the paper is made available to users without charge; (b) a copyright notice and full citation appear with the paper, and (c) a link to SPIE's official online version of the abstract is provided using the DOI (Document Object Identifier) link.

Citation format:

Author(s), "Paper Title," Publication Title, Editors, Volume (Issue) Number, Article (or Page) Number, (Year).

Copyright notice format:

Copyright XXXX (year) Society of Photo-Optical Instrumentation Engineers. One print or electronic copy may be made for personal use only. Systematic reproduction and distribution, duplication of any material in this paper for a fee or for commercial purposes, or modification of the content of the paper are prohibited.

DOI abstract link format:

<http://dx.doi.org/DOI#> (Note: The DOI can be found on the title page or online abstract page of any SPIE article.)

If the work that forms the basis of this Paper was done under a contract with a governmental agency or other entity that retains certain rights, this Transfer of Copyright is subject to any rights that such governmental agency or other entity may have acquired.

By signing this Agreement, the authors warrant that (1) the Paper is original and has not previously been published elsewhere; (2) this work does not infringe on any copyright or other rights in any other work; (3) all necessary reproduction permissions, licenses, and clearances have been obtained; and (4) the authors own the copyright in the Paper, are authorized to transfer it, and have full power to enter into this Agreement with SPIE.

WHO SHOULD SIGN. This form must be signed by (1) at least one author who is not a U.S. Government employee and (2) the author's employer if the Paper was prepared within the scope of the author's employment or was commissioned by the employer. If not signed by all authors, the author(s) signing this Agreement represents that he/she is signing this Agreement as authorized agent for and on behalf of all the authors.

Author's signature _____ Print name _____ Date (mm/dd/yyyy) _____

Author's signature _____ Print name _____ Date (mm/dd/yyyy) _____

33536 East Lake Joanna Drive
Eustis, Florida 32736

August 28, 2018

Dear OSA Copyright Office,

This letter will confirm our recent telephone conversation. I am completing a doctoral dissertation at the University of Central Florida entitled "Effect of Nonclassical Optical Turbulence on a Propagating Laser." I would like your permission to reprint in my dissertation excerpts from the following publications of which I am first author:

"Evidence of Anisotropic Optical Turbulence over Runway" (Conference Proceedings)

"Evolution of Near Ground Optical Turbulence over Concrete Runway throughout Multiple Days in Summer and Winter" (JOSA A 35, 2018)

"Near Ground Measure and Theoretical Model of Plane Wave Covariance of Intensity in Anisotropic Turbulence" (Optics Letters 43, 2018)

The requested permission extends to any future revisions and editions of my dissertation, including non-exclusive world rights in all languages. These rights will in no way restrict republication of the material in any other form by you or by others authorized by you. Your signing of this letter will also confirm that you own or your company owns the copyright to the above-described material.

If these arrangements meet with your approval, please sign this letter where indicated, scan, and return to me. Thank you for your attention in this matter.

Sincerely,

Melissa Beason

PERMISSION GRANTED FOR THE USE REQUESTED ABOVE:

By:  Rebecca Robinson, The Optical Society
(Sign) (Print)
Date: 6 September 2018

REFERENCES

1. R. R. Beland, "Propagation through atmospheric optical turbulence," in *The Infrared and Electro Optical Systems Handbook*, F. G. Smith, ed. (SPIE Optical Engineering Press, 1993), Vol. 2, Chap. 2.
2. Andrews, L. C., Phillips, R. L., Wayne, D., Sauer, P., Leclerc, T., and Crabbs, R., "Creating a C_n^2 profile as a function of altitude using scintillation measurements along a slant path," *Proc. SPIE* 8238, 82380(2012).
3. L. C. Andrews and R. L. Phillips, *Laser Beam Propagation through Random Media*, 2nd ed. (SPIE, 2005).
4. A. A. Consortini, L. Ronchi, and L. Stefanutti, "Investigation of atmospheric turbulence by narrow Laser Beams," *Appl. Opt.* **9**, 2543-2547 (1970).
5. A. Kon, "Qualitative theory of amplitude and phase fluctuations in a medium with anisotropic turbulent irregularities," *Waves in Random Media* **4**, 297-305 (1994).
6. F. Wang, I. Toselli, J. Li, O. Korotkova, "Measuring anisotropy ellipse of atmospheric turbulence by intensity correlations of laser light," *Optics Letters* **42**, 1129-1132 (2017).
7. A. N. Kolmogorov, "The local structure of turbulence in an incompressible viscous fluid for very large Reynolds numbers," *C. R. (Doki) Acad. Sci. U.S.S.R.* **30**, 301-305 (1941).
8. A. M. Obukhov, "Structure of the Temperature Field in a Turbulent Flow," *Investiya Akademii Nauk SSSR, Seriya Geograficheskaya i Geofizicheskaya* (Bulletin of the Academy of Sciences of the USSR, Geographical and Geophysical Series), **13**, No. 1, 58-69 (1949).
9. S. Corsin, "On the Spectrum of Isotropic Temperature Fluctuations in an Isotropic Turbulence," *Journal of Applied Physics*, **22**, No. 4, 469-473 (1951).
10. A. D. Wheelon, "Electromagnetic Scintillation: I. Geometrical Optics," (Cambridge University Press, 2001).
11. R. J. Hill and S. F. Clifford, "Modified spectrum of atmospheric temperature fluctuations and its application to optical propagation," *J. Opt. Soc. Am.* **68**, 892-899 (1978).

12. J. C. Owens, "Optical refractive index of air: Dependence on pressure, temperature, and compositions," *Appl. Opt.* **6**, 51-59 (1967).
13. V. I. Tatarskii, *Wave Propagation in a Turbulent Medium* (McGraw-Hill, New York, 1961), translation by R. A. Silverman.
14. V. I. Tatarskii, *The Effects of the Turbulent Atmosphere on Wave Propagation* (translated for NOAA by Israel Program for Scientific Translations, Jerusalem, 1971).
15. M. Beason, L. Andrews, R. Phillips, "Study on the effect of anisotropy on a propagating beam," *Proc. SPIE* 10408, 104080B-1 (2017).
16. L. C. Andrews, R. L. Phillips, and R. Crabbs, "Propagation of a Gaussian beam wave in general anisotropic turbulence," *Proc. SPIE* 9224, 922402 (2104).
17. M. Beason, C. Smith, J. Coffaro, S. Belichki, J. Spsychalsky, F. Titus, R. Crabbs, L. Andrews, R. Phillips, "Near ground measure and theoretical model of plane wave covariance of intensity in anisotropic turbulence," *Optics Letters* **43**, 2607-2610 (2018).
18. J. E. McCrae, C. E. Murphy, S. R. Bose-Pillai, C. A. Rice and S. T. Fiorino, "The influence of wind on anisotropy in optical turbulence," in *Proceedings of IEEE Conference on Aerospace* (IEEE, 2018), pp. 1-8.
19. M. Beason, J. Coffaro, C. Smith, J. Spsychalsky, S. Belichki, F. Titus, F. Sanzone, B. Berry, R. Crabbs, L. Andrews, and R. Phillips, "Evolution of near ground optical turbulence over concrete runway throughout multiple days in summer and winter," *J. Opt. Soc. Am. A* **35**, 1393-1400 (2018).
20. M. Beason, F. Sanzone, J. Coffaro, C. Smith, J. Spsychalsky, B. Berry, F. Titus, R. Crabbs, L. Andrews, R. Phillips, "Near ground measurements of beam shaping and anisotropic turbulence over concrete runway and grass range," *Proc. SPIE* 10408, 104080B (2018).
21. V. Kulikov, M. Vorontsov, "Analysis of the joint impact of atmospheric turbulence and refractivity on laser beam propagation," *Opt Express* **25**, 28524-28535 (2017).
22. M. Vorontsov, V. Kulikov, "Accounting for optical refractivity and turbulence effects in optical wave propagation over long distances," *Proc. SPIE* 10650, 1065009 (2018).
23. R. Maimon, "Refractive index of air in dependence of temperature," <https://physics.stackexchange.com/q/14948>, (26 September 2017).